

Implementation of the Remove–Compute–Restore Method for Regional Geoid Determination Using GRAV-D Airborne Gravity Data in the United States

A Thesis Submitted

In Partial Fulfilment of the Requirements

for the Degree of

Master of Science by Research

By

Sreekanth K S

(231030409)



to the

DEPARTMENT OF CIVIL ENGINEERING

INDIAN INSTITUTE OF TECHNOLOGY KANPUR

June 2025

Certificate

It is certified that the work contained in the thesis titled "**Implementation of the Remove–Compute–Restore Method for Regional Geoid Determination Using GRAV-D Airborne Gravity Data in the United States**" by **Sreekanth K S** (231030409), has been carried out under my supervision and this work has not been submitted elsewhere for a degree.



Maj. Gen. Dr. B. Nagarajan

Professor

Department of Civil Engineering

Indian Institute of Technology Kanpur

June, 2025

Declaration

This is to certify that the thesis titled "**Implementation of the Remove–Compute–Restore Method for Regional Geoid Determination Using GRAV-D Airborne Gravity Data in the United States**" has been authored by me. It presents the research conducted by me under the supervision of **Maj. Gen. Dr. B. Nagarajan**.

To the best of my knowledge, it is an original work, both in terms of research content and narrative, and has not been submitted elsewhere, in part or in full, for a degree. Further, due credit has been attributed to the relevant state-of-the-art and collaborations (if any) with appropriate citations and acknowledgements, in line with established norms and practices.



Sreekanth K S

231030409

MSR, Geoinformatics

Department of Civil Engineering

Indian Institute of Technology Kanpur

Abstract

Name of the student: **Sreekanth K S**

Roll No: **231030409**

Degree for which submitted: **MSR**

Department: **CE**

Thesis title: **Implementation of the Remove–Compute–Restore Method for Regional Geoid Determination Using GRAV-D Airborne Gravity Data in the United States**

Thesis supervisors: **Maj. Gen. Dr. B. Nagarajan**

Month and year of thesis submission: **June 2025**

This study presents a high-resolution regional geoid model over southwestern Colorado (37° – 38° N, 107° – 108° W), incorporating airborne gravity data from the Gravity for the Redefinition of the American Vertical Datum (GRAV-D) project, topographic corrections, and indirect topographic effects. A remove–compute–restore framework was implemented, wherein medium and short-wavelength gravity anomalies were derived from GRAV-D airborne data after applying second-order free-air, atmospheric, and terrain corrections. Stokes' integration was performed using Fast Fourier Transform (FFT)-based convolution to compute the residual geoid, which was then refined by adding the indirect topographic effect derived from a planar FFT-based convolution over a high-resolution Digital Elevation Model (DEM). The final regional geoid model was validated against 58 high-accuracy geometric geoid heights from the Geoid Slope Validation Survey (GSVS) dataset.

Results show that the final geoid model achieves a root mean square error (RMSE) of 0.470 m, a mean error (bias) of -0.461 m, and a standard deviation (SD) of 0.094 m, demonstrating both high accuracy and strong internal consistency. In contrast, global models such as the Earth Gravitational Model (EGM; RMSE: 1.045 m, SD: 0.022 m) and the Global Gravity Model GGM05G (RMSE: 1.643 m, SD: 0.125 m) exhibit higher total error and less local fidelity. Notably, while the initial tiled approach for computing the indirect topographic effect introduced artifacts in steep terrain, a revised global FFT formulation with 3σ outlier filtering yielded a physically smooth and consistent geoid.

The analysis underscores the limitations of planar indirect-effect computation in mountainous regions and highlights the need for spherical or residual terrain modelling (RTM) techniques in future studies. Overall, this work demonstrates that combining airborne gravity data with refined terrain modelling enables the development of regional geoid models with sub-meter total accuracy, minimal bias, and centimetre-level precision—especially critical for vertical datum realization in rugged topography.

Acknowledgements

I would like to express my sincere gratitude to my thesis supervisor, Maj. Gen. Dr. B. Nagarajan, for his invaluable guidance, continuous encouragement, and insightful feedback throughout the course of this research. His mentorship has been instrumental in shaping my academic and professional growth.

I extend my heartfelt thanks to the National Centre for Geodesy (NCG) for providing excellent research facilities, a collaborative environment, and the resources essential for the successful completion of my thesis.

My sincere appreciation goes to Dr. Somalin Nath, Research Associate at NCG, for her consistent support, technical insights, and constructive discussions that enriched the quality of this work.

I am also grateful to Dr. Balaji Devaraju for his engaging and thorough instruction in physical geodesy, which laid a strong foundation for my understanding of the subject and significantly influenced the direction of this research.

I would like to thank my friends for their companionship, encouragement, and constant support throughout this journey. Lastly, I owe a deep debt of gratitude to my family for their unwavering love, patience, and moral support that kept me grounded and motivated every step of the way.

Contents

Acknowledgements.....	vi
List of Figures.....	x
List of Tables.....	xii
List of Abbreviations	xiii
Chapter 1. Introduction.....	1
1.1 Background and Motivation	1
1.2 Objective of the Study	3
1.3 Scope and Limitations	3
1.4 Structure of the Thesis	5
Chapter 2. Theoretical Background.....	7
2.1 Gravitation	7
2.2 Gravitational Potential of Extended Bodies.....	7
2.3 Gravity Field and Boundary Value Problems	8
2.4 The Normal and Disturbing Fields	8
2.5 Gravity and Normal Gravity	9
2.6 Geoid, Ellipsoid, and Height Systems	9
2.7 Gravity Disturbance and Gravity Anomaly	11
2.8 Gravity Reduction.....	12
2.8.1 Free-Air Reduction	13
2.8.2 Bouguer Reduction	14
2.8.3 Terrain Correction.....	14
2.8.4 Indirect Effects of Gravity Reductions	15
2.9 Geoid Height and Bruns' Formula	16
2.10 Fundamental Equation of Physical Geodesy	17
2.11 Stokes Formula	18
Chapter 3. Literature Review	19

3.1 Limitations of Global Geoid Models in High-Relief Terrain	19
3.2 Airborne Gravimetry for Regional Geoid Modelling	20
3.3 Classical Remove–Compute–Restore (RCR) Geoid Modeling.....	20
3.4 Downward Continuation of Airborne Data.....	21
3.5 FFT-Based Stokes and Terrain Corrections	22
3.6 Global Geopotential Models and Data Integration	22
3.7 Indirect Topographic Effects.....	23
3.8 Validation with GNSS/Levelling Data.....	23
3.9 Case Studies and Comparative Approaches.....	24
3.10 Recent Advances and Future Directions	25
Chapter 4. Study Area and Data Sources	26
4.1 Study Area.....	26
4.2 Airborne Gravity (GRAV-D).....	27
4.3 Global Geopotential Model (GGM05G).....	32
4.4 Digital Elevation Model (SRTM 1 Arc-second DEM)	33
4.5 Validation Data (Geoid Slope Validation Survey)	35
Chapter 5. Methodology	37
5.1 Input Data Requirements	38
5.2 Gravity Reductions and Anomaly Computation	38
5.3 Removal of Long-Wavelength Geopotential Signal	39
5.4 Atmospheric Correction.....	40
5.5 Terrain Corrections via FFT.....	41
5.6 Computation of the Faye Anomaly	42
5.7 Stokes Integral via FFT.....	42
5.8 Brun’s Formula and Conversion to Geoid Undulation	44
5.9 Restoration of the Global Geoid	44
5.10 Indirect Topographic Effect	45
5.11 Final Geoid Computation.....	46

Chapter 6. Results and Discussions	48
6.1 Observed gravity data visualisation and analysis	48
6.2 GGM-Derived Geoid Heights and Gravity Anomalies.....	54
6.3 Normal Gravity	56
6.4 Second-Order Free-Air Correction	56
6.5 Free-Air Anomaly	57
6.6 Short and Medium Wavelength Gravity Anomaly.....	58
6.7 Atmospheric Correction.....	58
6.8 Gravity Anomaly Corrected for Atmosphere.....	59
6.9 Analysis of Gravity Anomaly and Topography in the Modelling Region	60
6.10 Correlation Between Elevation and Gravity Anomaly	62
6.11 Terrain Correction via FFT: Edge Artifacts and Mitigation.....	64
6.12 Transition from Short and Medium Wavelength Anomaly to Faye Anomaly and Suitability for Geoid Modelling.....	68
6.13 Computation and Analysis of the Disturbing Potential Using FFT-Based Stokes Integration.....	70
6.14 Construction of the Co-Geoid Model	72
6.15 Evaluation of the Co-Geoid Model and Accuracy Assessment	74
6.16 Planar FFT-Based Indirect-Effect Computation	76
6.17 Indirect Effect Recalculated Using Global FFT Approach.....	81
6.18 Quantitative Comparison of Geoid Versions in the Modelling Region	83
6.19 Validation of EGM-Based Geoid and Comparative Assessment	84
6.20 Synthesis of Validation Results.....	86
Chapter 7. Conclusions and Recommendations.....	87
7.1 Conclusions.....	87
7.2 Recommendations.....	88
7.3 Future Work	88
References.....	90

List of Figures

2.1	Geometric relationship between topography, geoid, and ellipsoid	10
2.2	Difference between gravity anomaly and gravity disturbance	11
2.3	Conceptual diagram of gravity reduction in geoid determination	12
2.4	Conceptual representation of co-geoid	16
	Study area map showing the location and context of the geoid	27
4.1	modelling region in southwestern Colorado within the broader GRAV-D Block MS05	
5.1	Schematic flowchart of the RCR geoid modelling pipeline	37
6.1	Scatter plot of the gravity observations with modelling region highlighted in grey	49
6.2	Histogram of airborne gravity data	50
6.3	Histogram of flight altitudes	52
6.4	3D Scatter plot of observed gravity	53
6.5	GGM derived geoid heights	55
6.6	GGM derived gravity anomalies	55
6.7	Normal gravity	56
6.8	Second order free air correction	57
6.9	Free air anomaly	57
6.10	Short and medium wavelength gravity anomaly	58
6.11	Atmospheric correction	59
6.12	Gravity anomaly corrected for atmosphere	59
6.13	Interpolated plot of gravity anomaly overlaid with observation points	60
6.14	Digital Elevation Model	62
6.15	Scatterplot of gravity anomaly vs elevation	63
6.16	Terrain correction (TC) map computed by naïve 2D FFT convolution (no padding)	64
6.17	FFT TC map after 3σ outlier clipping	65
6.18	Terrain correction map using tiled FFT convolution	66
6.19	Faye Anomaly	69
6.20	Disturbing potential	71

6.21	Residual geoid	72
6.22	GGM05G geoid	73
6.23	Co-geoid	74
6.24	Histogram of co-geoid and GGM05G geoid differences	75
6.25	Initial indirect-effect map computed using a tile-wise planar FFT convolution over the DEM	77
6.26	Regional geoid map obtained by adding the tile-based indirect-effect grid (from Figure 6.25) to the co-geoid.	78
6.27	Improved indirect-effect map generated using a single global planar FFT convolution over the entire DEM	82
6.28	Final regional geoid model after applying the globally computed indirect effect (from Figure 6.27) to the co-geoid.	82
6.29	EGM 2008 Geoid	85

List of Tables

6.1	Comparison of geoid height accuracy between GGM05G and the co-geoid using GSVS17 control points	76
6.2	Quantitative comparison of geoid model versions in the study region, based on RMSE, mean error, standard deviation, and surface roughness (RMS gradient).	83
6.3	Validation statistics of the interpolated EGM-derived geoid using GSVS17 control points	58 84
6.4	Consolidated validation statistics for all geoid models using 58 GS VS17 control points	86

List of Abbreviations

ATMC	Atmospheric Correction
BC	Bouguer Correction
BVP	Boundary Value Problem
DEM	Digital Elevation Model
EGM	Earth Gravitational Model
FAA	Free Air Anomaly
FAC	Free Air Correction
FFT	Fast Fourier Transform
GGM	Global Geoid Model
GGM05G	Global Gravity Model 05 GOCE and GRACE
GNSS	Global Navigation Satellite System
GPS	Global Positioning System
GRAVD	Gravity for the Redefinition of the American Vertical Datum
GSVS	Geoid Slope Validation Survey
ICGEM	International Centre for Global Earth Models
MSL	Mean Sea Level
RCR	Remove Compute Restore
RMSE	Root Mean Square Error
RTM	Residual Terrain Modelling
SRTM	Shuttle Radar Topography Mission
SST	Sea Surface Topography
TC	Terrain Correction
WGS	World Geodetic System

Chapter 1. Introduction

1.1 Background and Motivation

The question of Earth's shape has intrigued humanity for centuries. While we often describe shapes using geometric terms, the Earth's form is far more complex, influenced by both geometry and physics. Understanding the Earth's shape is crucial, particularly when defining concepts like verticality and measuring heights.

Shape is often associated with a geometric outline or boundary. According to Wikipedia, shape is "a graphical representation of an object's form or its external boundary, outline, or external surface." However, when discussing Earth's shape, we are not only referring to its geometric form but also considering its physical characteristics. This perspective is essential in geodesy, where the Earth's shape is defined by gravitational forces, resulting in surfaces of equal potential.

Height, on the other hand, is not just a geometric measurement but also a physical quantity that relates to potential energy within Earth's gravity field. To measure height consistently, we need a common reference surface. Typically, this surface is geoid, but the concept of geoid is more complex than it seems. It is a representation of an equipotential surface—a surface where gravitational potential is constant.

To understand height measurement, consider how water behaves. In a hypothetical, force-free Earth, bodies of water would naturally settle into equipotential surfaces, forming reference surfaces for height measurements. Gravity acts perpendicular to these surfaces at every point, making them ideal for defining a baseline for measuring elevations.

Geoid can be approximated by the Mean Sea Level (MSL). But there is variation between mean sea level and geoid which is called Sea Surface Topography (SST), which may in the order of ± 2 meters. We know 71% of the Earth's surface is covered by oceans, MSL is thus conventionally used as an approximated reference surface. However, on continents, lakes and other bodies of water also represent local equipotential surfaces. Therefore, there are many such surfaces, but the geoid is the most widely recognized as the "zero-height" reference surface globally.

The geoid is a physical, rather than purely geometric, representation of Earth's shape, reflecting variations in Earth's mass distribution. Determining the geoid is vital for obtaining globally consistent height measurements.

To determine the geoid, we first approximate Earth's shape using a reference ellipsoid—a mathematically defined surface. We then measure deviations between the ellipsoid and the actual geoid, capturing the Earth's irregularities. This process involves analysing gravity data to infer mass distribution and potential variations.

It is important to distinguish between gravitation and gravity. Gravitation refers to the fundamental force of attraction between masses, as described by Newton's law of universal gravitation. Gravity, on the other hand, is the observable force experienced at or near Earth's surface, which includes both the gravitational attraction due to Earth's mass and the centrifugal acceleration arising from Earth's rotation. As a result, terrestrial gravity measurements reflect the combined effect of mass distribution and rotational forces. In airborne gravity surveys, the measurements are further affected by additional fictitious forces, particularly the Coriolis force, which arises due to the motion of the aircraft relative to Earth's rotating reference frame. This Coriolis effect must be corrected during data processing to isolate the true gravity signal.

Beyond scientific curiosity, accurately modelling the Earth's shape has practical importance. The geoid undulation enables conversion of Global Positioning System (GPS)-derived ellipsoidal heights to orthometric heights, which are critical for civil engineering, flood risk assessment, infrastructure development, and land surveying.

Despite its importance, existing tools for regional geoid modelling often present barriers to entry for beginners. Many available software solutions are proprietary, complex, or lack comprehensive documentation, making them less accessible to students and early-career professionals. Moreover, while advanced methods have gained prominence, foundational techniques like the classical Remove-Restore method remain underrepresented in user-friendly, open-source formats.

Addressing this gap, this research aims to develop an open-source Python toolbox that implements the classical Remove-Restore method for regional geoid modelling, utilizing airborne gravity data. This toolbox is designed as an educational resource, simplifying the geoid modelling process and providing a stepping stone for learners to grasp fundamental concepts before progressing to more advanced methodologies.

By democratizing access to geoid modelling tools and emphasizing foundational techniques, this project seeks to empower a broader audience to engage with geodetic science, fostering a deeper understanding of Earth's physical characteristics and enhancing the precision of geospatial analyses.

1.2 Objective of the Study

The primary objective of this study is to implement the classical Remove-Restore (RCR) method for regional geoid determination using airborne gravity data from the GRAV-D (Gravity for the Redefinition of the Vertical Datum) project. This approach aims to provide a systematic framework for geoid modelling by refining gravity data and integrating multiple datasets to enhance geoid accuracy and spatial resolution.

To achieve this, the study is guided by the following specific objectives:

- Translate the RCR methodology from theoretical formulation to practical application, using airborne gravity data and global geopotential models to isolate residual gravity signals relevant for local geoid modelling.
- Apply precise terrain corrections using high-resolution digital elevation models to account for topographic mass effects, including both direct and indirect topographic contributions.
- Demonstrate the effectiveness of airborne gravity data in improving satellite-derived global geoid models, thereby increasing resolution and reducing regional geoid errors in complex terrain.
- Validate the gravimetric geoid model by comparing it with geometric geoid heights derived from GNSS/levelling benchmarks, specifically using the Geoid Slope Validation Survey 2017 (GSVS17) dataset, to quantify modelling accuracy and evaluate the consistency of the results.

1.3 Scope and Limitations

Scope:

- The study focuses on developing a regional geoid model over a selected area in the United States using airborne gravity data from the GRAV-D project, with a specific emphasis on a $1^\circ \times 1^\circ$ grid with 1 arc-second resolution where validation points from the GSVS17 dataset are available.

- Integration of GRAV-D airborne gravity data, Shuttle Radar Topography Mission (SRTM) 1 arc-second Digital Elevation Model (DEM), and the Global Gravity Model 2005 (GGM05G) — a satellite-derived global geopotential model. GGM05G provides long-wavelength gravity field information, which is essential for preserving the low-frequency component of the Earth's gravity field during regional geoid modelling. The combination of these datasets enables the capture of short- and medium-wavelength gravity signals while retaining the global structure from GGM05G.
- Implementation of the classical Remove-Compute-Restore method, incorporating terrain and atmospheric corrections, Fast Fourier Transform (FFT)-based Stokes integration, and Brun's formula for geoid undulation calculation.
- Application of FFT techniques for efficient Stokes integral evaluation to handle large datasets and maintain computational efficiency.
- The methodology is designed specifically for GRAV-D data, given its publicly accessible, uniform, and dense nature, making it suitable for interpolation techniques.
- The study is conducted in a hilly terrain, allowing for assessment of geoid modelling performance in complex topography.
- All data processing and modelling are performed with World Geodetic System 1984 (WGS 84) as the consistent reference datum.

Limitations:

- Although absolute gravity measurements from ground stations are used as tie points for calibration and quality control, only airborne gravity data are used for geoid modelling in this study.
- Although the airborne dataset covers a larger area, the modelling is confined to a $1^\circ \times 1^\circ$ grid to align with the available validation benchmarks.
- While the methodology adopted here is universally applicable, the current implementation is tailored specifically to datasets from the GRAV-D project, which are available for the United States. As such, this study is limited to a U.S.-based region for demonstration and validation, but the approach can be adapted to other regions with suitable gravity and topographic data.

- For the removal of long-wavelength components, gravity anomaly values are obtained from the International Centre for Global Earth Models (ICGEM) geoid computation service, which provides online access to a variety of global gravity field models. Users are required to manually upload geodetic coordinates to the ICGEM portal to retrieve corresponding gravity anomaly or geoid undulation values based on selected global models (e.g., GGM05G). This manual interaction is necessary due to the service's web-based interface.
- The FFT-based approach uses planar approximations for integral evaluation instead of actual numerical integrals, potentially introducing minor errors in regions with steep topography.
- Linear interpolation is employed based on the assumption of uniform spatial density in the GRAV-D dataset, which may not be applicable in regions with sparse data.
- The SRTM 1 arc-second DEM is used for terrain correction and indirect topographic effect computations due to its high spatial resolution and global availability. However, the vertical accuracy of the DEM is not independently assessed in this study, and potential elevation errors or artifacts in the SRTM data are not accounted for in the geoid modelling process.
- The applicability of the methodology in terrains other than hilly regions has not been evaluated in this study.

1.4 Structure of the Thesis

The thesis is structured into six main chapters, each focusing on a distinct aspect of the study.

Chapter 1, Introduction, provides the background and motivation for the study, emphasizing the significance of accurate regional geoid models and the potential of airborne gravity data to enhance geoid accuracy. It outlines the research objectives and clearly defines the scope and limitations of the work. The chapter concludes with a brief overview of the thesis structure to guide the reader through the subsequent sections.

Chapter 2, Theoretical background, provides a comprehensive theoretical foundation for geoid modelling in physical geodesy. It begins with Newtonian gravitation and extends to the gravitational potential of extended bodies. It introduces key concepts such as geopotential, normal potential, and disturbing potential, which are essential for

understanding the Earth's gravity field. The chapter also discusses geoid, ellipsoid, and height systems, and explains gravity anomalies and reduction techniques like Free-Air, Bouguer, and Terrain corrections. It concludes with Bruns' formula and the fundamental equation linking gravity anomalies to the disturbing potential for geoid height determination.

Chapter 3, Literature Review, presents a comprehensive review of existing work relevant to geoid modelling. It discusses classical geoid determination techniques and the evolution of the Remove-Compute-Restore (RCR) method, with a specific focus on the application of airborne gravity data, particularly from the GRAV-D project. Additionally, the chapter examines FFT-based Stokes integration methods, terrain correction strategies, and validation techniques using GNSS/levelling data such as the GSVS17 dataset.

Chapter 4, Study Area and Data Sources, provides a detailed description of the study area, specifying the selected MS05 block from the GRAV-D dataset. It offers an overview of the datasets used, including airborne gravity data, SRTM 1 arc-second DEM, the GGM05G global gravity model, and the GSVS17 GNSS/levelling dataset.

Chapter 5, Methodology, details the step-by-step approach employed in the study, beginning with an overview of the Remove-Compute-Restore technique. It describes the data preparation processes, including gridding and interpolation, followed by FFT-based Stokes kernel convolution for geoid computation. Terrain correction methods using the DEM and the computation of geoid undulations from residual gravity anomalies are explained.

Chapter 6, Results and Discussion, interprets the results, including intermediate and final outputs like free-air anomalies, terrain corrections, and geoid undulations. Includes visualizations such as maps, profiles, and histograms that aid understanding. Validation is performed using RMSE and bias statistics from GSVS17 data. Error patterns and residuals are analysed, with suggestions offered for methodological improvements.

Chapter 7, Conclusions and Recommendations, synthesizes the key findings and conclusions drawn from the study, emphasizing contributions to regional geoid modelling using GRAV-D data and FFT-based integration methods.

Chapter 2. Theoretical Background

2.1 Gravitation

According to Newton's law of universal gravitation, the force of attraction 'F' between two-point masses ' m_1 ' and ' m_2 ' is directly proportional to the product of their masses and inversely proportional to the square of the distance 'r' separating them. This relationship is mathematically expressed as:

$$F = \frac{Gm_1m_2}{r^2} \quad (2.1)$$

where G is the gravitational constant, approximately equal to $6.6743 \times 10^{-11} \text{ m}^3 \text{ kg}^{-1} \text{ s}^{-2}$. In geodesy, we are particularly interested in the gravitational field generated by a single point mass.

The equations presented in this chapter (Equations 2.1 to 2.20) are primarily drawn from or adapted based on the classical formulations provided in Heiskanen and Moritz (1967), unless explicitly referenced otherwise.

Let us denote the source mass by 'm', and consider the gravitational acceleration 'a' it produces at a point located a distance 'r' away as:

$$a = \frac{F}{m_2} = \frac{Gm}{r^2} \quad (2.2)$$

This acceleration vector \vec{a} can also be interpreted as the gradient of a scalar potential field known as the gravitational potential V, given by:

$$V = \frac{Gm}{r} \quad (2.3)$$

However, these expressions are valid only for idealized point masses. The real Earth, with its complex and inhomogeneous mass distribution, requires a more general formulation.

2.2 Gravitational Potential of Extended Bodies

For an extended mass body, the gravitational potential V_P at a point P is determined by integrating over the volume of the body:

$$V_P = G \iiint \frac{\rho(x, y, z)}{r} dx dy dz \quad (2.4)$$

where $\rho(x, y, z)$ is the local mass density and ‘r’ is the distance from the mass element to point P. Unfortunately, for the Earth, this integral cannot be evaluated exactly since the internal density distribution is not known with sufficient precision.

While Newton’s law allows computation of a gravitational field if the shape and density of a body are known, the Earth poses unique challenges: neither its precise density distribution nor the exact shape, the geoid—the equipotential surface is fully known.

2.3 Gravity Field and Boundary Value Problems

However, we may ask: Can we determine the gravitational field in the space surrounding the Earth without knowing its internal density structure, but by using gravitational potential values on a known boundary surface? This question arises in satellite orbit determination, where we seek to compute the gravitational acceleration acting on the satellite. The resulting mathematical formulation is a boundary value problem (BVP).

In such problems, the goal is to determine a function (here, the gravitational potential) inside a spatial domain based on, values of the function on the boundary, and its governing partial differential equation. In geodesy, however, even the boundary surface (the geoid) is unknown and must be estimated. This adds a layer of complexity to the BVP.

In this thesis, the focus is not on determining the external gravitational field but on determining the geoid itself.

Moreover, we cannot directly measure gravitational potential. What we can measure is gravitational attraction—more accurately, gravity, which includes not only gravitational attraction but also the effects of Earth’s rotation, which is the centrifugal acceleration.

2.4 The Normal and Disturbing Fields

In physical geodesy, the Earth’s gravity field is characterized by the geopotential ‘W’. To facilitate practical computations and analyses, especially given the complexity of Earth’s actual mass distribution, a simplified model known as the normal potential ‘U’ is employed. This model represents an idealized Earth, typically an ellipsoid with uniform rotation and mass distribution.

The disturbing potential ‘T’ is defined as the difference between the actual geopotential and the normal potential. This potential encapsulates the deviations of the Earth’s actual gravity field from the idealized model. Notably, T is harmonic (i.e., it satisfies Laplace’s equation) in regions outside the Earth’s mass distribution, assuming the atmosphere’s mass is negligible. This harmonic property makes T particularly useful for mathematical modelling and geodetic computations.

The actual gravity potential W of the Earth is then related to the normal potential U through the disturbing potential T as:

$$W = U + T \quad (2.5)$$

The goal of geoid determination is to compute the geoid undulation or height, which is closely related to the disturbing potential T which will be explained in section 2.9.

2.5 Gravity and Normal Gravity

The gravitational acceleration \vec{g} experienced at a point on or near the Earth’s surface is derived from the gradient of the geopotential along the plumb line:

$$\vec{g} = \nabla W \quad (2.6)$$

Similarly, the normal gravity $\vec{\gamma}$ is the gradient of the normal potential along the normal to the reference ellipsoid:

$$\vec{\gamma} = \nabla U \quad (2.7)$$

These vectors point in the direction of the steepest increase of their respective potentials and have magnitudes corresponding to the gravitational acceleration at that point.

In physical geodesy, observable quantities are compared to those computed from an idealized reference model. Consequently, we work with anomalous quantities, which refer to differences between observed and computed values at an approximate (reference) location. Before going to understand gravity anomaly one needs to have a geometrical visualisation of geoid, ellipsoid and related heights which is explained in section 2.6.

2.6 Geoid, Ellipsoid, and Height Systems

The geoid is the equipotential surface (level surface) of the Earth’s gravity field that most closely coincides with the undisturbed ocean surface (and its continuation through the

continents). Disturbances are caused by ocean tides, streams, winds, variations in salinity and temperature, etc, of the order of $\pm 2\text{m}$ [Sjöberg & Bagherbandi, 2017].

In contrast, the reference ellipsoid is a smooth, mathematically defined surface that approximates the shape of the Earth. It is formed by rotating an ellipse about its minor axis (oblate ellipsoid) and is characterized by parameters such as semi-major and semi-minor axes. The ellipsoid is globally fitted to match the geoid as closely as possible. Importantly, the normal potential on the reference ellipsoid is defined to be equal to the actual geopotential on the geoid surface [Sjöberg & Bagherbandi, 2017].

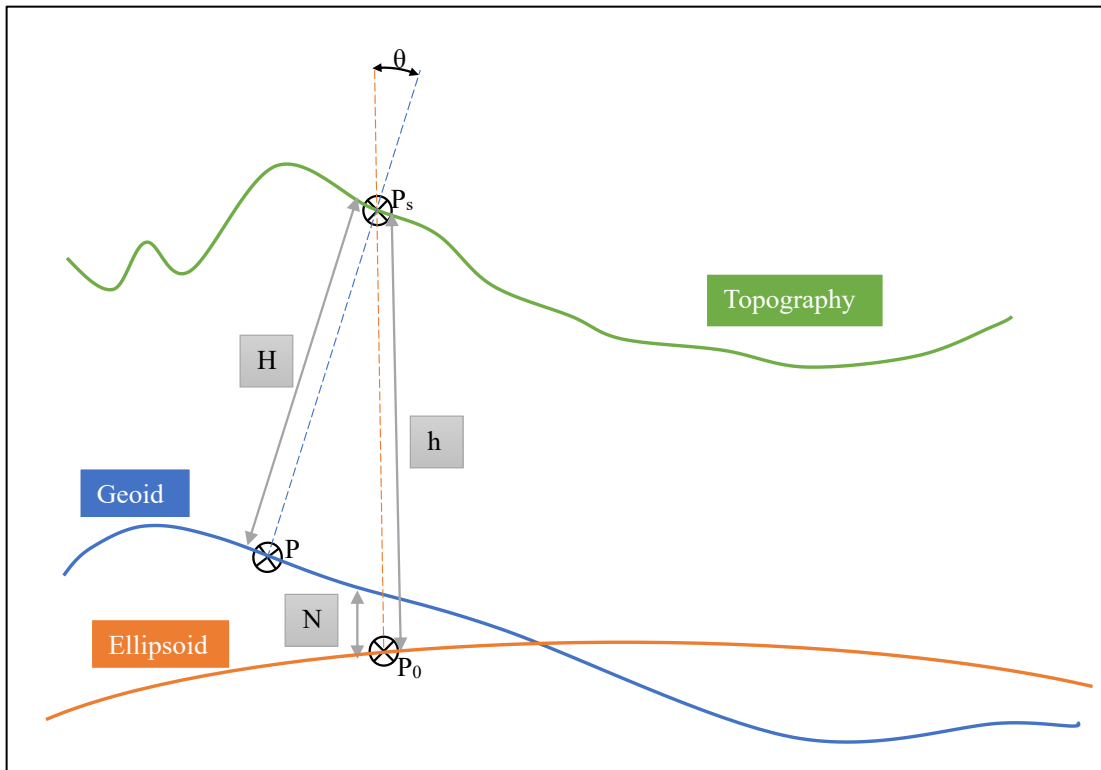


Figure 2.1 Geometric relationship between topography, geoid, and ellipsoid.

Figure 2.1 provides a geometric interpretation of the relationship between the Earth's topography, geoid, and ellipsoid. The green curve represents the surface of the Earth (topography). The blue curve denotes the geoid. The orange curve represents the reference ellipsoid, which may lie above or below the geoid depending on location.

Let us consider a point ' P_s ' on the Earth's surface. The blue dashed line indicates the curved plumb line, or direction of gravity, passing through ' P_s ' and intersecting the geoid at point ' P '. The orange dashed line shows the ellipsoidal normal, intersecting the ellipsoid at point ' P_0 '.

From this geometry, several important height-related quantities are defined:

Orthometric Height (H): The height of point P_s above the geoid, measured along the curved plumb line.

Ellipsoidal Height (h): The height of point P_s above the reference ellipsoid, measured along the ellipsoidal normal.

Geoid Undulation (N): The separation between the geoid and the ellipsoid along the ellipsoidal normal, i.e., between points P and P_0 .

Deflection of the Vertical (θ): The angle between the plumb line and the ellipsoidal normal at point P_s .

Assuming the deflection of the vertical is small, which is often acceptable for regional studies, the geoid undulation can be approximated as:

$$N \approx h - H \quad (2.8)$$

This equation forms the basis for geometric geoid determination, wherein h is obtained using GNSS/GPS measurements and H from spirit levelling. However, the focus of the present study is to determine N by gravimetric methods, using gravity anomalies rather than direct height differences.

2.7 Gravity Disturbance and Gravity Anomaly

In physical geodesy, gravity values are typically referenced to a known surface. This gives rise to two important derived quantities: gravity disturbance and gravity anomaly, which differ based on the reference point to which gravity is reduced.

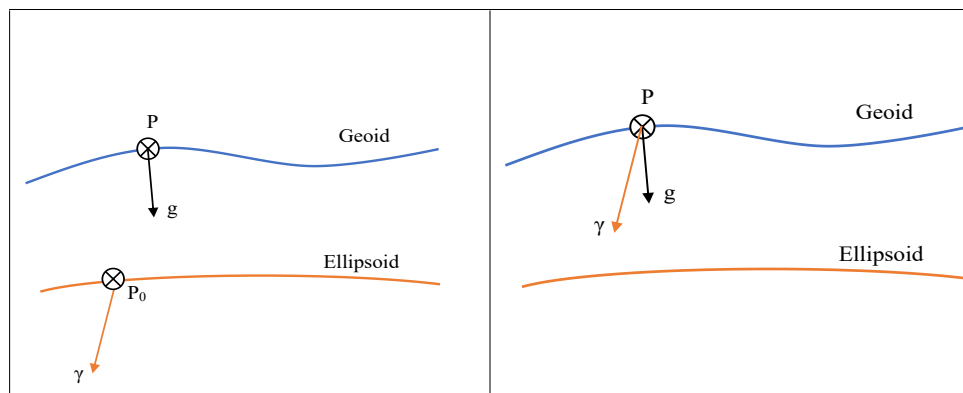


Figure 2.2 Difference between gravity anomaly(left) and gravity disturbance(right)

Gravity Anomaly (Δg):

The difference between the gravity reduced to the point P on the geoid and the normal gravity computed at the ellipsoidal point P_0 :

$$\Delta g = g(P) - \gamma(P_0) \quad (2.9)$$

This requires downward continuation of the surface gravity to the geoid

Gravity Disturbance (δg):

The difference between the gravity reduced to the point P and the normal gravity (γ) at that same point:

$$\delta g = g(P) - \gamma(P) \quad (2.10)$$

This requires upward continuation of the normal gravity on the ellipsoid to the geoid surface.

2.8 Gravity Reduction

In geodesy, gravity measurements are typically taken at points on the Earth's surface, denoted as P_s . The primary objective of gravity reduction is to reduce surface gravity measurements into values that represent the gravity field at the geoid. This adjustment is crucial because; it ensures that gravity data from various elevations are comparable, accurate geoid models require gravity values referenced to the geoid and solutions like Stokes' formula necessitate gravity anomalies defined on the geoid, assuming no external masses above it.

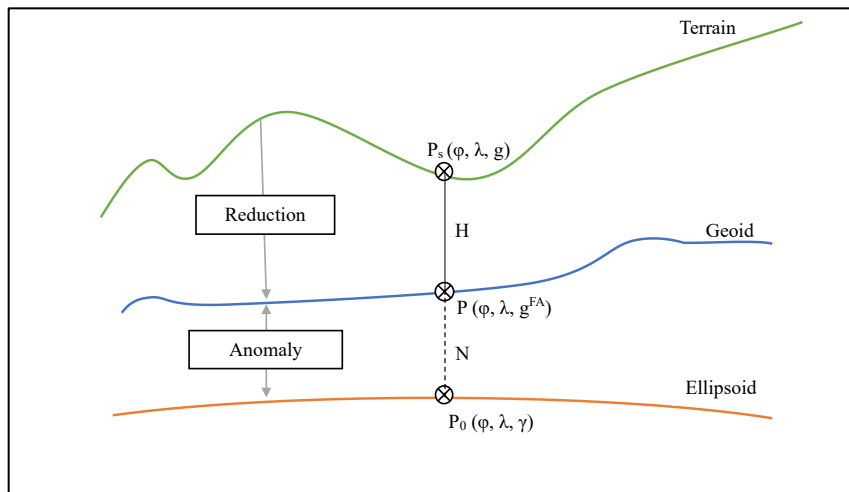


Figure 2.3 Conceptual diagram of gravity reduction in geoid determination

Figure 2.3 conceptually illustrates the process of gravity reduction, which transforms observed gravity measurements taken at the Earth's surface (point P_s) to corresponding values on the geoid (point P) and finally references them to the normal gravity on the ellipsoid (point P_0). The terrain surface represents the actual topography, where gravity is observed as g . To derive the gravity anomaly required in Stokes's formula, the observed gravity must first be reduced to the geoid by applying geometrical corrections (e.g., free-air correction) and physical corrections (e.g., Bouguer and terrain corrections). This intermediate value, denoted g^{FA} , reflects gravity as if the observation were made on the geoid. The anomaly is then computed by subtracting the normal gravity γ at the corresponding ellipsoidal point P_0 . The figure also emphasizes that the reduction involves the conceptual downward continuation of the gravity observation point and the removal of the gravitational effects of topographic masses. This framework is essential for converting heterogeneous gravity observations into a consistent dataset referenced to the geoid, as required by Stokes's integral for geoid computation.

Gravity reductions are primarily categorized into geometrical and physical corrections. Geometrical reductions, such as Free-Air Correction, account for the elevation of the measurement point, whereas physical reductions like the Bouguer and Terrain corrections incorporate the gravitational influence of intervening masses. Together, these corrections aim to remove non-anomalous gravity components and emphasize geophysically significant variations.

2.8.1 Free-Air Reduction

The Free-Air Reduction (FAR) corrects the observed gravity for the elevation of the measurement point above the reference ellipsoid or geoid. It assumes a hypothetical continuation of gravity in free space, neglecting any intervening mass between the surface and the datum. Mathematically, the Free-Air Correction is given by:

$$FAC = -\frac{\partial g}{\partial H} H = 0.3086 H \text{ [mgal]} \quad (2.11)$$

where H is the orthometric height of the observation point above the geoid. The correction factor, often approximated as 0.3086 mGal/m, reflects the vertical gravity gradient near the Earth's surface.

This correction is conceptually straightforward and is typically applied as the first step in gravity reduction. However, since it neglects the gravitational attraction of the material between the station and the reference level, it often overestimates the correction in mountainous regions.

The derivation and explanation of the free-air correction are discussed in detail by Hofmann-Wellenhof and Moritz (2006), where it is emphasized that this correction provides a reference gravity that would be observed if the station were moved vertically down to geoid level without altering the mass configuration of the Earth

2.8.2 Bouguer Reduction

The Bouguer Reduction complements the Free-Air Correction by accounting for the gravitational attraction of the rock mass located between the observation point and the geoid. It assumes the mass is distributed as an infinite horizontal slab (Bouguer plate) of uniform density. The Bouguer correction is expressed as:

$$BC = 2\pi G\rho H \quad (2.12)$$

where ρ is the mean density of the crustal material, typically assumed to be around 2.67 g/cm³, and H is the station height. The positive sign indicates that this mass increases gravity at the station, and its effect must be subtracted to simulate a gravity value at the geoid level.

The combination of Free-Air and Bouguer corrections yields the Simple Bouguer gravity.

$$g_{SB} = g_{obs} + FAC - BC \quad (2.13)$$

However, here the assumption of a flat, infinite slab becomes increasingly invalid in areas with complex topography, leading to the need for further refinement through terrain corrections.

Nico Sneeuw (2004) discusses the physical implications of the Bouguer plate approximation and its limitations in real-world applications. His treatment emphasizes the trade-offs involved in simplifying complex topographic structures into planar approximations.

2.8.3 Terrain Correction

Terrain Correction (TC) refines the Bouguer reduction by addressing the deviations from the flat-slab assumption. It calculates the gravitational attraction of the actual terrain surrounding the observation point, typically within a radius of several kilometers. These

corrections are crucial in regions with rugged relief, where the gravitational effects of nearby valleys and peaks can significantly bias gravity measurements.

The terrain correction is always positive, as the Bouguer plate underestimates gravity in valleys and overestimates it in mountains. Terrain corrections can be computed using digital elevation models (DEMs) and involve numerical integration or prism-based summation of gravitational contributions from topographic masses.

The Complete Bouguer gravity is obtained by including terrain corrections in the Simple Bouguer gravity:

$$g_{CB} = g_{obs} + FAC - BC + TC \quad (2.14)$$

Hofmann-Wellenhof and Moritz (2006) & Sneeuw (2004) acknowledge the computational complexity of terrain corrections. Hofmann-Wellenhof and Moritz (2006) provide analytical insights into regional terrain correction strategies, while Sneeuw (2004) offers modern perspectives on digital implementations using high-resolution DEMs.

2.8.4 Indirect Effects of Gravity Reductions

While gravity reductions serve to normalize gravity observations for meaningful geophysical interpretation, the process is not without fundamental challenges. Even when standard reductions such as the Free-Air, Bouguer, and Terrain corrections are applied with precision, they do not completely eliminate discrepancies between the observed gravity field and the reference potential surface. These residual discrepancies are attributed to what are known as indirect effects, which emerge as a consequence of altering the Earth's mass distribution during the reduction process.

When gravity is reduced from a surface observation point to a reference surface like the geoid, we conceptually remove topographic masses—mountains, plateaus, and valleys—that lie between the observation point and the reference level. However, these masses are integral to the Earth's gravitational potential field. Their removal does not merely adjust the measurement location; it changes the very shape and configuration of the equipotential surfaces themselves. In effect, the original geoid, defined by a specific gravitational potential, is no longer valid once the mass distribution has been altered. A new equipotential surface, still possessing the same potential value, emerges in a different location. This new surface is referred to as the co-geoid.

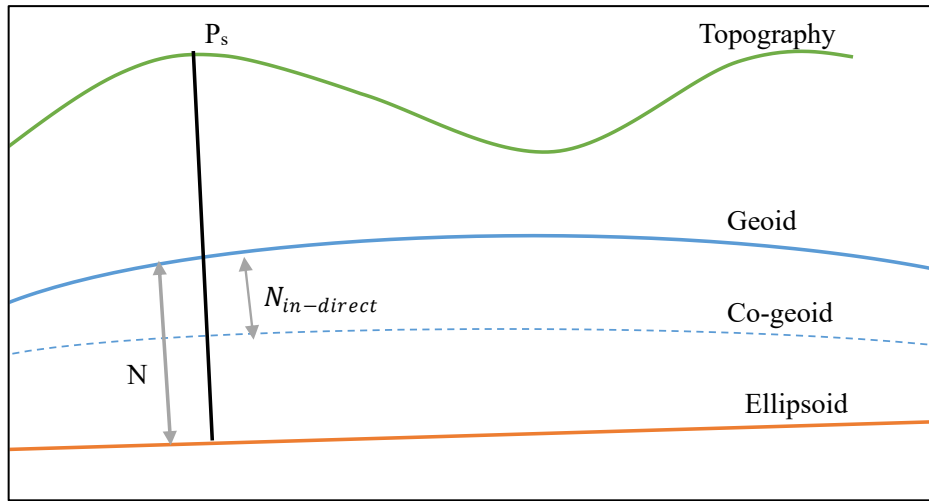


Figure 2.4 Conceptual representation of co-geoid

Figure 2.4 illustrates the geometric relationship between the topographic surface, geoid, co-geoid, and the reference ellipsoid in the context of indirect effects. The point P_s represents the location where gravity is observed on the terrain. In standard gravity reduction procedures, masses above the geoid are mathematically removed to simulate a reference field without topography. However, this removal alters the gravitational potential field, causing the original geoid to shift. As a result, the equipotential surface computed after mass removal, shown as the co-geoid, is no longer aligned with the true geoid. The vertical distance between the geoid and co-geoid is referred to as the primary indirect effect, denoted $N_{in\text{-}direct}$. It represents the correction required to reconcile the displacement of the reference surface due to the terrain mass removal. This shift must be accounted for to maintain consistency in high-precision geoid modelling using Stokes's formula.

Ignoring indirect effects, especially in regions with significant topographic variation, can introduce non-negligible errors in geoid height estimation. Their inclusion is therefore essential in high-accuracy geodetic computations. Texts such as Hofmann-Wellenhof and Moritz's Physical Geodesy provide a detailed discussion of these effects, emphasizing their theoretical necessity and practical implementation in gravity field modelling.

2.9 Geoid Height and Bruns' Formula

A Taylor expansion of the normal potential U along the ellipsoidal normal gives the disturbing potential at the geoid T as:

$$T = W - U \approx N \gamma \quad (2.15)$$

Where:

- W : geopotential on the geoid,
- U : normal potential at the same point,
- γ : normal gravity on the ellipsoid.

From this, the Bruns' formula is derived:

$$N = T / \gamma \quad (2.16)$$

This formula assumes that the disturbing potential is known at the point of interest and that the normal gravity γ is computed at the corresponding point on the reference ellipsoid. Bruns' formula is fundamental in geoid determination, allowing for the computation of geoid heights from gravity measurements. So, the gravity measurements we do must be linked to disturbing potential and then only we can find geoid undulation. How to link gravity to disturbing potential is discussed in the next section.

2.10 Fundamental Equation of Physical Geodesy

The fundamental equation of physical geodesy establishes a relationship between the gravity anomaly and the disturbing potential. It is derived by considering the vertical derivative of the disturbing potential and the variation of normal gravity with height:

$$\Delta g = - \frac{\partial T}{\partial h} + \frac{\partial \gamma}{\partial h} T \quad (2.17)$$

In this equation:

- Δg is the gravity anomaly.
- $\partial T / \partial h$ is the vertical derivative of the disturbing potential.
- $\partial \gamma / \partial h$ is the vertical derivative of the normal gravity.
- γ is the normal gravity at the point of interest.

This equation is pivotal in geodesy as it links observable quantities (gravity anomalies) to the disturbing potential, facilitating the modelling of the Earth's gravity field.

For many practical applications, especially those involving global or regional scales, the Earth's shape can be approximated as a sphere. Under this approximation, the fundamental equation simplifies to:

$$\Delta g = -\frac{\partial T}{\partial r} - 2 \frac{T}{r} \quad (2.18)$$

Here:

- r is the radial distance from the Earth's center.
- $\partial T/\partial r$ is the radial derivative of the disturbing potential.

This first-order differential equation, known as the fundamental equation of physical geodesy, was first solved by Stokes in 1849 and forms the basis for deriving the disturbing potential from surface gravity data.

2.11 Stokes Formula

Stokes' formula (Stokes 1849) is the solution to the differential equation given above

$$T = \frac{R}{4\pi} \int_{\lambda=0}^{\lambda=360} \int_{\phi=0}^{\phi=180} \Delta g S(\psi) d\sigma \quad (2.19)$$

In this equation, R represents the Earth's mean radius. Δg is the gravity anomaly. The integration is performed over the solid angle $d\sigma$, a surface element on a unit sphere defined as $d\sigma = \cos\phi d\phi d\lambda$, where ϕ and λ are the geodetic latitude and longitude.

Central to the integral is the Stokes function $S(\psi)$ also known as the Stokes kernel. This function plays a crucial role by weighting the gravity anomaly data based on the angular distance ψ , which is the spherical angle between the evaluation point for the geoid height and the location of the gravity anomaly measurement, as seen from the Earth's center. The Stokes kernel (equation 2–305 in Hofmann-Wellenhof & Moritz, 2006) is given by the expression:

$$S(\psi) = \frac{1}{\sin \frac{\psi}{2}} - 6 \sin \frac{\psi}{2} + 1 - 5 \cos \psi - 3 \cos \psi \ln \left(\sin \frac{\psi}{2} + \sin^2 \frac{\psi}{2} \right) \quad (2.20)$$

The practical computation of these formulas are discussed in chapter 5.

Chapter 3. Literature Review

As noted by Reguzzoni et al. (2021), GNSS-levelling provides a very efficient technology to obtain ellipsoidal heights an indispensable requirement is the precise knowledge of the geoid. In practice, high-resolution gravimetric geoids are used to define consistent vertical datums over a region. They underpin engineering, surveying, and geoscientific applications that depend on accurate physical heights. Key geodetic roles of regional geoid models include, converting GNSS-derived ellipsoidal heights to orthometric (physical) heights, defining a consistent vertical datum and unifying height systems within a region and supporting surveying, engineering, and scientific tasks that rely on accurate physical heights. In all, a high-precision regional geoid enables GNSS to be used for practically any height-related application by providing the tie to local sea level (or vertical datum).

3.1 Limitations of Global Geoid Models in High-Relief Terrain

Global geopotential models (e.g. derived from CHAMP/GRACE/GOCE satellites) have greatly improved our knowledge of the Earth’s gravity field at long wavelengths. However, these models inherently smooth short-wavelength signals because of the high altitude of their satellite orbits. Consequently, the finest gravity features – which are critically important in mountainous regions – are not resolved by global models alone. This limitation has been quantified in practice. For example, Smith and Milbert (1998) found that geoid errors from a global model (EGM96) can exceed 1.5–3 meters in very rugged terrain (e.g. the Himalayas and Rocky Mountains). In other words, over steep peaks and valleys a satellite-only geoid may be off by well over a meter. Such errors are unacceptable for modern cm-level geodesy.

In our study area – the Durango–Walsenburg region of southwestern Colorado – these issues are acute. This area was used as a GNSS/levelling reference test (NGS GSVS17) precisely because of its extreme relief. Elevations range from about 314 m to 4385 m within this region. In such high-relief terrain, the short-wavelength gravity anomalies are large and global models smooth them out. Therefore, global geoid models alone cannot meet precision requirements in this setting.

These limitations make clear that regional geoid refinement is necessary in high-relief areas like our Colorado study site. Detailed, high-resolution gravity information is needed to capture the missing geoid signal lost in the satellite models.

3.2 Airborne Gravimetry for Regional Geoid Modelling

Airborne gravity surveys provide a critical means of filling the data gaps in such regions. Modern aircraft-borne gravimeters can continuously collect medium-scale gravity data (spatial scales of a few to hundreds of kilometres) over challenging terrain. This capability complements sparse ground measurements, “filling the gaps” across mountains where land surveys are impractical. Many countries have conducted airborne gravity campaigns in recent decades to update their gravity databases and height systems (e.g. USA’s GRAV-D project, Turkey, New Zealand, etc.). In the U.S., the GRAV-D program has systematically flown high-altitude surveys over the western mountains, providing an unprecedented set of gravity measurements for geoid computation.

Studies in the Colorado region show the tangible benefits of these data. For instance, Jiang and Wang (2020) demonstrated that including GRAV-D airborne data in the geoid solution reduced the model’s root-mean-square error from about 5.8 cm down to 5.3 cm. Likewise, Varga et al. (2021) found that combining terrestrial and airborne gravity improved geoid accuracy by roughly 1.1 cm ($\approx 20\%$ better standard deviation) compared to using terrestrial data alone. These results confirm that airborne measurements significantly enhance model precision in high-relief areas. Moreover, airborne geoid studies in other countries show similar gains whenever such data are incorporated.

3.3 Classical Remove–Compute–Restore (RCR) Geoid Modeling

The remove–compute–restore (RCR) approach is a classical Stokes-based method for regional geoid determination. In RCR, a long-wavelength reference field (from a global geopotential model) is removed from gravity data, a residual geoid is computed (typically by Stokes’ integral or its modifications), and then the removed field plus other effects (e.g. terrain) are restored to obtain the full geoid. Formally, one subtracts the normal-gravity component and the long-wavelength disturbing potential (from a GGM) from the observed anomalies, computes the high-frequency geoid via a 2-D Stokes convolution (often using FFT for efficiency), and then adds back the GGM-derived geoid heights and terrain corrections. Over time, this basic workflow has been refined: FFT implementations (applying full zero-padding to approximate spherical integration) were

introduced to speed up Stokes integrals and mitigate spherical truncation issues. Authors like Tziavos (1993) and Sideris and Li (1993) added padding and tapering techniques to improve the FFT geoid. Meanwhile, the reference field subtraction and terrain treatment have been developed through Molodensky's normal-field approaches and Helmert condensation methods. In practice, the key RCR steps can be summarized as: remove a high-degree GGM (e.g. up to degree n), remove local topographic effects; compute the residual geoid (usually via FFT-accelerated Stokes convolution); then restore the GGM and terrain contributions. Notably, Abdalla and Green (2015) outline these steps: remove the GGM field from terrestrial gravity, compute the residual geoid via FFT, and finally add back the GGM geoid and FFT-computed terrain corrections.

The RCR method has proven adaptable and effective in many regions. For example, Hirt et al. (2019) demonstrate that modern high-resolution terrain models greatly enhance RCR accuracy: they created a 3" (~ 90 m) global gravimetric terrain correction grid based on SRTM to capture topographic gravity. In geoid modeling, high-res Digital Elevation Models (like NASA's SRTM 1"-arc (~ 30 m) data) are essential for accurate terrain reduction: they allow the short-range prism summations or residual terrain model (RTM) corrections needed in RCR. Hirt et al. (2019) emphasize that 90 m resolution topographic corrections significantly improve the removal of mountainous signals. Similarly, rigorous methods (e.g. the RTM approach of Forsberg and Tscherning) use SRTM-based models to compute both direct terrain corrections and the so-called atmospheric correction due to topography (the “topography-bounded atmosphere”). Together, these ensure that the observed gravity anomalies (free-air) can be reduced correctly to the geoid. In effect, high-res DEMs smooth the data and remove local masses, which is critical in regions with strong relief.

3.4 Downward Continuation of Airborne Data

Airborne gravimetry (such as GRAV-D) measures gravity at flight altitudes (typically 4–11 km in GRAV-D). Before using these data in Stokes' integral, they must be downward-continued to the reference (surface) level. Various methods have been explored for this, including spectral continuation (spherical-harmonic truncation), inverse Poisson, least-squares collocation (LSC), radial basis functions (RBF), and analytic (Moritz's method). Li and Huang (2019) compared four DC methods (LSC, inverse Poisson, truncated spherical harmonics, RBF) on GRAV-D airborne data (including Colorado) and found significant differences: truncated spherical harmonics lost ~50% of the gravity signal

compared to LSC/RBF, LSC introduced an unknown bias, and inverse Poisson suffered numerical instability in rough terrain. In contrast, Li et al. (2022) compared six DC techniques and reported that all produce similar geoid results when optimally configured – but LSC stood out as most robust. They found comparable geoid quality among methods but noted that LSC (with an appropriate covariance) was more stable and thus recommend LSC for GRAV-D data (using other methods only as a check). In practice, then, downward continuation must be performed carefully (often by LSC), since errors in this step (especially in mountainous regions) can degrade the geoid. Overall, studies conclude that with proper implementation all standard DC methods yield similar final geoid accuracy, although LSC offers flexibility (especially for high-altitude data).

3.5 FFT-Based Stokes and Terrain Corrections

The compute stage of RCR often leverages Fast Fourier Transform (FFT) to implement the Stokes convolution efficiently. In this planar-approximation, 2-D convolution form of Stokes' integral, FFT can dramatically speed up the computation over a gridded domain. For example, Abdalla and Green (2015) describe reformulating Stokes' formula into a 2D convolution on a grid and computing it via FFT. This approach was originally developed in the 1980s (e.g. Sideris 1987; Schwarz et al. 1990) and refined with zero-padding to address the limited area approximation. In RCR, FFT is also used to compute terrain corrections. For instance, Liu et al. (2023) applied FFT to the residual terrain model (RTM) data from a 1" SRTM DEM, calculating the combined effect of near-range topography on the residual gravity field to be included in the restoration step. In summary, the FFT-accelerated method allows both the residual-geoid (Stokes) computation and the high-resolution terrain (RTM) reductions to be done quickly on large grids. This FFT-based RCR is especially advantageous in regional contexts (like a 700×550 km window in Colorado) because it handles dense grids and multiple corrections rapidly.

3.6 Global Geopotential Models and Data Integration

The remove step in RCR relies on a global geopotential model (GGM) to provide the long-wavelength gravity signal. In practice, one selects a GGM (e.g. EGM2008, EIGEN-6C4, or a GRACE/GOCE hybrid like GGM05G) up to a certain degree and subtracts its corresponding gravity anomalies (or disturbing potential) from the data. Recent studies emphasize choosing high-quality models: Liu et al. (2023) compared five GGMs (EGM2008, three GOCE-based, etc.) and found large differences in their low-degree error

spectra. Notably, GOCE-enhanced models had much lower error than EGM2008 at mid-frequencies. In their Colorado case, the GOCE+GRACE model XGM2016 exhibited minimal cumulative error up to degree 719 (≈ 1.1 cm) and was chosen for the RCR reference field. Once the GGM field is removed, the remaining gravity (and airborne) anomalies contain only high-frequency content resolvable by the data. After computing the residual geoid, the GGM’s geoid (and any removed spherical topography terms) is restored. This integration of GGM with local data is crucial: it injects long-wave gravity missing from the regional gravity surveys. In summary, GRAV-D based RCR typically uses a modern GGM (such as GGM05G or similar) truncated to some degree (often 720–2160) and adds its geoid back in the final sum, ensuring that both satellite and terrestrial signals are consistently combined.

3.7 Indirect Topographic Effects

A special consideration in gravimetric geoid modelling is the indirect topographic effect. This arises because Stokes’ formula (which assumes all mass is above a reference surface) does not inherently account for the gravitational effect of the missing mass below the reference ellipsoid. In modern terms, an indirect correction must be applied to account for the difference between the actual density distribution and the normal Earth (Molodensky’s approach). Sjöberg (2018) stresses that neglecting this correction would cause geoid errors of meters in rugged areas. In practice, the primary indirect topographic effect (PITE) is computed (often via an integral over the topography with a factor involving the normal potential), and sometimes a secondary effect (SITE) is added for full consistency. The challenges are that ITE requires an assumed density model for the topographic material; any error in density leads directly to geoid error. Modern geoid routines (including NGS’s GRAVSOFT) include ITE or equivalently apply a Helmert condensation so that the result matches the geoid height definition. In RCR terms, one usually adds the indirect correction in the restore step (often as part of “additive corrections” in a Least-Squares Stokes approach). Overall, accurately modelling the indirect effect is as important as the direct terrain correction, especially in high-relief areas.

3.8 Validation with GNSS/Levelling Data

Regional geoid models are typically validated against high-quality GNSS/levelling benchmarks. In rugged U.S. terrain, the GSVS17 (Geoid Slope Validation Survey 2017)

network in Colorado provides such independent data. This data set of precise GPS and levelled orthometric heights along a ~250 km transect allows testing of geoid height estimates at the ~cm level. For example, the Colorado 1-cm geoid experiment (IAG WG2.2.2) used GSVS17 to compare geoid solutions from many teams. Results showed that the best models had 2–3 cm RMS agreement with GSVS17 (falling short of 1 cm). Such validation underscores the inherent difficulty in mountains: even with GRAV-D and terrain corrections, standard deviations of differences ranged 2–8 cm. In practice, a successful RCR implementation should match the GNSS/levelling within a few cm.

3.9 Case Studies and Comparative Approaches

Several case studies illustrate RCR’s performance in mountainous settings. In the Colorado 1-cm experiment, fourteen international groups computed geoid/quasigeoid models from the same GRAV-D and levelling data. Their (quasi)geoid models agreed around 2 cm overall. Importantly, differences between methods were mainly due to data processing choices rather than theory: as one summary notes, “the differences are not primarily caused by differences in theory, but originate from numerical computations and/or data processing techniques”. In a direct GRAV-D study, Varga et al. (2021) used an RCR-type (LSM) method in Colorado: they found that adding the downward-continued airborne data to terrestrial gravity improved geoid accuracy by ~1.1 cm (20%) relative to using terrestrial data alone. This quantifies the benefit of GRAV-D in a classical geoid solution.

Comparisons of RCR versus modern methods show generally compatible results. For instance, Abdalla and Green (2015) compared RCR (FFT-Stokes), LSM (Stokes+corrections), and collocation in Sudan and found the three methods “showed comparable results” (differences $\lesssim 5$ mm after levelling bias removal). However, some studies report that the least-squares modification (LSM) with additive corrections can slightly outperform a plain FFT-based RCR in complex terrain. For example, in central Turkey Abbak et al. (2012) showed that LSM (plus additional surface-gravity fitting) gave a noticeably better fit than RCR under sparse gravity sampling. Yildiz et al. (2012) likewise found RCR, LSM, and LSC (collocation) solutions were essentially equivalent once a common bias was removed. Overall, both classical RCR and modern collocation-based approaches can achieve similar cm-level accuracy if carefully implemented. Notably, the KTH collocation method (a least-squares combination of Stokes and satellite contributions) is known to theoretically include all indirect effects and provides a

sophisticated cross-check, but it does not automatically yield superior accuracy unless all parameters (covariances, densities) are well modelled. In summary, regional experiments indicate that classical RCR remains competitive with modern techniques in mountainous US regions, especially when using the high-resolution DEM, high-quality GGMs, and careful downward continuation as described above.

3.10 Recent Advances and Future Directions

Emerging research indicates that artificial intelligence algorithms can adapt to spatial variability, "enabling the development of geoid models that are more locally accurate and adaptable to specific geographic conditions". This adaptive capability is particularly valuable in mountainous regions where traditional mathematical models may struggle with extreme variations in terrain and gravity.

Machine learning approaches offer the potential to identify complex patterns in the relationship between gravity measurements, topography, and geoid heights that might not be apparent in conventional physical models. As computational resources improve and training data expands, these methods may help bridge the gap between current 2-3 cm accuracy and the aspirational 1 cm target.

High-resolution regional gravity field modelling using band-limited spherical radial basis functions represents another significant advance. This approach effectively captures detailed gravity field variations in mountainous terrain by providing adaptive spatial resolution that conforms to the complexity of the local gravity field.

Wang et al. (2021) demonstrated that transforms in the frequency domain can provide "higher processing efficiency and accuracy, which solves the problem of data missing and edge expansion in both downward continuation and vertical integration". Such mathematical refinements continue to improve both the computational efficiency and physical fidelity of geoid models.

The ongoing refinement of regional geoid models will benefit from new observation types and improved measurement technologies. Future advances may incorporate satellite gravity gradiometry, quantum gravity sensors, and improved airborne systems with higher resolution and accuracy. The integration of these diverse data sources will require sophisticated statistical approaches to handle their different error characteristics and spatial resolutions

Chapter 4. Study Area and Data Sources

4.1 Study Area

The study area is geospatially situated within the broader NGS GRAV-D survey block designated as MS05 (Mountain South 05), which spans multiple states including Colorado, New Mexico, Kansas, Oklahoma, and Texas. Block MS05 covers an area of approximately 610 km by 295 km and was surveyed as part of NOAA's Gravity for the Redefinition of the American Vertical Datum (GRAV-D) project. Although the full Block MS05 spans a larger region, the geoid modelling performed in this project is confined to a smaller, well-constrained $1^\circ \times 1^\circ$ region within southwestern Colorado, bounded by latitudes $37^\circ\text{--}38^\circ\text{N}$ and longitudes $107^\circ\text{--}108^\circ\text{W}$.

The selected modelling area overlaps directly with a portion of the GSVS17 (Geoid Slope Validation Survey 2017) corridor, which lies along U.S. Highway 160 between Durango and Walsenburg. Elevations along this transect vary from approximately 1900 meters to over 3300 meters, capturing a diverse set of terrain-induced gravitational effects essential for testing the fidelity of geoid models.

The extent of the GRAV-D Block MS05, the specific $1^\circ \times 1^\circ$ geoid modelling region, the underlying digital elevation model, and the location of the GSVS17 ground survey benchmarks are depicted in figure 4.1 through a set of multi-scale maps. These maps provide both regional and national geographic context for the study. The top panel presents the SRTM 1 arc-second (~ 30 m) Digital Elevation Model (DEM), highlighting the rugged topography of southern Colorado, with GSVS17 survey points aligned along U.S. Highway 160. The middle panel situates the $1^\circ \times 1^\circ$ modelling window ($37^\circ\text{--}38^\circ\text{N}$, $107^\circ\text{--}108^\circ\text{W}$) within the broader GRAV-D MS05 airborne gravity survey block, outlining the coverage of the CO17-1 campaign conducted by the National Geodetic Survey. The bottom panel places the entire study area within the larger map of the contiguous United States, showing surrounding state boundaries in magenta. Together, these visual elements illustrate the integration of high-resolution gravity, topographic, and geodetic data used in this regional geoid modelling effort.

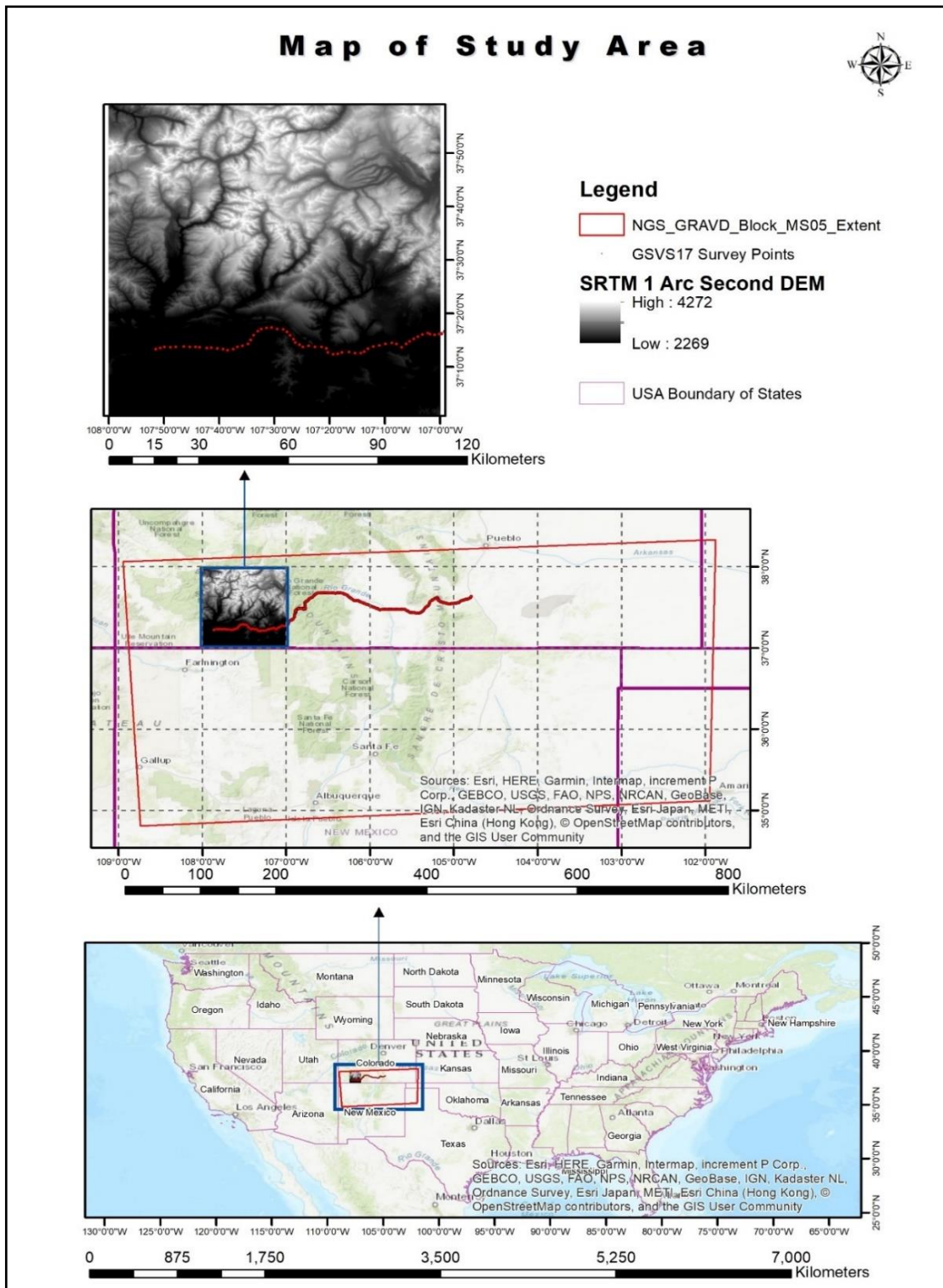


Figure 4.1 Study area map showing the location and context of the geoid modelling region in southwestern Colorado within the broader GRAV-D Block MS05

4.2 Airborne Gravity (GRAV-D)

The U.S. National Geodetic Survey (NGS) is conducting an ambitious project, GRAV-D (Gravity for the Redefinition of the American Vertical Datum), to improve the Nation's

vertical height system. In particular, GRAV-D will deliver high-quality gravity data so that orthometric heights (heights above the geoid, which closely approximate mean sea level) can be computed rapidly and accurately.

GRAV-D uses specialized terminology to describe its survey areas and operations. For example, a “block” is defined as a pre-planned geographic survey area (usually several thousand square kilometers) with enough internal flown and cross-over lines to yield robust error statistics. A “survey” refers to a specific data-collection campaign, typically conducted by a field team at a particular airport with specific aircraft and instruments. The project’s documentation uses these terms to differentiate data coverage areas (“blocks”) and individual field deployments (“surveys”).

All GRAV-D airborne gravity and related data products are made publicly available through NOAA’s GRAV-D data distribution portal. A Google Maps–based data portal on the GRAV-D website shows the status of each block (planned, in progress, or released), and provides direct links to the block-specific download pages. When data for a block are released, the portal highlights the block and provides a link. Each block’s download page includes a Google map of the flown lines, and a downloadable ZIP archive containing all data and documentation for that block. Typical contents of a block’s ZIP file include: a ReadMe, the official gravity data file, supplementary data (e.g. cross lines, transit lines), metadata, and KML files for the block outline and line locations.

The planning of GRAV-D survey blocks takes into account several critical considerations to ensure data quality and operational efficiency. One key factor is the orientation and complexity of the local gravity field, which influences the optimal direction of survey lines to best capture gravity-field trends. Airport accessibility is also a major consideration; block boundaries are designed with the locations of nearby airports in mind to facilitate take-off and landing logistics. In regions with challenging topography, such as mountainous areas, blocks are sized to allow safe and practical flight altitudes that maintain adequate ground clearance. Additionally, each survey line is planned to be long enough to encompass relevant geological features, yet short enough to be completed within a single flight given the aircraft’s fuel capacity and operational limits. The spacing of flight lines is carefully selected to ensure sufficient sampling density, both along and across the flight path, to accurately characterize the gravity field. A minimum cross-line spacing is maintained to allow for the detection and estimation of systematic errors and

instrument drifts through crossing error analysis. Finally, to ensure continuity and consistency, adjacent blocks are designed to slightly overlap or align with previous surveys, allowing gravimetric data sets to connect seamlessly and enabling gravimetric offsets to be properly adjusted.

The nominal altitude for most GRAV-D airborne surveys is 20,000 ft (\approx 6,096 m). This altitude is chosen as a compromise: it is low enough to preserve mid-scale gravity signal, yet high enough that a long line (e.g. 500 km) can be flown in roughly one hour. Flying higher generally reduces the sensitivity to short-wavelength gravity anomalies (making resolution coarser) but allows longer lines (since the aircraft can stay at altitude longer). Flying lower improves sensitivity to small-scale features but shortens flight endurance. The 20,000-ft nominal altitude thus balances recovery of mid-wavelength gravity features against practical issues (such as airline traffic, aircraft performance, and survey duration). In fact, at 20,000 ft a 500-km line can be completed in just over 60 minutes, which matches the endurance of typical GRAV-D aircraft on station.

A key limitation on airborne gravity resolution is simply the flight altitude. Childers et al. (1999) quantified this by defining a “geologic wavelength” (λ_g) that characterizes the smallest anomaly size recoverable at a given altitude. λ_g depends on the aircraft height (z_c) above the anomaly centre. For flat terrain surveys, z_c is simply the flight altitude.

$$\lambda_g = 1.54 z_c \quad (\text{Childers et al., 1999, Eq. 1})$$

Roughly speaking, higher altitude yields larger λ_g , meaning only longer-wavelength features are detectable. There is also a related concept of the fourier wavelength (λ_f), which represents the surface wavelength of that anomaly in the gravity field spectrum. For a given geologic wavelength and survey altitude, λ_f is twice larger than λ_g .

$$\lambda_f = 2\lambda_g \quad (\text{Childers et al., 1999, Eq. 2})$$

For the GRAV-D nominal altitude of 20,000 ft (6096 m), the calculations show that the minimum recoverable geologic wavelength is about 9.4 km (and the corresponding Fourier wavelength about 18.8 km). In practical terms, this means that no feature significantly smaller than \sim 20 km across can be resolved in the airborne gravity data at this altitude for flat terrain. (Terrain relief tends to help: if surveying over mountains or valleys, the effective altitude above the anomaly center is less, so the Fourier wavelength shrinks and somewhat smaller features can be detected.) This example illustrates the

trade-off: at 20,000 ft the survey is essentially “blind” to anomalies narrower than on the order of 10–20 km. Conversely, flying lower (say 10,000 ft) would roughly halve λ_g and improve resolution of smaller targets, at the cost of shorter line length and more severe atmospheric turbulence effects.

Besides altitude effects, the survey line spacing also limits resolution by the Nyquist sampling theorem. GRAV-D typically flies lines on a 10-km grid. By Nyquist, the smallest cross-track wavelength that can be sampled without aliasing is twice the line spacing, i.e. about 20 km. In other words, even if the altitude allowed it, the gridding of the data enforces that features smaller than ~20 km in the north-south (cross-line) direction cannot be reliably recovered without aliasing. (With denser line spacing, such as 5 km, the cross-track resolution would improve correspondingly to ~10 km.) Along-track resolution (east-west direction) is governed by how fast the aircraft flies, the sampling rate of the gravimeter, and any low-pass filtering applied. Typically, the aircraft speed (hundreds of knots) and modern instruments yield very fine raw sampling (meters to hundreds of meters), so along-track resolution is often better than the cross-track resolution.

In summary, for the nominal GRAV-D block configuration (20,000 ft altitude, 10-km line spacing), the effective feature resolution is on the order of 20 km. That is, the gravity field can be reliably mapped down to ~20-km spatial scales. Filtering and noise further affect resolution: data are generally low-pass filtered to remove high-frequency noise, but field quality control (and possible re-flights) aims to minimize the need for aggressive filtering.

Each block’s documentation (the Block Airborne Gravity Data User Manual) will summarize parameters for that area: the actual flight altitude, line spacing, nominal and achieved resolutions, and any special processing notes. In all cases, GRAV-D’s planning and QC procedures emphasize consistency and accuracy, so that the resulting gravity data meet the project’s strict requirements for updating the national vertical datum.

GRAV-D employs the Micro-g LaCoste Turn-key Airborne Gravimetry System (TAGS), a beam-type, zero-length spring gravimeter mounted on a gyro-stabilized platform. The TAGS unit provides high precision (0.01 mGal in laboratory conditions), incorporates horizontal accelerometer outputs, and features user-friendly computerized control with digital data recording.

Operational protocols for GRAV-D surveys are designed to ensure data stability and accuracy throughout the mission. Each day begins with morning still readings taken

before flights to stabilize the gravimeter system and establish a baseline. During survey operations, the system remains continuously active across multiple flights, with intermediate still readings conducted between sorties to monitor for instrument drift or tares. The gravimeter is integrated with a NovAtel DL4 Plus or DLV3 GPS receiver, which provides precise real-time positioning and timing information. This is achieved through GPS signals in combination with an internal rubidium clock, ensuring synchronization and high temporal accuracy of the gravity measurements. Nearly all GRAV-D aircraft carry a secondary GPS system integrated with an Inertial Measurement Unit (IMU), providing attitude data (pitch, roll, yaw, true heading) essential for correcting gravimeter readings. In the absence of IMU data, GPS redundancy is ensured by a backup TAGS timing unit.

At the airport base, one or two GPS base stations are deployed near the aircraft parking area. These base stations enable differential GPS processing and serve as backups in case Precise Point Positioning (PPP) solutions do not meet accuracy thresholds.

For accurate calibration, a gravity tie is performed using a field-tested absolute gravimeter (MGL A-10) at the specific location of the TAGS unit. Relative gravimeters measure vertical gradients to correct for differences in sensor height, allowing conversion of gravimeter outputs from arbitrary units to physical gravity units (m/s^2 or mGal).

GRAV-D utilizes Newton, a custom MATLAB-based software developed by the National Geodetic Survey (NGS), to process airborne gravimetry data with the precision and accuracy required for the project's high-altitude, high-speed surveys. The gravity data processing workflow begins with the re-computation of gravimeter readings in accordance with TAGS operational guidelines. GPS and gravity data are then synchronized to within 0.01 seconds to ensure temporal alignment. Several critical corrections are applied, including those for aircraft motion—such as Eötvös and vertical acceleration effects—gravimeter tilt (off-level correction), and instrument drift. The data are further refined using a time-domain Gaussian filter, which is applied three times to smooth out noise while preserving signal integrity. Flight tracks are carefully edited and trimmed to exclude segments affected by significant aircraft manoeuvres that could compromise data quality. Finally, internal consistency checks, such as cross-over analysis and line-to-line correlation, are conducted to validate the reliability and coherence of the processed gravity data.

4.3 Global Geopotential Model (GGM05G)

In a remove–compute–restore (RCR) geoid computation, the choice of the base global gravity model directly affects which spectral bands are removed a priori. GGM05G, a global geopotential model derived only from GRACE and GOCE satellite data, contains predominantly long-wavelength (low-degree) gravity signals. In practice, GGM05G extends to spherical harmonic degree 240 but, by construction, lacks any terrestrial or airborne data. Thus it represents a “smooth” global field (akin to EGM08’s long-wavelength portion) without local short-wavelength detail. Using GGM05G in the remove step of RCR means that only the broad-scale (long-period) geoid undulations are subtracted from the observations, avoiding inadvertent subtraction of medium- or short-wavelength signals. In effect, low-degree geopotential harmonics (which correspond to wavelengths of hundreds to thousands of kilometres) are removed, while the finer-grained anomalies remain for subsequent modelling. This is advantageous because it prevents high-frequency regional signals from “leaking” into the removed component and ensures that the compute stage (using local data) can recover the full shorter-wavelength geoid details.

The use of GGM05G for the RCR method guarantees that the remove step subtracts only the intended large-scale field. In contrast, if one were to use a full-resolution model in the remove step, medium- and short-wavelength content present in that model would also be subtracted, leaving less signal for the compute stage.

By contrast, the Earth Gravitational Model 2008 (EGM2008) is a combined global geopotential model that already integrates satellite, terrestrial, and airborne data. EGM2008 is complete to spherical harmonic degree and order 2159 (and includes extra coefficients to 2190), and its data merge explicitly terrestrial gravity measurements, satellite altimetry-derived gravity, and airborne surveys. In practice, using EGM2008 as the “remove” model would imply subtracting all of these signals (including medium- and short-wavelength components) at once. This could inadvertently remove much of the same detail that one intends to model locally, effectively leaving little residual for the compute stage. In other words, EGM2008’s high-degree content would “over-cleanse” the data, potentially degrading the regional solution.

4.4 Digital Elevation Model (SRTM 1 Arc-second DEM)

The Shuttle Radar Topography Mission (SRTM) 1 arc-second DEM, offering approximately 30-meter spatial resolution, has emerged as a superior dataset for geoid and gravity modelling. Its fine resolution captures subtle topographic variations, such as small hills, ridges, and valleys, that are completely averaged out in coarser DEMs like those at 90-meter or 1-kilometer resolution. This capability is particularly important in rugged terrains, where gravity signals can change significantly over short distances due to abrupt elevation differences. A 30-meter DEM can preserve these sharp terrain gradients, making the resulting terrain corrections more accurate and reducing the risk of systematic errors in gravity anomalies. Coarser datasets tend to underestimate the gravitational influence of elevated features and overestimate that of depressions due to their inherent smoothing of terrain, leading to distorted anomaly fields and, ultimately, biased geoid surfaces.

In modern geoid determination, especially where centimetre-level accuracy is desired, such biases can result in errors of several centimetres in the geoid height, particularly in mountainous regions. For example, in areas like Colorado, the Andes, or the Himalayas, using a coarser 90-meter DEM may lead to geoid errors ranging from 2 to 5 centimetres or more. By contrast, the SRTM 1 arc-second data enables the accurate computation of terrain attraction integrals, better estimation of indirect topographic effects, and high-resolution modelling of gravity anomalies. These improvements directly translate to more accurate Stokes integration results and more reliable geoid surfaces. In empirical studies, high-resolution DEMs have consistently shown reduced root-mean-square (RMS) errors in geoid heights when compared to coarse-grid counterparts, validating the substantial impact of resolution on geodetic modelling outcomes.

Furthermore, the global availability and consistency of the SRTM 1 arc-second DEM add to its value. It offers seamless coverage between 60°N and 60°S and is uniformly referenced to the WGS84 geodetic datum. This uniformity eliminates the need to patch together multiple local DEMs of varying quality and datums, simplifying processing and reducing potential errors in geoid computations. Older global DEMs such as GLOBE (~1 km), GTOPO30 (~1 km), or ETOPO1 (~1.8 km) lack the spatial detail and accuracy needed for modern geodetic applications and introduce significant errors in rugged terrain. For instance, studies have shown that using ETOPO1 in mountainous regions like

Kazakhstan can result in standard deviations in geoid height differences exceeding 30 meters, making it unsuitable for precision geodesy. By contrast, SRTM 1 arc-second datasets deliver orders of magnitude improvement in both resolution and vertical fidelity.

Despite these advantages, many studies still rely on lower-resolution DEMs due to several practical constraints. High-resolution datasets are computationally demanding, requiring greater storage space and processing time. Historically, global 1 arc-second SRTM data were unavailable or restricted outside the U.S., which limited their adoption. Moreover, legacy workflows and software were often optimized for coarser inputs, making transition to finer grids resource-intensive. However, with the recent global availability of void-filled SRTM 1" data, these limitations have largely been overcome. For researchers aiming to achieve centimetre-level geoid accuracy, especially in rugged terrains, the use of high-resolution DEMs like SRTM 1" is now both feasible and necessary.

In geoid modelling practice, terrain corrections are typically performed within a specific radius around each computation point, often up to 20–50 km. Because the gravitational effect of terrain decays rapidly with distance, the terrain close to the computation point—referred to as the near-field—has the greatest influence on correction accuracy. It is precisely this near-field region where the difference between a high-resolution and low-resolution DEM is most pronounced. Coarse DEMs tend to average out sharp local variations, resulting in underestimation of terrain attraction from peaks and overestimation from depressions. This distortion is propagated into the terrain correction, affecting both the gravity anomalies and the geoid surface derived from them. High-resolution DEMs like the 30 m SRTM preserve these critical local features, enabling more accurate numerical integration of terrain mass effects and yielding better model fidelity.

Empirical results from various studies strongly support the superiority of high-resolution DEMs in geoid computation. In Malaysia, for example, researchers observed that using 90-meter SRTM data reduced the RMS vertical difference in geoid height to 2.17 meters, compared to 3.61 meters when using a much coarser 1-arcminute grid. This clearly shows that higher resolution correlates with lower height errors. Kiamehr and Sjöberg (2005) similarly demonstrated that replacing coarse DEMs with SRTM significantly improved gridded gravity anomalies, terrain corrections, and geoid heights in Iran. They found that inaccuracies introduced by using the GLOBE DEM instead of SRTM could reach ± 1.1

meters in geoid height and ± 160 mGals in surface gravity, illustrating the profound influence of DEM resolution on geoid accuracy.

The use of the 1 arc-second (30 m) SRTM DEM substantially enhances the accuracy and reliability of terrain corrections, gravity anomalies, and geoid models. Though it imposes a higher computational burden, the resolution gain yields better representation of local topography, minimizes systematic biases in terrain-attracted gravity corrections, and ensures higher-fidelity geoid surfaces. With the current availability of global high-resolution DEMs and advancements in computational tools, there is a strong case for adopting fine-resolution elevation data as the standard for regional geoid modelling, especially in geodetically challenging terrains. Such practices are essential for realizing centimetre-level vertical datums and supporting high-precision applications in geophysics, surveying, and Earth science.

4.5 Validation Data (Geoid Slope Validation Survey)

The Geoid Slope Validation Survey 2017 (GSVS17), conducted by the National Geodetic Survey (NGS), represents a pivotal effort in validating and enhancing the accuracy of gravity-based geoid models, particularly in challenging terrains. This survey, the third and final in the GSVS series, was executed along a 360-kilometer stretch of US Highway 160 in southern Colorado, spanning from Durango to Walsenburg. The region's rugged topography, with elevations ranging between 1,900 and 3,300 meters, provided an ideal testing ground for assessing geoid model performance under complex conditions.

A comprehensive suite of geodetic observations was collected at approximately 223 benchmarks spaced at 1.6-kilometer intervals. Each benchmark underwent long-duration GPS sessions exceeding 24 hours, ensuring high-precision ellipsoidal height measurements. Complementing these were first-order, Class II spirit levelling measurements, which provided orthometric heights with a precision of ± 0.7 mm per square root kilometre. Additionally, absolute gravity measurements were obtained using FG-5 gravimeters at key endpoints and A-10 gravimeters at all benchmarks, achieving accuracies better than ± 10 microgals. Vertical gravity gradients were also measured at each site, contributing to a robust dataset for geoid evaluation.

The primary objective of GSVS17 was to generate a high-fidelity "ground truth" dataset to assess the accuracy of various geoid models, including those developed under the Gravity for the Redefinition of the American Vertical Datum (GRAV-D) initiative. By

comparing geoid undulations derived from GPS and levelling data against model predictions, researchers aimed to quantify model discrepancies and identify areas for improvement. Notably, the inclusion of GRAV-D airborne gravity data in models like xGEOID19B was scrutinized to determine its impact on model accuracy. Findings indicated that while GRAV-D data contributed to model refinement, other factors such as terrain corrections and reference model choices also significantly influenced accuracy, often at the $\pm 1\text{--}2$ cm RMS level.

GSVS17's meticulous approach and comprehensive data collection have provided invaluable insights into geoid model performance in mountainous regions. The survey's outcomes have informed the development of more accurate gravimetric geoid models, which are crucial for establishing a reliable national vertical datum. By addressing the challenges posed by complex terrain and integrating diverse observational data, GSVS17 has set a benchmark for future geodetic surveys and model validations.

Chapter 5. Methodology

The goal of this study is to compute a high-resolution regional geoid using the classical Remove-Compute-Restore (RCR) approach. In this framework, gravity anomalies from global and regional sources are separated by wavelength and treated in a stepwise manner. First, raw gravity observations are corrected for known effects (e.g. height, terrain, atmospheric masses) to form standardized gravity anomalies. Simultaneously, the contribution of long-wavelength geopotential (from a high-degree global geopotential model, GGM) is removed. The residual (short-wavelength) anomalies are then used in a Stokes boundary-value integral (implemented via FFT) to compute a residual geoid. Brun's formula is applied to convert potentials to height-anomalies, and finally the global reference geoid undulation is restored to obtain the co-geoid model. Lastly, indirect topographic effect correction is added to get the geoid. Figure 5.1 illustrates the processing pipeline.

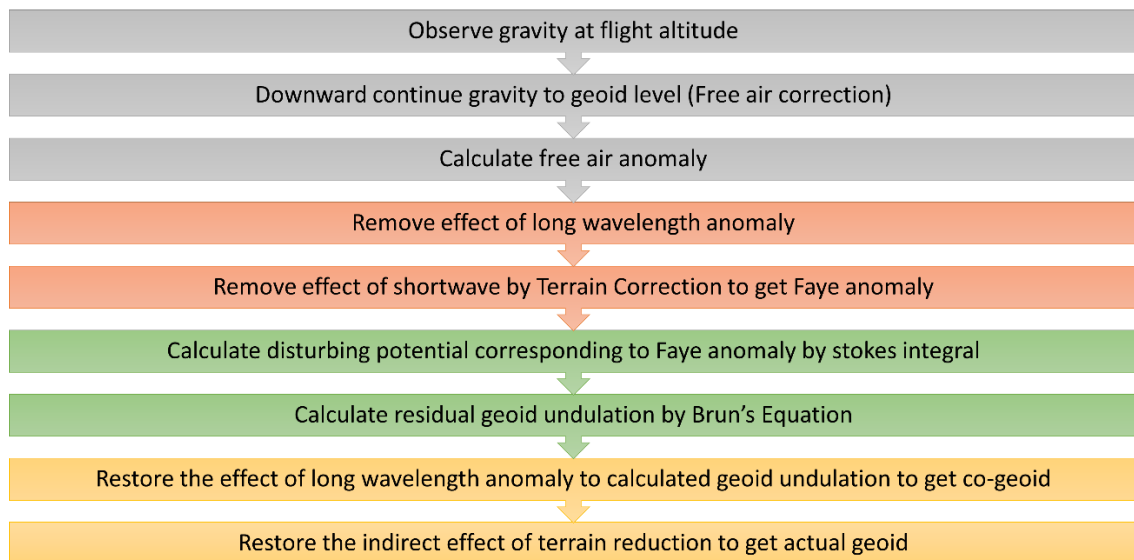


Figure 5.1. Schematic flowchart of the RCR geoid modelling pipeline

The following sections describe each step in detail, with justification and standard references. Equation numbers or symbols (when used) refer to classic geodetic theory (e.g. Heiskanen & Moritz, 1967; Hofmann-Wellenhof & Moritz, 2006) and gravity field manuals (e.g. the GRAV-D User Manual). Throughout, we adopt a WGS84 reference ellipsoid datum.

5.1 Input Data Requirements

The methodology requires a comprehensive set of geodetic and geophysical input datasets to support accurate gravity reduction and geoid modelling. The key inputs include:

- Observed gravity values (g_{obs}) at airborne flight altitudes from GRAV-D campaign point files
- Latitude (ϕ) and longitude (λ) coordinates of each observation point (in WGS-84 reference frame)
- Flight height above the ellipsoid (h_{flight})
- Geoid undulation values (N_{GGM}) from a Global Geoid Model
- Gravity anomalies (Δg_{GGM}) derived from the same Global Geoid Model
- Digital Elevation Model (DEM)-based surface heights (H_P)
- Orthometric heights from levelling benchmarks (e.g., GSVS17) for geoid validation

These datasets serve as the foundation for performing gravity reductions and anomaly computations that underpin the classical remove-restore method for regional geoid modelling.

5.2 Gravity Reductions and Anomaly Computation

The first stage is gravity data reduction, converting observed gravity to standard anomalies. This involves computing the theoretical normal gravity at each station (on the reference ellipsoid at that latitude) and removing it, as well as applying the free-air corrections. Formally, the free air gravity anomaly is defined as the observed gravity at the station, minus the free-air correction (accounting for the elevation of the station), minus the normal gravity on the ellipsoid. In practice, a second-order free-air correction (Taylor series expansion) is often used for accuracy. The result is the free-air anomaly which removes the bulk effect of station height.

See GRAV-D General User Manual, Section 3.3 for equations 5.1 and 5.2.

The free-air anomaly ($\Delta g_{\text{free-air}}$) is computed using the following relation:

$$\Delta g_{\text{free-air}} = g_{\text{obs}} + \text{FAC} - \gamma \quad (5.1)$$

Where:

- (g_{obs}) is the observed gravity at the flight altitude,

- (FAC) is the second-order free-air correction,
- (γ) is the normal gravity at the ellipsoid corresponding to the observation latitude.

The second-order free-air correction accounts for height-dependent variations and is formulated as:

$$\text{FAC} = - \left[\left(\frac{-2\gamma}{a} \right) (1 + f + m - 2f \sin^2 \phi) H + \left(\frac{3\gamma}{a^2} \right) H^2 \right] \quad (5.2)$$

where the orthometric height (H) is approximated by:

$$H = h_{\text{flight}} - N_{\text{GGM}} \quad (5.3)$$

The normal gravity (γ) is computed using the Somigliana–Pizzetti formula (Hofmann-Wellenhof and Moritz, 2006 (Eq. 2-146)):

$$\gamma = \frac{a\gamma_{\text{eq}} \cos^2 \phi + b\gamma_{\text{pole}} \sin^2 \phi}{\sqrt{a^2 \cos^2 \phi + b^2 \sin^2 \phi}} \quad (5.4)$$

Constants and parameters used in the above expressions:

- ($f = 1 / 298.257223563$): Flattening of the WGS-84 ellipsoid,
- ($a = 6378137$ m): Equatorial radius,
- ($b = 6356752.3142$ m): Polar radius,
- ($GM = 3.986004418 \times 10^{14}$ m 3 /s 2): Geocentric gravitational constant,
- ($\omega = 7.292115 \times 10^{-5}$ rad/s): Angular velocity of Earth,
- ($m = \frac{\omega^2 a^2 b}{GM}$): Centrifugal parameter,
- ($\gamma_{\text{eq}} = 978032.53359$ mGal): Normal gravity at the equator,
- ($\gamma_{\text{pole}} = 983218.49378$ mGal): Normal gravity at the poles.

5.3 Removal of Long-Wavelength Geopotential Signal

In the RCR approach, the next step is to remove long-wavelength (global) gravity field signals from the anomalies. A high-degree global geopotential model (GGM) contains the long-wavelength gravity variations (low spherical harmonics). We compute the gravity anomaly from this GGM at each grid point and subtract it from the observed anomalies. This ensures that only the shorter-scale residual anomalies remain for regional processing. In effect, the GGM acts as the remove field. By removing the GGM signal first, the subsequent Stokes-integral solution will honour the accuracy of the satellite-derived long

wavelengths, while the local (high-frequency) signal is handled separately. This step also avoids truncation artifacts: if the GGM is used up to degree 360 or more, the residual anomalies correspond to wavelengths below a few hundred kilometres, suitable for regional FFT processing.

The residual short- and medium-wavelength gravity anomaly is computed as:

$$\Delta g_{s \& mw} = \Delta g_{\text{free-air}} - \Delta g_{\text{GGM}} \quad (5.5)$$

Where:

- $(\Delta g_{\text{free-air}})$: Free-air gravity anomaly
- (Δg_{GGM}) : Gravity anomaly from the Global Geopotential Model,
- $(\Delta g_{s \& mw})$ Residual short-and medium-wavelength anomaly retained for regional analysis.

5.4 Atmospheric Correction

After removing the GGM, we apply an atmospheric correction to the gravity anomalies. The mass of the atmosphere above each station contributes a small additional gravity that must be removed to isolate the effect of the solid Earth. A standard atmospheric correction (Heiskanen & Moritz, 1967; Forsberg, 1984) treats the atmosphere as a layered mass with a known density profile. We compute and subtract this effect from the gravity anomaly. Although the atmospheric effect is modest compared to topography, it is important for formal consistency (and can contribute up to a few centimetres in geoid height over high altitudes). Modern gravimetric software and manuals (e.g. the GRAV-D Manual, Heiskanen & Moritz) include the standard atmospheric reduction.

We remove the effect of the atmosphere to obtain a gravity anomaly that retains medium-wavelength signals and is corrected for atmospheric effects. The atmospheric correction (ATMC), equation 5.6 was modelled using a fifth-degree polynomial approximation of atmospheric density variation with height, originally derived from the U.S. Standard Atmosphere (NOAA, NASA, and USAF, 1976) and cited in Abbak et al. (2024).

Standard atmospheric correction formula:

$$\begin{aligned} \text{ATMC} = & 0.871 - 1.0298 * 10^{-4}H + 5.3105 * 10^{-9}H^2 - 2.1642 * \\ & 10^{-13}H^3 + 9.5246 * 10^{-18}H^4 - 2.2411 * 10^{-22}H^5 \end{aligned} \quad (5.6)$$

Atmosphere-corrected gravity anomaly:

$$\Delta g_{s \& mw}^{\text{atm}} = \Delta g_{s \& mw} - \text{ATMC} \quad (5.7)$$

5.5 Terrain Corrections via FFT

The next step is to remove the effect of local topography from the gravity field. We compute the terrain correction (TC): the gravitational attraction of the actual terrain is calculated and removed from the anomaly. In a gridded setting, this is done by convolving the elevation grid with the Newtonian attraction kernel. We use a fast Fourier transform (FFT) method to compute the three-dimensional terrain effect (Forsberg, 1984; Hwang et al., 2002). In practice, the DEM is transformed into the frequency domain, multiplied by the theoretical terrain-kernel spectrum (Molodensky's kernel in the flat Earth approximation), and inverted. The result is the precise terrain correction on a grid, which is then subtracted from the anomaly. The NOAA-GRAVSOFT documentation and other sources explicitly mention that terrain corrections can be efficiently evaluated by FFT (or its variants). For example, GRAVSOFT's TCFOUR routine implements the FFT-based terrain convolution. This approach is accurate and faster than summing prisms.

This step isolates the signal due to anomalous subsurface density by accounting for all known topographic mass: the local topography has been “removed” from the gravity. It is important to use a sufficiently high-resolution DEM and to carefully handle edges (e.g. with padding) because the FFT convolution can otherwise introduce Gibbs oscillations near the grid boundaries. In practice we ensure that the terrain grid is large enough (often extended beyond the area of interest) to minimize edge effects.

According to Forsberg (1985, equation 10, p. 346), the terrain correction at a point (P) can be approximated by:

$$TC(P) = \frac{1}{2} G\rho \iint \frac{(h_Q - h_p)^2}{r^3} dx dy \quad (5.8)$$

Where:

- (G) is the gravitational constant,
- (ρ) is the average crustal density,
- (h_p) is the height at the evaluation point (from DEM),
- (h_Q) is the height at the surrounding grid points (from DEM)

- (r) is the distance from the evaluation point to each surrounding point, evaluated as $\sqrt{(X_P - X_Q)^2 + (Y_P - Y_Q)^2}$
- (dx) and (dy) are the DEM cell sizes.

This expression can be expanded as:

$$TC(P) = \frac{G\rho}{2} \left[\iint \frac{H_Q^2}{r^3} dx dy + H_P^2 \iint \frac{1}{r^3} dx dy - 2H_P \iint \frac{H_Q}{r^3} dx dy \right] \quad (5.9)$$

In FFT terms, the terrain correction can be written as:

$$TC(P) = \frac{G\rho}{2} \left[H_P^2 \cdot F^{-1} \left(F(1) \cdot F \left(\frac{1}{r^3} \right) \right) + F^{-1} \left(F(H_Q^2) \cdot F \left(\frac{1}{r^3} \right) \right) - 2H_P \cdot F^{-1} \left(F(H_Q) \cdot F \left(\frac{1}{r^3} \right) \right) \right] \quad (5.10)$$

Where (F) and (F^{-1}) denote the forward and inverse Fourier transforms, respectively. Equations (5.9) and (5.10) are derived from Forsberg (1985).

5.6 Computation of the Faye Anomaly

According to the NOAA-NCEI dictionary, “Helmert Anomalies, also known as Faye Anomalies, are free-air anomalies which have had a terrain correction applied” (National Centers for Environmental Information [NCEI], n.d.). This Faye anomaly is the principal input to the Stokes integral in the compute step: it contains both the medium wavelengths of the gravity field. Its use ensures that the Stokes integral computes the residual geoid.

The Faye anomaly is computed as:

$$\Delta g_{faye} = \Delta g_{s \& mw}^{atm} - TC \quad (5.11)$$

5.7 Stokes Integral via FFT

The disturbing potential is obtained by numerically solving Stokes’s integral formula on the Faye anomaly field. Stokes’s formula relates the disturbing potential TTT at a point

to an area integral of gravity anomalies over the Earth's surface. Instead of direct numerical integration, we use FFT-based convolution methods (Forsberg, 1984; Strang & van Hees, 1990). In practice, the spherical Stokes kernel is applied in the spectral domain, which is efficient for gridded data. NOAA's geoid-computation software notes that the Stokes integral "can conveniently be evaluated using FFT methods." We implement a band-limited Stokes solution (typically up to a chosen spherical cap angle) so that only the local residual field is integrated, while the remainder (beyond the cap) is approximated or treated as bias. The FFT approach implicitly performs a convolution of the Faye anomaly grid with Stokes's function. The result of this operation is a map of the residual disturbing potential. In essence, this is the gravimetric residual potential assuming the global field has been removed.

Because our anomalies are on a regular (latitude–longitude) grid of limited area, we implement a planar approximation to Stokes's formula with zero-padding and tapering to reduce edge effects. (Caution is needed: as noted above, FFT methods can introduce Gibbs oscillations if the anomaly field is not smoothly extended.) At this point, we have effectively solved the Stokes boundary-value problem in a spherical approximation for the residual field.

Hofmann-Wellenhof and Moritz (2006) present the classical form of the Stokes kernel along with its integral formulation. The disturbing potential (T_r) using Stokes's integral for the residual field Δg_{faye} is given by:

$$T_r = \frac{R}{4\pi} \iint \Delta g_{faye} S(\psi) d\Omega \quad (5.12)$$

Where R is the mean earth radius, Ω is the sphere of integration, ψ is the geocentric angle between computation and running points. It is computed as a function of the spherical coordinates (ϕ_P, λ_P) of the computation point P and the coordinates (ϕ_Q, λ_Q) of the data points.

$$\begin{aligned} \sin^2 \frac{\psi}{2} = & \sin^2 \left(\frac{\phi_P - \phi_Q}{2} \right) \\ & + \sin^2 \left(\frac{\lambda_P - \lambda_Q}{2} \right) \times \cos \phi_P \times \cos \phi_Q \end{aligned} \quad (5.13)$$

Equation 5.13 is the classic haversine identity used to compute the great-circle distance between two points P and Q on a sphere. The central angle between two points on a sphere can be computed using the haversine formula (Sinnott, 1984).

$S(\psi)$ is the Stokes kernel; the integration is over the entire sphere. The integral can be done on a planar cartesian grid for our regional case.

$$S(\psi) = \frac{1}{\sin \frac{\psi}{2}} - 6 \sin \frac{\psi}{2} + 1 - 5 \cos \psi - 3 \cos \psi \ln \left(\sin \frac{\psi}{2} + \sin^2 \frac{\psi}{2} \right) \quad (5.14)$$

Stokes Integral by FFT

$$T_r = \frac{R}{4\pi} \left[F^{-1} \left(F(\Delta g_{faye}) F(S(\psi)) \right) \right] \quad (5.15)$$

5.8 Brun's Formula and Conversion to Geoid Undulation

To convert the computed disturbing potential into a physical height, we apply Brun's formula. Brun's formula states that the geoid undulation N is given by the disturbing potential divided by the normal gravity at the computation point. In practice, we compute normal gravity (γ) at the reference ellipsoid to use in this conversion. After this step, the grid contains the residual geoid undulation above the reference ellipsoid, based solely on the observed residual gravity field. The fundamental geodetic formula originates from Bruns (1878) and is reiterated in the context of physical geodesy by Hofmann-Wellenhof & Moritz (2006).

Thus, residual geoid, (N_r) by Brun's equation

$$N_r = \frac{T_r}{\gamma} \quad (5.16)$$

5.9 Restoration of the Global Geoid

Having computed the residual geoid, we now restore the removed long-wavelength geoid undulations from the GGM. This is the final “restore” phase of RCR. We take the geoid heights from the same global model that was subtracted earlier, and add these back residual geoids is the co-geoid height. In other words, the co-geoid undulation is the superposition of the low-degree GGM geoid and the high-degree residual geoid. This ensures that the final model honours the long-wavelength accuracy of the satellite model while incorporating the detailed local gravity data. At this stage we have the gravimetric co-geoid that can be compared to independent data (e.g. GNSS-levelling) if desired.

$$N_{\text{Co-Geoid}} = N_r + N_{\text{GGM}} \quad (5.17)$$

5.10 Indirect Topographic Effect

In a Stokes–Helmert or remove-compute-restore (RCR) scheme, one first removes the gravitational potential of terrain (and other long-wavelength signals such as a global geopotential model) from the observations, computes a residual “co-geoid,” and then adds back the contributions of the removed masses. The indirect effect is precisely the change in the geoid due to putting the topographic masses back. In Helmert’s second condensation method, all topographic mass is condensed onto a spherical reference surface and the geoid is computed for this “reduced” Earth. Restoring the original relief then shifts the geoid surface; this shift is the indirect effect. In practice one often applies an indirect correction on the order of tenths of meters in mountainous areas.

Planar formulas (e.g. Nagy’s or Wichiencharoen’s) assume a flat reference surface and constant density, leading to simple convolution integrals of the DEM. However, both Martinec and Vaníček (1994) and Sjöberg (1999) have shown that this planar model is inadequate in high relief: a flat-Earth approximation systematically biases the indirect effect by up to tens of centimetres in high mountains. Adopting a spherical treatment of the geoid surface yields more accurate expressions. In particular, Sjöberg and Nahavandchi (1999) conclude that a classical planar integral truncated at a finite cap omits long-wavelength geoid contributions on the order of 0.5 m in high mountains, and recommend supplementing the planar convolution with a spherical-harmonic representation of the terrain. Similarly, Molodensky’s approach (which treats observations on the Earth’s actual surface) inherently includes terrain effects but is computationally demanding. In summary, the indirect effect is conceptually the change in geoid height caused by the mass of the topography, and it must be added to the co-geoid to obtain the final regional geoid.

Following the formulation by Wang and Rapp (1990), as presented in Eq. (60) of Jekeli and Serpas (2003), the indirect topographic effect was computed using the second-order flat-Earth approximation. Thus, indirect topographic effect ($N_{in-direct}$), can be expressed as:

$$N_{in-direct}(P) = \frac{-G\rho}{\gamma} \left[\pi H_P^2 + \frac{1}{6} \iint_{\Omega} \frac{H_Q^3 - H_P^3}{r^3} d\Omega \right] \quad (5.18)$$

Where:

- G is the universal gravitational constant,
- ρ is the mean crustal density,
- γ is the normal gravity at point P,
- H_P is the DEM height at the computation point P,
- H_Q is the DEM height at the surrounding points Q,
- r is the planar distance between P and Q,
- Ω denotes the region of integration, and
- $d\Omega \approx dx \cdot dy$ is the surface area element in a planar approximation.

The first term πH_P^2 represents a local (self-effect) contribution, while the second integral term accounts for the potential difference induced by all other terrain masses surrounding point P. This formula is based on a planar approximation suitable for regional studies where the curvature of the Earth is neglected within the computational cap.

For computational efficiency, especially with gridded topography data, the above integral can be evaluated using the Fast Fourier Transform (FFT). The FFT method converts the convolution integral into a product in the spectral domain, allowing for rapid computation.

The FFT-based form is written as:

$$N_{in-direct} = \frac{-G\rho}{\gamma} \left[\pi H_P^2 + \frac{1}{6} \left[F^{-1} \left(F(H_Q^3)F\left(\frac{1}{r^3}\right) \right) - H_P^3 \cdot F^{-1} \left(F(1)F\left(\frac{1}{r^3}\right) \right) \right] \right] \quad (5.19)$$

5.11 Final Geoid Computation

Once the indirect effect has been computed, it is added to the co-geoid to yield the final geoid undulation:

$$N_{Geoid} = N_{Co-Geoid} + N_{in-direct} \quad (5.20)$$

This step completes the Remove-Compute-Restore (RCR) process by including topographic mass. It ensures a more physically consistent and accurate geoid model.

Thus, RCR method is widely used in regional geoid projects because it naturally combines global models with dense local data. It is particularly effective when the study area is relatively small (so that a spherical cap integration suffices) and when a reliable global model is available to supply long waves. In this context (regional geoid modelling), RCR provides a practical pipeline. All steps above (reductions, FFT, Stokes, Brun) are grounded in classical geodesy (Heiskanen & Moritz, 1967; Forsberg, 1984) and have proven accuracy.

Chapter 6. Results and Discussions

6.1 Observed gravity data visualisation and analysis

The raw gravity dataset used in this study was obtained from the GRAV-D project's NGS Block MS02, Beta 2 version. This version contains a total of 2,460,617 point gravity observations, acquired using the Micro-g LaCoste TAGS S-211 airborne gravimeter. As per the GRAV-D User Manual (Youngman & Johnson, 2017), the TAGS system records gravity at a sampling rate of 20 Hz, corresponding to approximately one observation every 6.43 meters along the flight path, assuming a nominal cruise speed of 125 m/s. While this high temporal (and thus spatial) resolution is beneficial for capturing fine-scale aircraft motion during preprocessing, it significantly oversamples the gravity signal needed for regional geoid modelling, where the target wavelengths are much larger (typically >5 km). To optimize data volume and computational efficiency, the observations were down sampled by retaining every 10th value, resulting in an effective sampling frequency of 2 Hz (i.e., one point every \sim 64.3 meters). This down sampling preserves the signal content relevant to medium- and long-wavelength gravity features, while substantially reducing redundancy and processing time. The choice to use the Beta 2 version reflects the desire to work with the most recent and updated release available for Block MS02. Figure 6.1 presents a scatter plot of the sampled gravity observations, providing a visual overview of the spatial distribution and magnitude of gravity across the survey area.

It is important to note that the GRAV-D data product, as delivered, has already undergone all necessary preprocessing steps according to the GRAV-D Airborne Gravity Data User Manual. These include synchronization of GPS and gravity time tags, filtering, Eötvös correction, drift correction, levelling, and quality control procedures such as cross-line comparisons and reflight verification where needed. As such, the provided data represent fully corrected gravity values at flight altitude and are directly usable for geoid modelling without requiring further low-level processing. This is explicitly stated in the user manual for the corresponding block (Youngman & Johnson, 2017) and reflects the high degree of rigor in GRAV-D's field protocols and data processing pipelines.

The descriptive statistical analysis of the sampled airborne gravity data reveals key insights into the distribution and variability of gravity values within the study region. The mean gravity value is approximately 978247.79 mGal, while the median is slightly higher at 978270.06 mGal, indicating a slight asymmetry in the distribution. The standard deviation is 138.38 mGal, suggesting a moderate level of variability around the mean. The gravity values range from a minimum of 977574.61 mGal to a maximum of 978515.36 mGal, resulting in a total range of 940.75 mGal.

Further examination of the distributional characteristics reveals a pronounced negative skewness of -2.59, indicating that the data is left-skewed with a longer tail toward lower gravity values. This asymmetry implies the presence of a small number of significantly low gravity measurements, which may correspond to localized geophysical anomalies. The kurtosis value of 8.07 confirms a leptokurtic distribution, characterized by a sharp peak and heavy tails. This suggests a higher likelihood of extreme values compared to a normal distribution, reinforcing the influence of outliers or spatial heterogeneities in the gravity field. Overall, these statistics highlight the non-Gaussian nature of the dataset and underscore the importance of considering distributional properties in subsequent modelling and interpretation efforts.

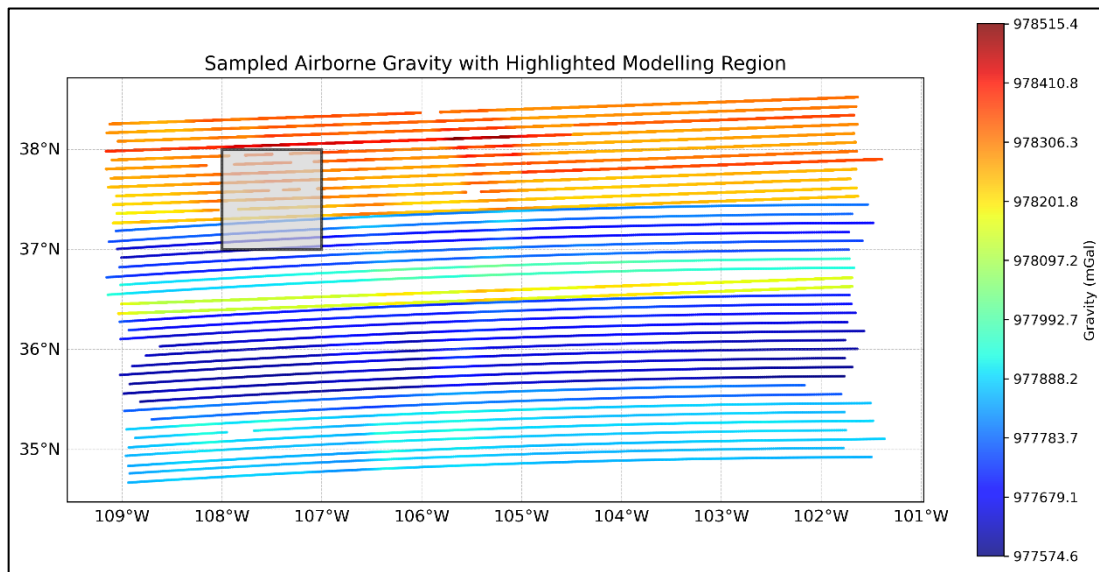


Figure 6.1: Scatter plot of the gravity observations with modelling region highlighted in grey

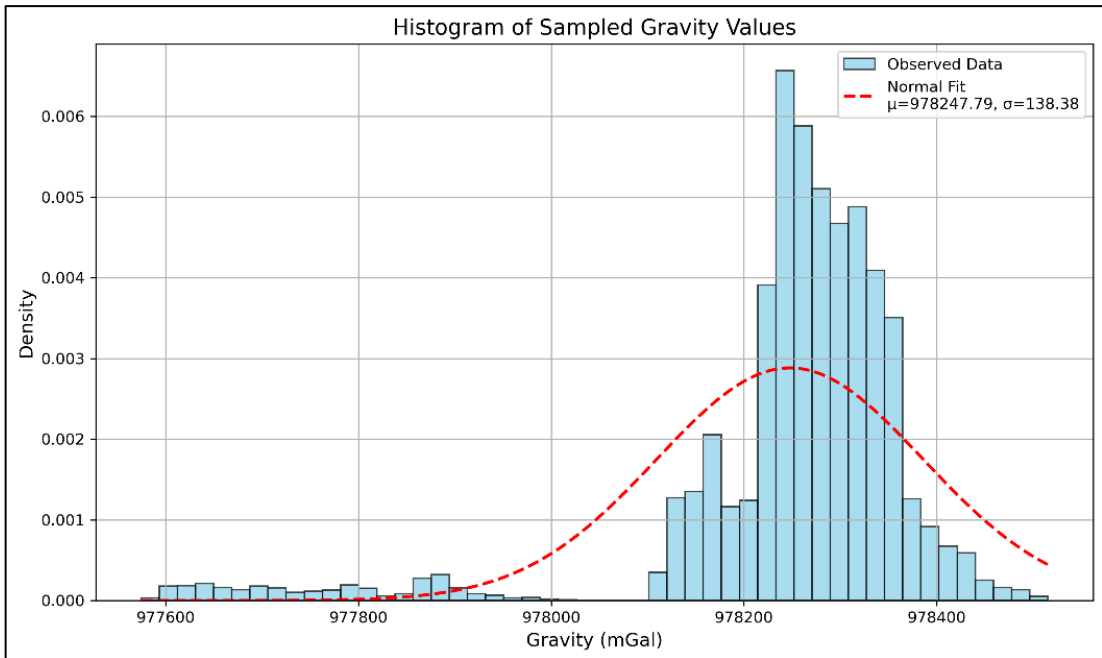


Figure 6.2 Histogram of airborne gravity data

Figure 6.2 displays a clearly left-skewed (negatively skewed) distribution, consistent with the earlier computed skewness value of approximately -2.59. A prominent peak is visible around 978250 mGal, aligning closely with the mean (978247.79 mGal) and median (978270.06 mGal), indicating that most gravity measurements are concentrated in this narrow range. However, the extended left tail signifies the presence of a relatively small number of significantly lower gravity values, likely associated with topographic depressions, structural anomalies, or local mass deficits.

The y-axis of the histogram represents probability density, expressed in units of [1/mGal], owing to the use of density=True in the histogram function. This normalization ensures that the area under the histogram sums to 1, effectively transforming the histogram into an empirical estimate of the probability density function (PDF) of the gravity distribution. Formally, the density in each bin is computed as the relative frequency of observations divided by the bin width in milligals. For example, a density value of 0.002 at 978200 mGal implies that the probability of observing a gravity value within a 1 mGal interval around that point is approximately 0.002, or 0.2%.

The overlaid red dashed curve represents a Gaussian distribution fitted using the sample mean and standard deviation. While the right-hand side of the histogram roughly follows the Gaussian curve, the left-hand side deviates considerably, with a heavier tail and

additional minor peaks, suggesting departure from normality. This is further supported by the high kurtosis (≈ 8.07), indicating a leptokurtic distribution with a sharp central peak and heavy tails, implying the presence of outliers or extreme values.

Thus the histogram illustrates a non-Gaussian, asymmetric distribution of gravity values, which may arise from complex subsurface structures or regional geophysical variations. These characteristics warrant careful consideration in further statistical modelling or geophysical inversion processes, as standard assumptions of normality may not hold.

The Pearson correlation analysis between the observed gravity data and flight altitude reveals a strong negative correlation, with a correlation coefficient of $r = -0.8920$ and a p-value approaching zero. This suggests a significant inverse relationship between altitude and gravity across the sampled airborne gravity dataset. Such a result typically implies that as the flight altitude increases, gravity measurements tend to decrease in a consistent and predictable manner, which is a common feature observed in airborne gravity surveys due to the influence of altitude on gravitational readings.

However, this negative correlation is expected in the context of gravity data observed at flight altitudes, prior to the application of necessary corrections such as the free-air correction or atmospheric adjustments. It is crucial to note that this correlation does not necessarily indicate erroneous data but rather reflects the inherent altitude-dependent characteristics of the measurements taken during flight. Gravity readings at high altitudes are subject to systematic biases that arise from the Earth's gravity field and the varying distance from the Earth's center at different altitudes. These biases are typically corrected for using the free-air correction, which compensates for the decrease in gravitational acceleration with increasing height above the Earth's surface, as well as atmospheric corrections, which account for air density and pressure variations at altitude.

The relevance of this Pearson correlation test lies in its ability to highlight the presence of systematic bias that can arise from uncorrected altitude effects. By examining the relationship between altitude and gravity before applying corrections, we can confirm that such a bias exists in the dataset and requires attention. A significant negative correlation such as this is often an indication of incomplete or inadequate correction processes in airborne gravity data, which could lead to inaccurate geophysical interpretations if not addressed.

While the primary objective at this stage is to identify such correlations, the comprehensive corrections—including free-air and atmospheric corrections—will be implemented in subsequent stages of data processing. These corrections will aim to neutralize the altitude-gravity relationship, ensuring that gravity values become independent of flight altitude and more accurately reflect the Earth's gravitational field. Once these corrections are applied, the gravity data will be ready for more advanced geophysical analyses and geoid modelling, free from altitude-related artifacts.

Figure 6.3 presents a histogram of the flight altitudes used during the survey. The distribution is distinctly multimodal, with a dominant peak centered around ~5550 m, representing the standard cruising altitude for the majority of the survey. Several smaller peaks at higher altitudes indicate a subset of data collected in mountainous or rugged regions. While the primary mode reflects consistent flight height essential for minimizing altitude-induced errors in gravity measurements, the presence of outliers and minor peaks confirms the need for thorough correction procedures (e.g., free-air and terrain corrections). The histogram aids in assessing the consistency of data acquisition and in identifying segments where the application of altitude-dependent corrections may require additional scrutiny.

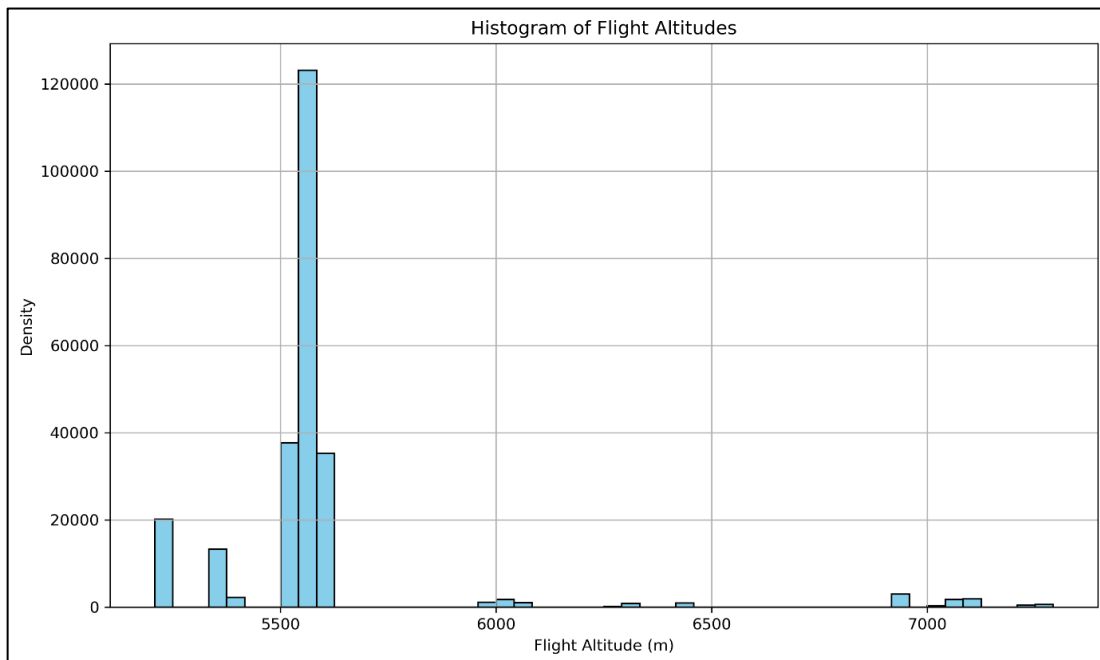


Figure 6.3 Histogram of flight altitudes

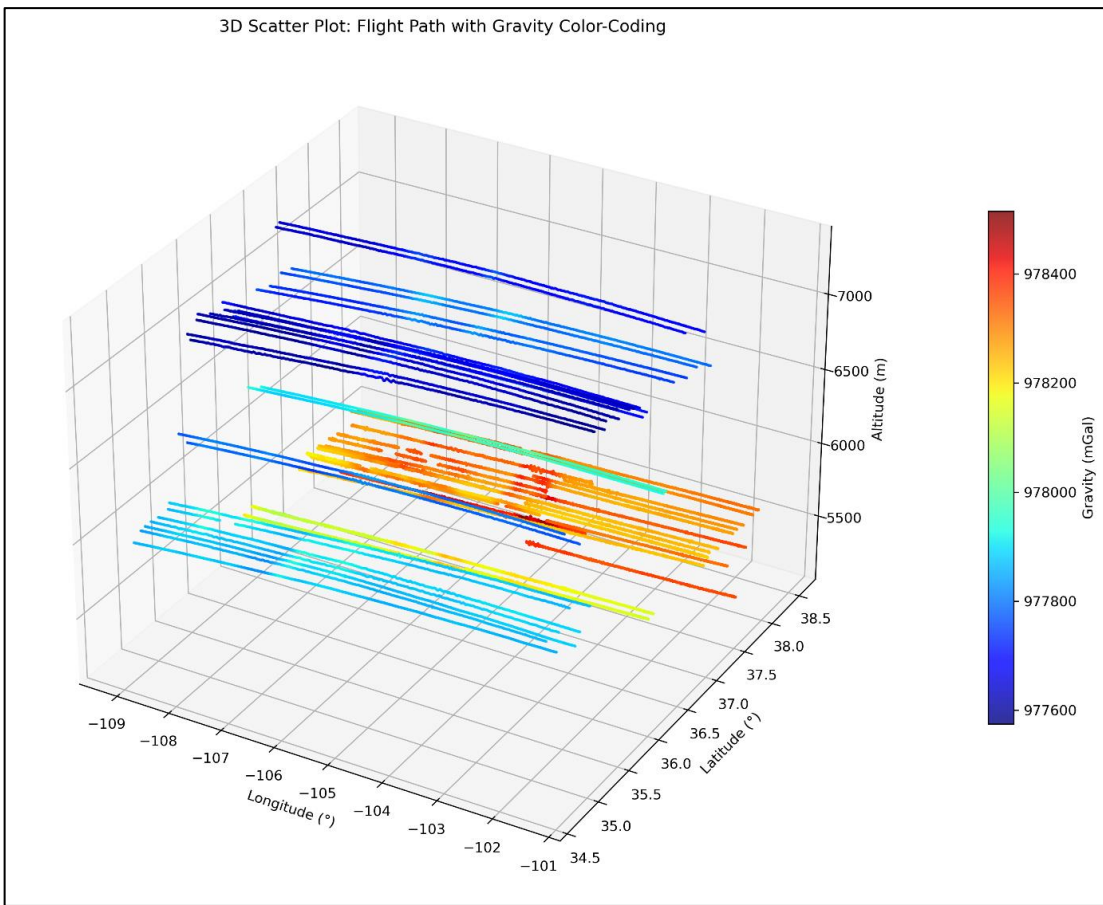


Figure 6.4 3D Scatter plot of observed gravity

Figure 6.4 illustrates the spatial configuration of the airborne gravity dataset using a 3D scatter plot, with flight altitude plotted against geographic coordinates (latitude and longitude), and gravity values represented through colour coding. This visualization offers a comprehensive depiction of the flight pattern, including both the vertical and horizontal variation in data acquisition. The majority of flight tracks are relatively straight and parallel, reflecting systematic airborne survey planning. However, variations in flight altitude are evident, particularly in areas of complex terrain, where topographic constraints necessitated adjustments in flight height. The color-coded gravity values also show regional variability, with lower gravity values (in cooler colours) generally associated with higher altitudes—an observation consistent with the earlier identified negative correlation between gravity and altitude ($r = -0.892$). This figure is especially useful in visually confirming that data coverage is continuous and that flight height adjustments may correspond with topographic influences or operational constraints during data collection.

It is also noted that while the GRAV-D campaign incorporates both data lines (flown at 10 km spacing) and cross lines (at 80 km spacing) for quality control, only the data lines are retained in this analysis. Cross lines, as per the GRAV-D methodology, are primarily used in internal calibration steps such as crossover difference analysis, and their exclusion here is consistent with standard practice in post-processed geoid modelling workflows.

Although the original GRAV-D dataset covers the full block, the regional geoid modelling in this study is confined to a $1^\circ \times 1^\circ$ area bounded by latitudes 37°N to 38°N and longitudes 107°W to 108°W. This region was chosen to coincide with the GSVS17 high-precision GNSS/levelling validation corridor. Importantly, point-wise gravity corrections (free-air, normal gravity, GGM removal, and atmospheric corrections) were performed on all raw observations prior to any spatial interpolation. Interpolation was applied only after obtaining gravity anomalies that reflect the medium and short-wavelength signal content and are corrected for atmospheric mass effects. This approach is justified because raw observed gravity is a composite of elevation-dependent, regional, and local effects, and it can vary abruptly due to topography and subsurface density changes. As such, interpolating raw gravity would be physically meaningless, as it assumes a spatial continuity that does not exist in the original measurements. In contrast, gravity anomalies—particularly those corrected for known systematic effects—vary more smoothly and predictably over space. Their behaviour is governed by potential theory and Laplace's equation, making them amenable to interpolation and gridding prior to integration in geoid modelling. This justification aligns with standard geodetic practices outlined in classical texts (Heiskanen & Moritz, 1967) and adopted in modern geoid modelling workflows (e.g., Forsberg, 1984; Hwang et al., 2002).

6.2 GGM-Derived Geoid Heights and Gravity Anomalies

To complement the analysis of observed airborne gravity data, additional gravity field functionals—specifically, the geoid and gravity anomaly values—were computed using the ICGEM Calculation Service (Ince et al., 2019). These functionals are derived from a global gravity model (GGM), selected based on its spatial resolution and degree of fit to the region of interest, and provide essential reference surfaces for interpreting gravity-related quantities.

Figures 6.5 and 6.6 depict the spatial variation of the GGM-based geoid height and the gravity anomaly, respectively, across the survey region. These visualizations serve as

reference layers for validating the consistency of observed gravity values and for further interpretation in geoid modelling

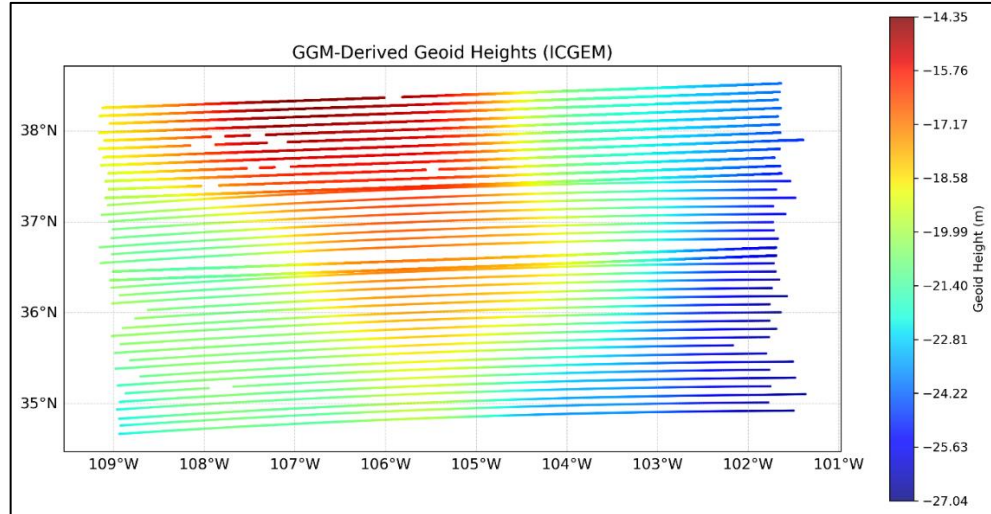


Figure 6.5 GGM derived geoid heights

The geoid, as defined by ICGEM, is the particular equipotential surface of the Earth's gravity field that corresponds to the undisturbed mean sea level and its continuation beneath the continents. Operationally, it is approximated using the height anomaly on the ellipsoid, with a correction term for topography derived using the Bouguer plate approximation. The topographic information utilized in this correction is based on the global ETOPO1 dataset. The resulting GGM-derived geoid height, referenced to the ellipsoid, captures large-scale variations in mass distribution and gravitational potential.

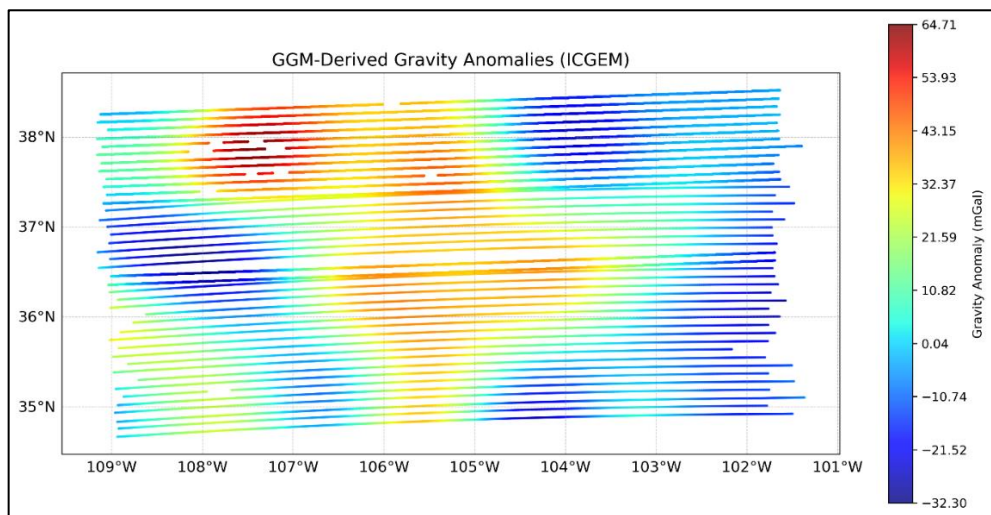


Figure 6.6 GGM derived gravity anomalies

The gravity anomaly plotted here follows the modern definition based on Molodensky's theory. It represents the difference between the actual gravity (computed from the full potential gradient) and the normal gravity evaluated on the telluroid—i.e., the theoretical reference surface shifted by the height anomaly. This formulation avoids the need for downward continuation and is more suitable for surface or airborne data comparisons.

6.3 Normal Gravity

Normal gravity represents the theoretical gravitational acceleration calculated at a given latitude and height on a reference ellipsoid, typically GRS80 or WGS84. It serves as the baseline model against which observed gravity is compared in anomaly computations. The spatial variation of normal gravity is primarily governed by Earth's oblateness and rotational flattening, resulting in a systematic increase from equator to poles.

The plotted distribution of normal gravity values as in figure 6.7 shows a smooth latitudinal gradient, as expected from ellipsoidal theory.

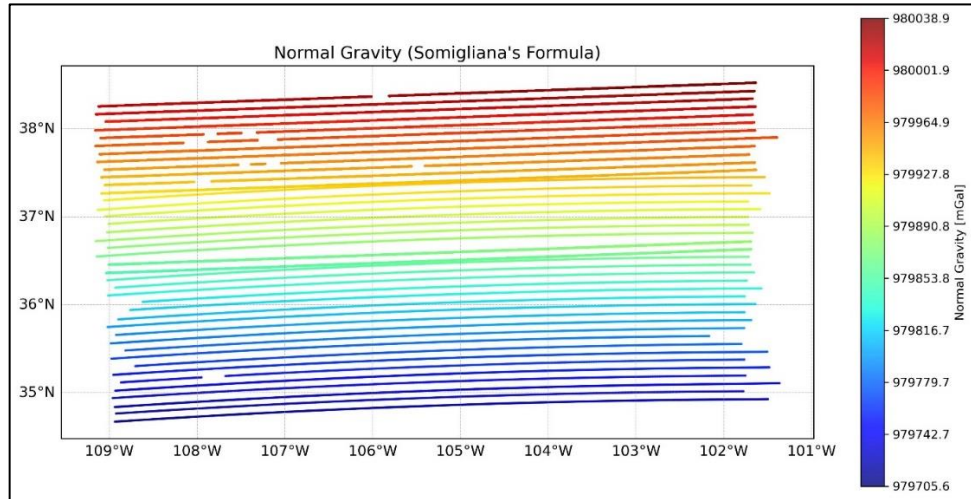


Figure 6.7 Normal gravity

6.4 Second-Order Free-Air Correction

The second-order free-air correction accounts for the reduction in gravitational acceleration with increasing altitude above the ellipsoid. Unlike its first-order counterpart, it incorporates curvature and gravity gradient variations using a Taylor series expansion, yielding greater accuracy, particularly at high altitudes.

The correction is dependent on the altitude as evident from the theoretical formula. This validates the initial observation of a strong negative correlation between raw gravity and flight height, and reinforces the necessity of altitude corrections in airborne gravity processing. The application of this correction serves to partially remove the systematic height dependence from the gravity data.

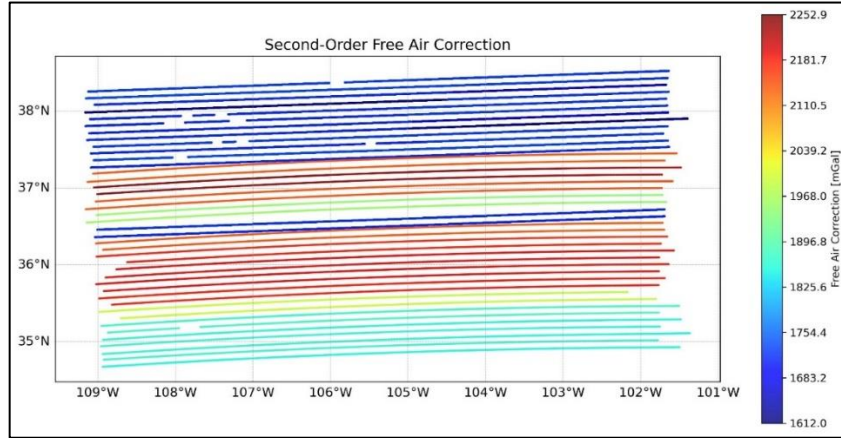


Figure 6.8 Second order free air correction

6.5 Free-Air Anomaly

The free-air anomaly (FAA) is derived by subtracting both the normal gravity and the free-air correction from the observed gravity. It captures the influence of subsurface mass variations, topography, and any residual altitude effects not fully compensated by the free-air correction.

Spatial analysis of the FAA plot reveals regions with pronounced positive or negative anomalies.

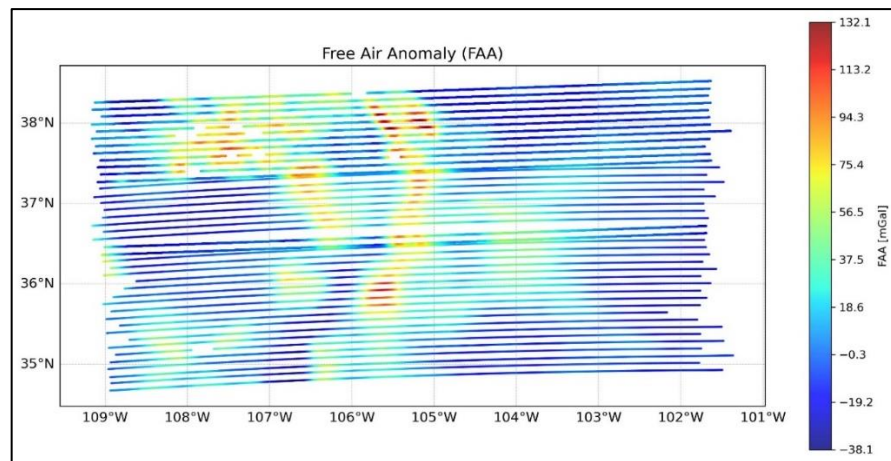


Figure 6.9 Free air anomaly

6.6 Short and Medium Wavelength Gravity Anomaly

To isolate the geophysical relevant signal content, long-wavelength gravitational effects—typically associated with the Earth’s global structure—are removed using a satellite-derived global gravity model (GGM05G). The resulting residual anomaly retains regional and local signal content with spatial scales between approximately 5 km and 100 km.

The smoother, band-limited nature of the field satisfies the assumptions of potential theory (e.g., Laplace’s equation), making it suitable for interpolation and gridding as part of the geoid modelling workflow.

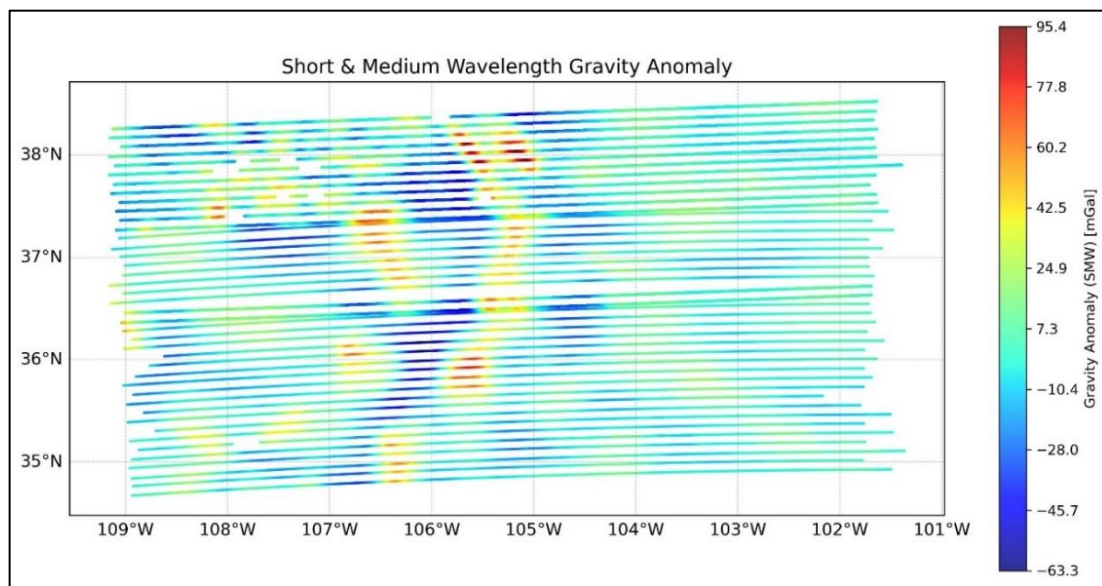


Figure 6.10 Short and medium wavelength gravity anomaly

6.7 Atmospheric Correction

Atmospheric correction accounts for the gravitational attraction of the air column above each observation point. This is typically modelled using a standard atmosphere approximation, and the correction is particularly relevant for airborne data collected at altitudes exceeding several kilometres.

The plot of atmospheric correction values exhibits a consistent positive trend with altitude, with corrections reaching approximately 0.9 mGal at the typical GRAV-D flight level (~ 6 km). Though modest in magnitude, the correction ensures consistency across all survey lines and further removes altitude-induced artifacts, thereby improving the fidelity of the gravity anomaly field.

6.8 Gravity Anomaly Corrected for Atmosphere

The final corrected anomaly is obtained by adding the atmospheric correction to the previously derived short- and medium-wavelength anomaly. This composite field represents a gravity anomaly free from both long-wavelength global trends and systematic altitude effects.

The plot of this final corrected field demonstrates a marked improvement in statistical properties. Specifically, correlation analysis reveals a negligible Pearson correlation coefficient with altitude ($r = -0.0234$), in contrast to the strong negative correlation observed in the raw gravity data ($r = -0.8920$). This confirms that the combined correction pipeline has effectively removed the height-dependent bias, yielding a gravity field that is representative solely of regional mass distributions. Such a result justifies the subsequent use of the corrected anomaly for spatial interpolation and integration within a remove–compute–restore (RCR) geoid modelling framework.

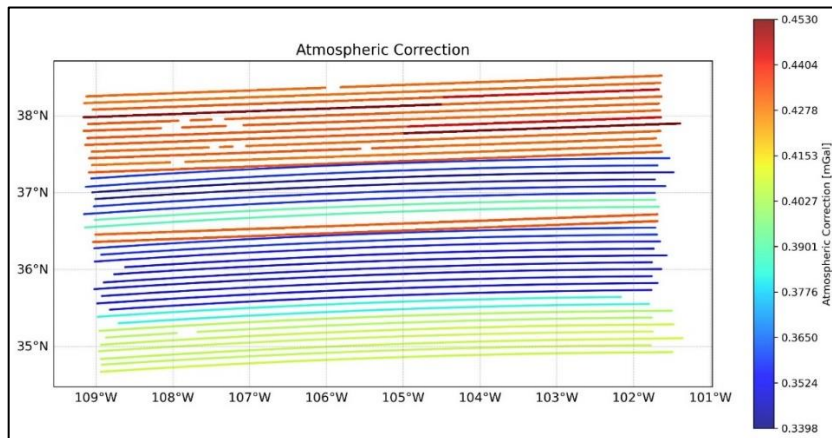


Figure 6.11 Atmospheric correction

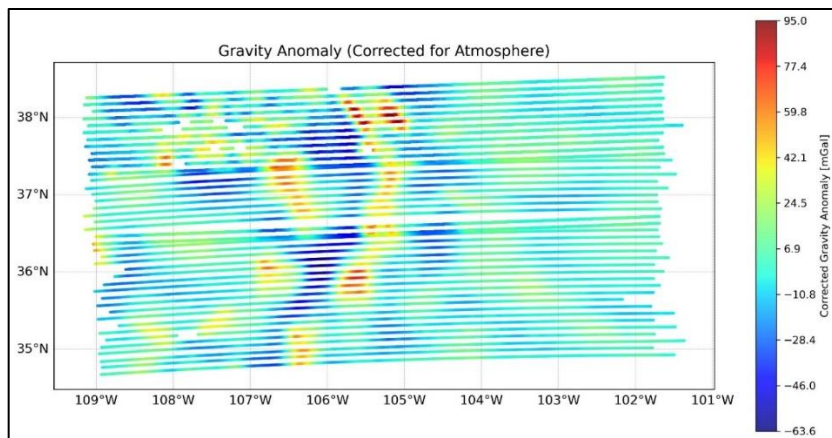


Figure 6.12 Gravity anomaly corrected for atmosphere

6.9 Analysis of Gravity Anomaly and Topography in the Modelling Region

Figure 6.13 presents the interpolated short and medium wavelength gravity anomaly field, corrected for atmospheric effects, overlaid with the original airborne gravity observation points within the selected $1^\circ \times 1^\circ$ modelling region ($37^\circ\text{--}38^\circ\text{N}$, $108^\circ\text{--}107^\circ\text{W}$). The corrected anomalies—derived through the removal of normal gravity, application of second-order free-air and atmospheric corrections, and filtering of long-wavelength signals—were interpolated using a linear interpolation scheme to produce a continuous anomaly surface suitable for geoid modelling. The interpolated gravity anomaly map reveals a well-defined pattern of geophysical anomalies ranging from approximately -42 mGal to $+48$ mGal. Positive anomalies are concentrated in the central and northeastern parts of the region, while pronounced negative anomalies dominate the southern and southwestern sectors.

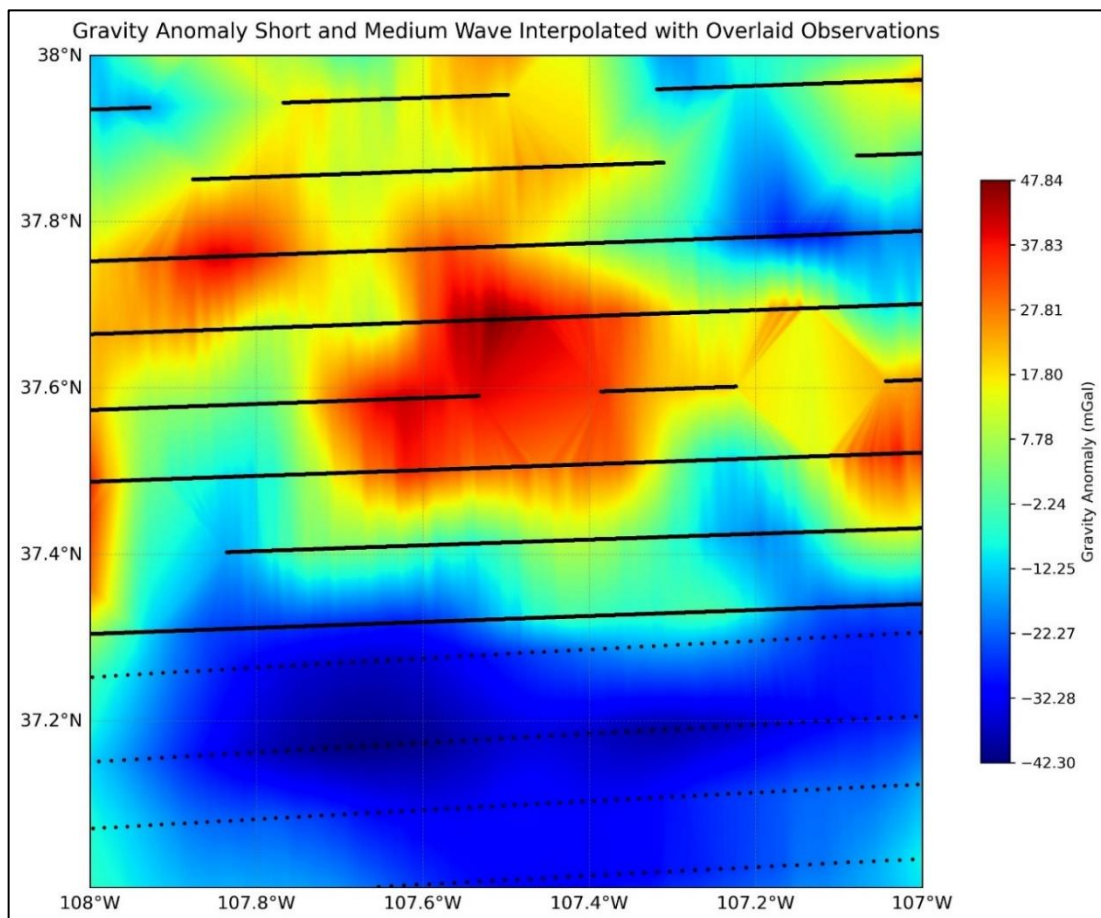


Figure 6.13 Interpolated plot of gravity anomaly overlaid with observation points

The observation points, representing the airborne gravity measurements, are densely distributed along flight lines with consistent spacing, providing sufficient sampling coverage to resolve regional and local gravity variations. The spatial density of these observations generally supports interpolation of features on the order of 5–10 km, corresponding to the short- and medium-wavelength components of the anomaly field. The corrected gravity anomaly, being a smoothed and harmonic potential field, is theoretically well-suited for interpolation using linear or higher-order methods. The strong visual agreement between the overlaid observations and the interpolated surface supports the adequacy of the linear interpolation approach in most areas.

However, some tessellation patterns and artificial angular boundaries are visible in parts of the interpolated field, particularly where flight line coverage is sparse or discontinuous. These artifacts are likely due to local data gaps or irregular sampling geometry, where linear interpolation across wider voids results in sharp gradients or unrealistic transitions. While these effects do not significantly compromise the regional integrity of the anomaly field, they highlight the importance of ensuring uniform spatial coverage—especially in critical modelling areas—to minimize interpolation artifacts. Nonetheless, the overall interpolated field exhibits smooth and geologically plausible trends, justifying its use for subsequent terrain correction and Stokes-based geoid computations.

Figure 6.14 presents the corresponding DEM, which illustrates significant elevation variation across the region, ranging from approximately 1800 m in the southern lowlands to over 4300 m in the rugged northern highlands.

Airborne gravity measurements over mountainous terrain can carry strong signals from near-surface topography. Even at high flight altitudes, the mass of valleys and peaks produces measurable gravity anomalies. In the 37–38°N, 107–108°W region (southwestern Colorado), rugged terrain (thousands of meters high) imparts significant short-wavelength signals on the free-air gravity anomaly that must be removed to recover a smoothly varying field for geoid computation. For example, Drenth et al. (2013) note that airborne gravity-gradient data “measure derivatives of the gravity field,” so “effects of terrain and near-surface geology are amplified” in the data, making “proper terrain corrections … critically important”. Likewise, Lin et al. (2025) show that uncorrected gravity-model errors grow with terrain altitude and that applying a detailed terrain (Residual Terrain Model, RTM) correction significantly reduces anomalies in

mountainous areas. In short, even high-altitude surveys over mountains require terrain correction to remove local mass effects and yield a harmonic anomaly field.

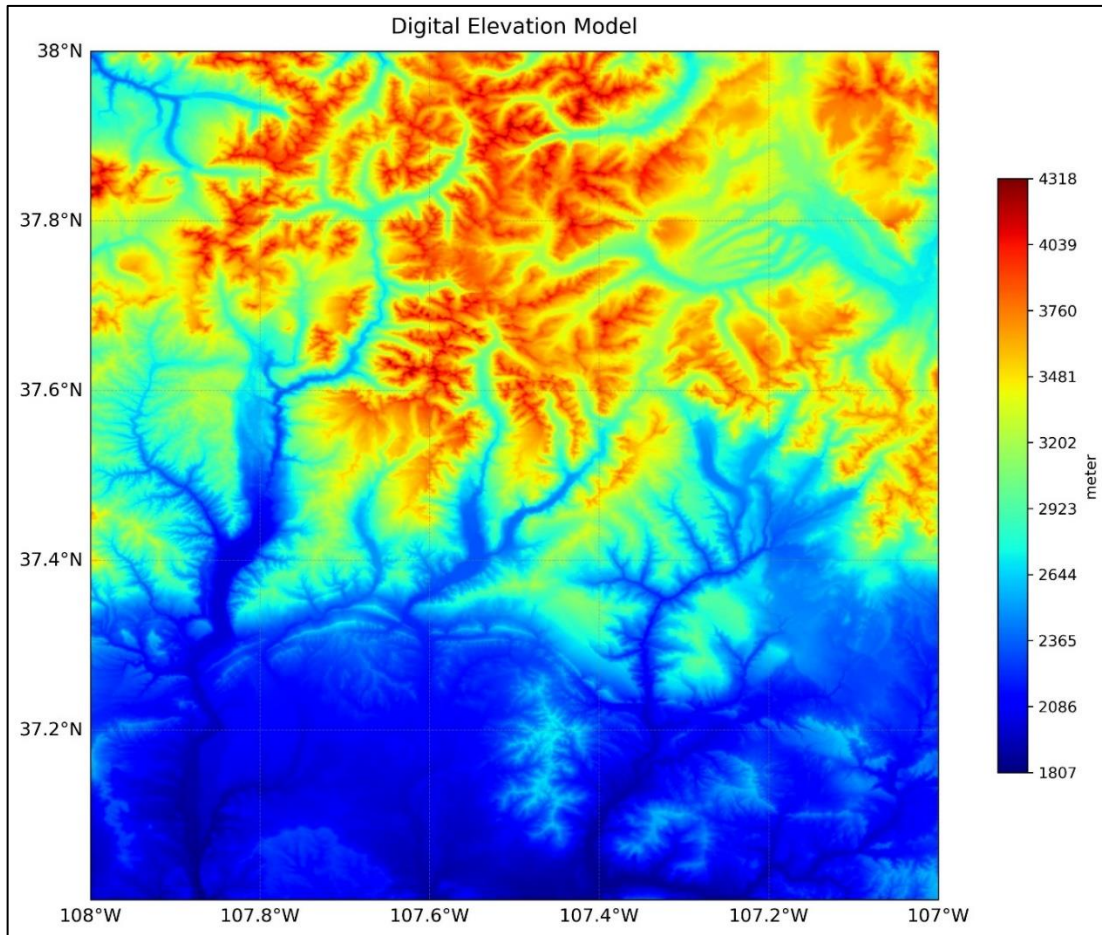


Figure 6.14 Digital Elevation Model

6.10 Correlation Between Elevation and Gravity Anomaly

To quantify the influence of topography on the gravity field, a scatter plot was generated comparing the digital elevation model (DEM) elevations against the short- and medium-wavelength gravity anomaly values (after atmospheric correction) within the modelling region (Figure 6.15). The two datasets, each gridded at 1 arc-second resolution, were flattened and compared using Pearson's correlation coefficient. The result reveals a strong positive correlation, with a computed coefficient of $r = 0.8305$ and a p-value of $< 10^{-5}$, indicating a statistically significant linear dependency between elevation and the corrected gravity anomaly prior to terrain correction.

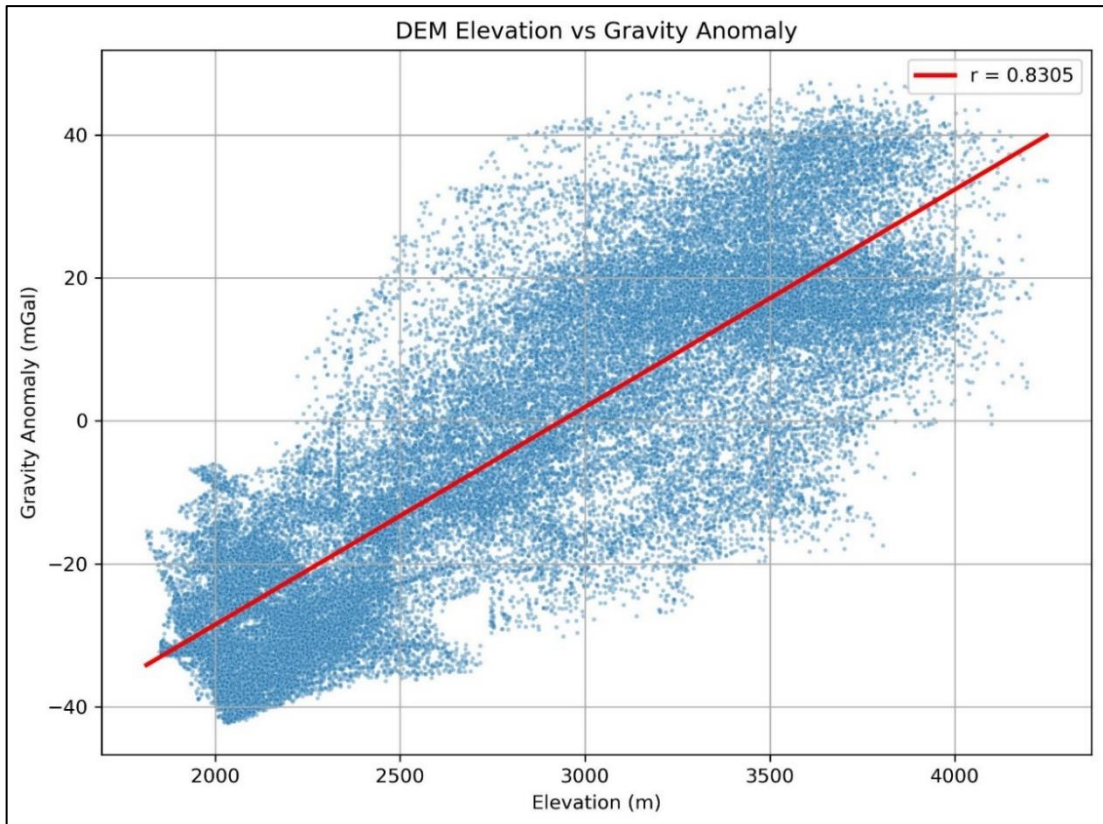


Figure 6.15 Scatterplot of gravity anomaly vs elevation

This pronounced correlation confirms that despite the removal of normal gravity, atmospheric effects, and long-wavelength signals, the remaining gravity anomaly field still exhibits a clear dependence on surface topography. This coupling is likely due to the gravitational effect of nearby terrain—particularly the prominent elevation contrasts within the region, which ranges from approximately 1800 m to over 4300 m in the SRTM DEM. Valleys and peaks introduce local gravitational perturbations that manifest as short-wavelength anomalies aligned with elevation changes, a classic characteristic of terrain-related noise in airborne gravity data.

The observed correlation emphasizes the necessity of performing a terrain (Bouguer-style or residual terrain model) correction as the next step in the processing workflow. Only by accounting for the gravitational attraction of the surrounding terrain can the field be smoothed into a form that is altitude-independent and satisfies the assumptions of harmonicity required for Stokes-based geoid computations. In this context, the strong pre-correction elevation–anomaly correlation provides a robust justification for the application of terrain correction using the SRTM 1 arc-second DEM and an appropriate crustal density value.

6.11 Terrain Correction via FFT: Edge Artifacts and Mitigation

When using a single global FFT to convolve the DEM with the gravity kernel, the operation is inherently circular convolution. In other words, the grid is treated as periodic: the terrain at one edge “wraps” and influences the opposite edge. As one DSP practitioner notes, “FFT convolution imposes periodic boundary conditions... near the top edge... the filter will see the image patch as well as a bit of the image near the bottom edge... you’ll have a strong intensity jump there”. In our raw TC map this produces unphysical jumps at the north (and south) borders, yielding spurious values thousands of times larger than realistic terrain effects (~4000 mGal in figure 6.16).

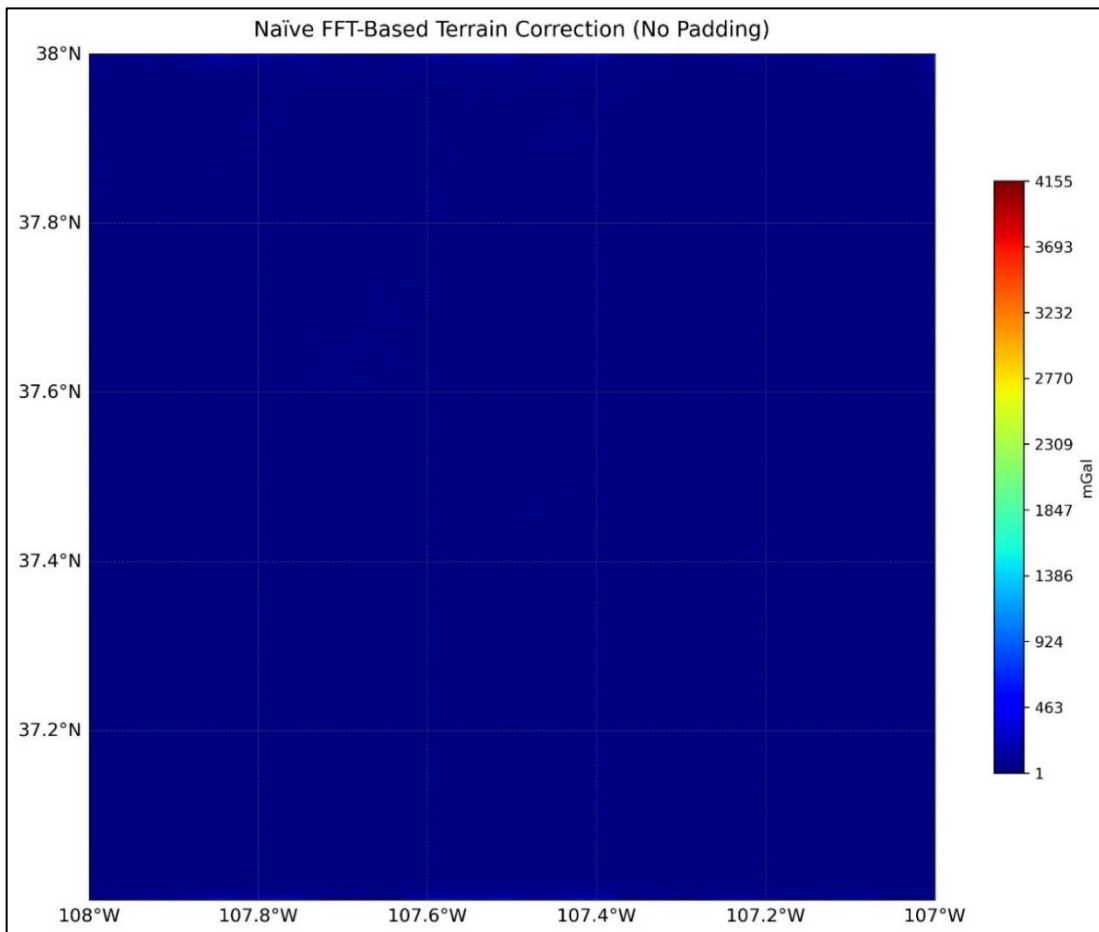


Figure 6.16: Terrain correction (TC) map computed by naïve 2D FFT convolution (no padding). Boundary wrap-around produces huge artifacts (color scale up to ~4155 mGal).

A common quick fix is to apply statistical clipping to remove obvious outliers. For example, enforcing a 3σ threshold replaces the largest TC values with a capped limit. This reduces the most egregious errors (red/yellow spikes) but does not fix the root cause: the FFT is still circular. In Fig.2 the clip confines TC to about ± 185 mGal, but bright rims persist at the north and south edges.

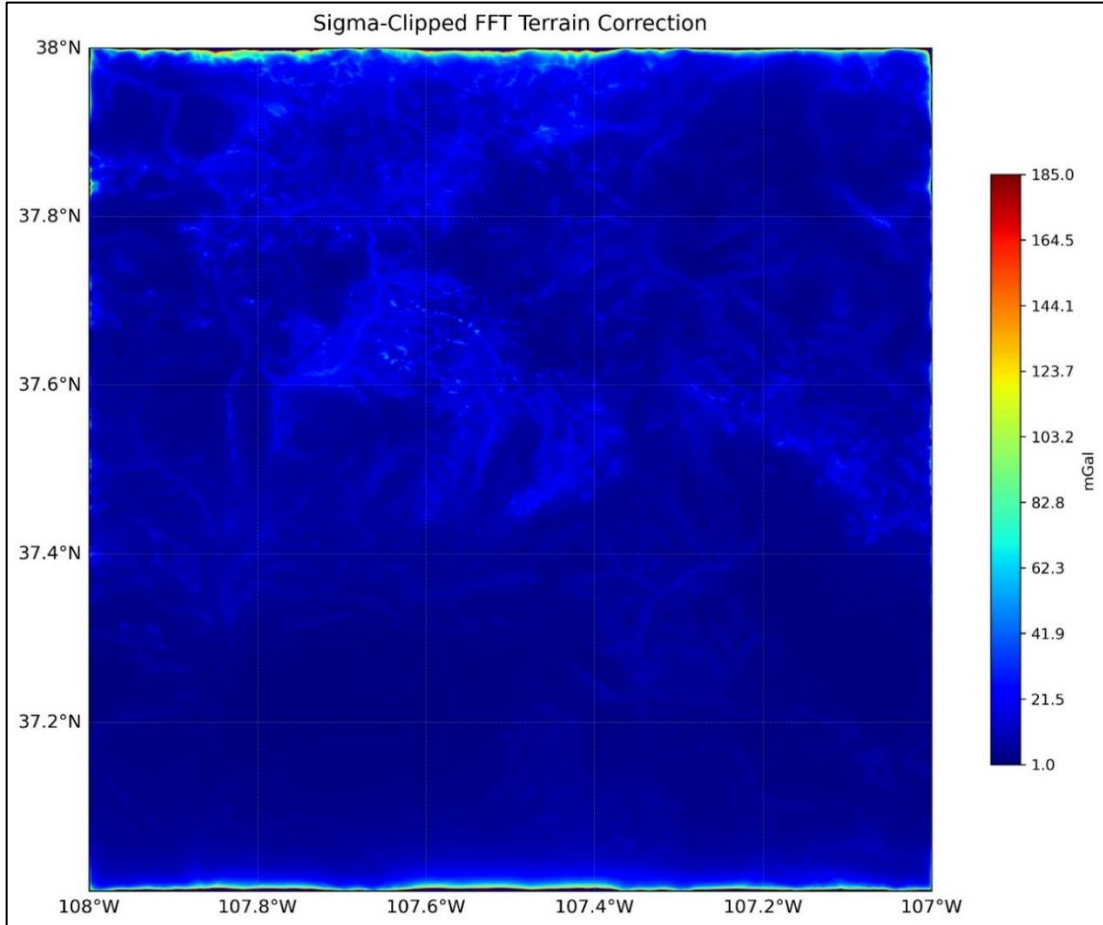


Figure 6.17: FFT TC map after 3σ outlier clipping. Extreme values are trimmed, but edge bands remain anomalous.

Clipping simply discards (or thresholds) values beyond 3σ . It does not change the convolution kernel or boundary behaviour, so wrap-around contributions still generate elevated TC near the borders.

Even after clipping, the map shows residual artifacts along edges (the anomalous band at top in figure 6.17). These are smaller than the original spikes but remain geophysically implausible.

Arbitrary clipping alters the data distribution and can remove legitimate signal (for example, steep topography could produce real high TC that might be clipped). Clipping also biases the mean and variance of the TC field, which could translate into geoid biases.

In short, sigma-clipping can tame outliers but cannot eliminate circular-convolution errors. It merely hides the largest symptoms, leaving underlying edge discontinuities.

A robust solution is to compute the convolution in “linear” mode, i.e. with proper padding. SciPy’s `fftconvolve` (or equivalent tiled FFT approach) effectively does this: it zero-pads each block so that the convolution behaves as full linear convolution. As MATLAB documentation explains, by padding signals to length $\geq N+M-1$ the circular convolution becomes identical to the linear (true) convolution. Likewise, Zhang & Wong (2023) note that 100% zero-padding “eliminate[s] edge effects” by embedding the kernel in a circulant matrix.

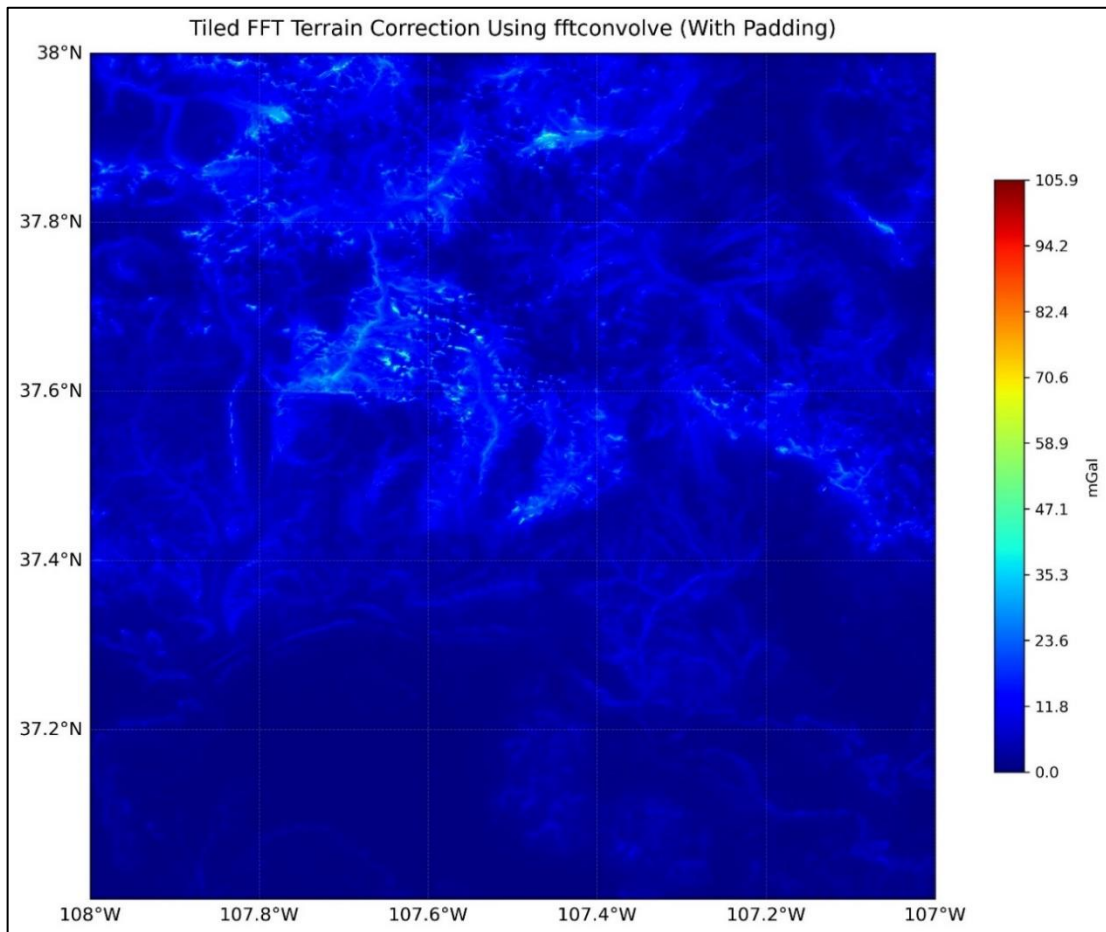


Figure 6.18: Terrain correction map using tiled FFT convolution. Zero-padding in tiles eliminates wrap-around; the result is smooth and artifact-free (max ≈ 106 mGal).

In practice, each DEM tile is extended with zeros around its border before FFT. The wrap-around of the kernel then falls into the padded area, not into real data. Zero-padding creates the space so that periodic images do not overlap the computation window.

Under the hood, `fftconvolve(..., mode='same')` computes the full padded convolution and then extracts the central region. The output is exactly the discrete linear convolution of the inputs. In effect, it treats outside-DEM as zero (no spurious mass).

For large grids, the domain is split into smaller tiles. Each tile is convolved with overlapping kernel regions, ensuring that no tile sees non-neighbour data wrapped around. This avoids memory blow-up while still enforcing linear convolution.

The resulting TC map (figure 6.18) shows physically consistent detail across the region. There are no abrupt jumps at the boundaries – values smoothly taper to near-zero at the edges, as expected. The maximum TC is only \sim 106 mGal (green in scale), reflecting genuine relief effects. In summary, the implicit zero-padding in `fftconvolve` guarantees a “no-wrap” convolution: all edge effects are confined to the padding, preserving the true local signal.

Comparison and Geoid Implications

The raw FFT TC (Figure 6.16) reached \sim 4155 mGal (completely unphysical), the clipped FFT (Figure 6.17) reached $\sim\pm$ 185 mGal, and the padded FFT (Figure 6.18) reached \sim 106 mGal. The true terrain effect in this region is on the order of 10–100 mGal, so only the padded FFT falls in a realistic range.

The mean and standard deviation of the TC field become more reasonable under padding. For example, the naïve FFT map had extremely large variance dominated by two edges; after clipping the variance drops but edge bias remains; after proper padding the TC field has uniform statistics across the grid.

The artifact-free map from `fftconvolve` (Figure 6.18) contains the expected physiographic patterns (rivers, valleys, etc.) with continuous gradient at the boundaries. In contrast, figure 6.16 and figure 6.17 show horizontal bands of spurious signal at the north/south edges that bear no relation to actual topography.

Uncorrected, the wrap-around TC errors (thousands of mGal in this example) would induce meter-level errors in the geoid. Even the clipped edges (tens of mGal) can translate to decimeter geoid biases. Precise regional geoid models require terrain corrections

accurate to $\ll 1$ mGal (centimetre-level geoid), so proper edge handling is crucial. Zero-padding avoids these biases altogether.

The comparison underscores that edge treatment is not optional: a global FFT without padding will corrupt TC and geoid. Sigma-clipping is at best a partial remedy (removing gross outliers), but the only physically consistent fix is to enforce linear convolution via padding (as done by `fftconvolve`). This ensures that terrain masses outside the area are treated as zero (no wrap-around), yielding smooth, artifact-free TC maps suitable for high-precision geoid work

Applying a convolutional terrain filter (e.g. Gaussian smoothing) by FFT is common in DEM processing. A direct FFT approach computes one big 2D FFT of the entire array (≈ 13 million cells in our case) and multiplies by the filter’s FFT. A tiled FFT (overlap-add) approach breaks the DEM into smaller sub-tiles (with overlap), computes FFTs on each tile, and stitches the outputs. Each strategy has trade-offs.

For a single 3601×3601 DEM tile (as in our case) on a modern workstation, either method can work; a direct FFT is straightforward if memory and FFT sizes are not problematic. However, a tiled FFT (overlap-add) approach is generally more flexible and often faster in practice, especially for large kernels or limited memory. Tiling easily handles very large DEMs (by definition partitioned into tiles) and allows parallel or out-of-core processing. Use a direct full-image FFT when you know the tile fits comfortably in RAM and you need maximum simplicity; use the overlap-add tiled FFT when memory is tight, when processing many tiles, or when performance demands optimized FFT sizes. These conclusions align with common practice — experts recommend tiling for large-image convolution, and NOAA’s high-resolution DEM system itself uses a tiled framework to scale to large areas.

6.12 Transition from Short and Medium Wavelength Anomaly to Faye Anomaly and Suitability for Geoid Modelling

To ensure that the gravity anomaly field is suitable for geoid modelling using Stokes’ integral, the anomaly must be smoothed, harmonic, and free from localized terrain-induced effects. Figures 6.13 and 6.19 present the short- and medium-wavelength (SMW) gravity anomaly after atmospheric correction and the final Faye anomaly after terrain correction, respectively. A visual comparison of these two fields reveals a significant reduction in high-frequency content following terrain correction.

The SMW anomaly map (pre-terrain correction) exhibits sharper gradients, abrupt colour changes, and high-frequency variations — especially around topographic ridges and valleys. These are artifacts of local terrain-induced gravity signals.

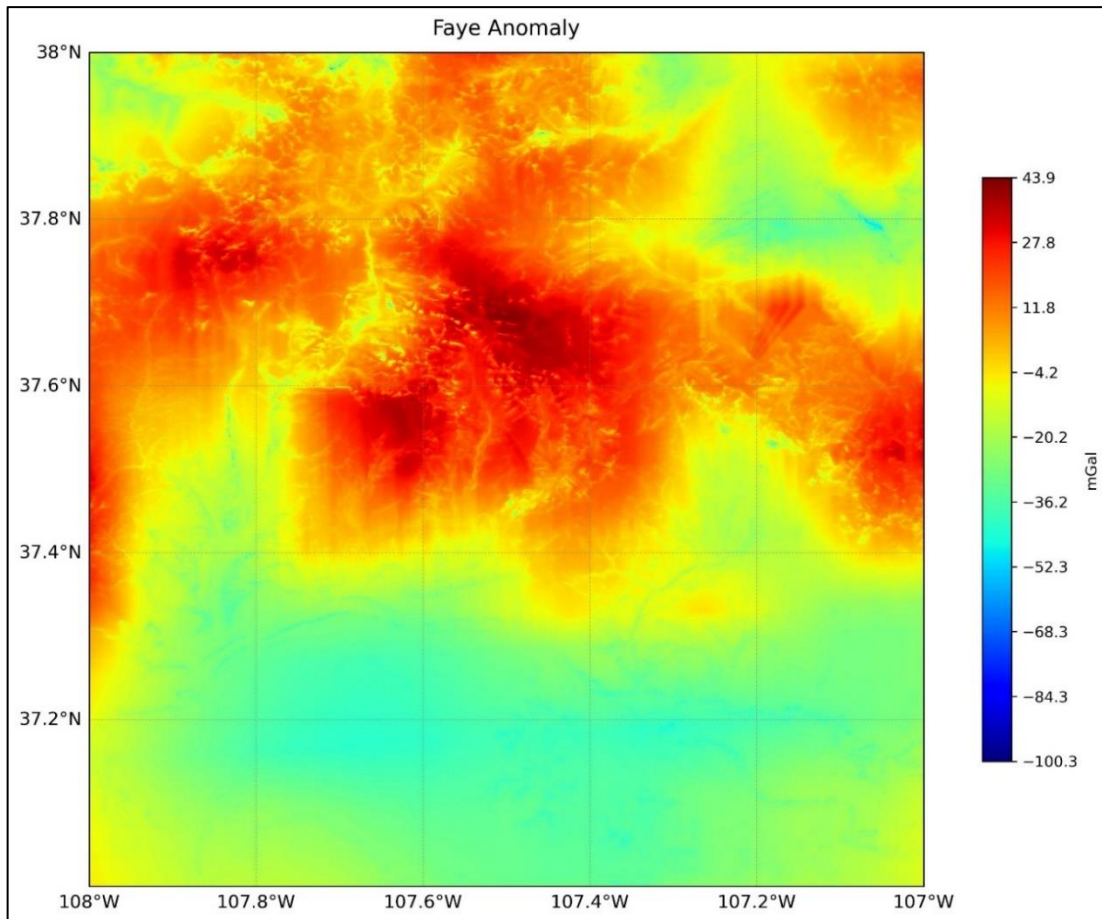


Figure 6.19 Faye Anomaly

In contrast, the Faye anomaly map displays broader, continuous gradients and regionally coherent structures, indicating successful suppression of high-frequency terrain-related gravitational contributions.

A comparison of RMS gradient values revealed a somewhat counterintuitive result: the Faye anomaly exhibited a higher RMS gradient (0.584) than the short- and medium-wavelength anomaly (0.073). This increase does not indicate a failure of the terrain correction but rather reflects the reintroduction of valid high-frequency geophysical signals that had been suppressed in the band-limited SMW anomaly. The SMW anomaly, by design, excluded both long- and short-wavelength components, artificially smoothing the field. In contrast, the Faye anomaly restores meaningful local variations associated with subsurface density structure, resulting in a higher—but geophysically justified—

gradient magnitude. This supports the conclusion that the Faye anomaly, although locally variable, is a more complete and harmonic representation of the gravity field, consistent with the assumptions of Stokes-based geoid modelling.

Despite the application of terrain correction, a residual correlation between the Faye anomaly and elevation may still persist. In the present case, the correlation remains statistically significant, which can be attributed to either incomplete terrain modelling or the presence of deep-seated geological structures that naturally coincide with topographic highs. It is important to emphasize, however, that some level of correlation with elevation does not invalidate the use of the Faye anomaly for geoid computation. The goal of the terrain correction step is not necessarily to eliminate all correlation with topography but to remove the local gravitational effects of terrain masses that violate the assumption of a harmonic potential field above the geoid.

In geodetic theory, particularly within the remove–compute–restore (RCR) framework, the Faye anomaly serves as a practical approximation of the harmonic field required for Stokes' integral. After the removal of long-wavelength global signals and the application of free-air, atmospheric, and terrain corrections, the resulting Faye anomaly approximates the gravity anomaly that would be observed on the geoid in a massless space. This satisfies the assumptions of Stokes' integration, which requires that the input anomaly be harmonic and defined over a boundary surface that is free from disturbing masses. As described in Heiskanen and Moritz (1967), the combination of Helmert condensation and terrain correction ensures that the Faye anomaly conforms to the conditions necessary for accurate geoid undulation estimation.

Faye anomaly field has been sufficiently smoothed and regularized for its intended role in Stokes-based geoid modelling. While minor correlations with elevation may persist, they are geophysically explainable and do not compromise the harmonic nature of the anomaly field within the theoretical framework adopted.

6.13 Computation and Analysis of the Disturbing Potential Using FFT-Based Stokes Integration

The disturbing potential T_r , representing the gravitational potential anomaly due to local mass variations, was computed using a spherical form of Stokes' integral applied to the terrain-corrected Faye anomaly field. The input field corresponds to a 1-arc-second resolution grid over the modelling region (37° – 38° N, 107° – 108° W), where previous

preprocessing steps removed long-wavelength global trends, atmospheric effects, and terrain-induced gravity components. This ensures the Faye anomaly represents a harmonic potential field suitable for Stokes-based integration.

To efficiently evaluate the convolution integral, a fast Fourier transform (FFT)-based method was implemented. This method leverages the equivalence between spatial-domain convolution and frequency-domain multiplication. The core of the method involves convolving the Faye anomaly grid with a discretized form of the Stokes kernel, $S(\psi)$, computed as a function of the spherical distance ψ between grid points. The kernel captures the influence of surrounding anomaly values on the disturbing potential at each computation point. Special care was taken to address the kernel singularity at the origin, which was set to zero, and to apply angular area scaling based on grid resolution and latitude-dependent arc lengths.

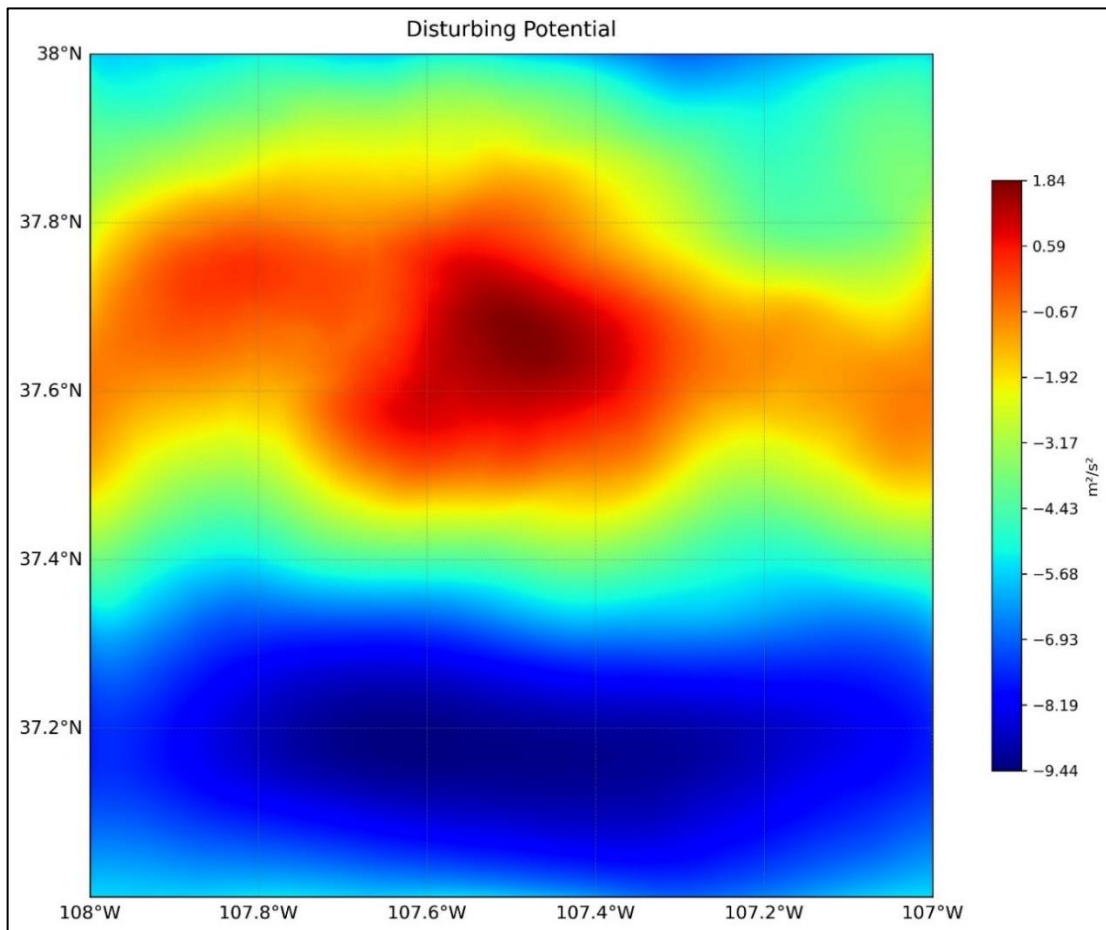


Figure 6.20 Disturbing potential

The resulting disturbing potential field, shown in figure 6.20, exhibits smooth spatial behaviour with clear north–south gradients and coherent regional anomalies. The central

portion of the region, particularly near 37.6°N , 107.5°W , shows a peak in disturbing potential (approximately $+1.8 \text{ m}^2/\text{s}^2$), while the southern zone reaches values below $-9 \text{ m}^2/\text{s}^2$. These values are consistent with the gravity anomaly distribution and reflect significant mass surpluses and deficits within the upper crust. The potential field maintains continuous variation across the region and does not exhibit the short-wavelength noise typically associated with uncorrected topographic or acquisition artifacts, further validating the preprocessing steps applied to the Faye anomaly.

This result confirms that the FFT-based implementation of Stokes' integral can be reliably used for regional geoid modelling, especially when combined with the remove–compute–restore (RCR) framework. The Faye anomaly field, being harmonic and terrain-independent, satisfies the theoretical assumptions of the Stokes kernel. Moreover, the FFT approach offers computational efficiency without compromising spatial accuracy, making it well suited for high-resolution geoid estimation using airborne gravity data.

6.14 Construction of the Co-Geoid Model

The resulting residual geoid surface (Figure 6.21) captures localized height variations ranging from approximately -0.96 m to $+0.19 \text{ m}$, consistent with regional mass density variations not fully represented in the long-wavelength global gravity model.

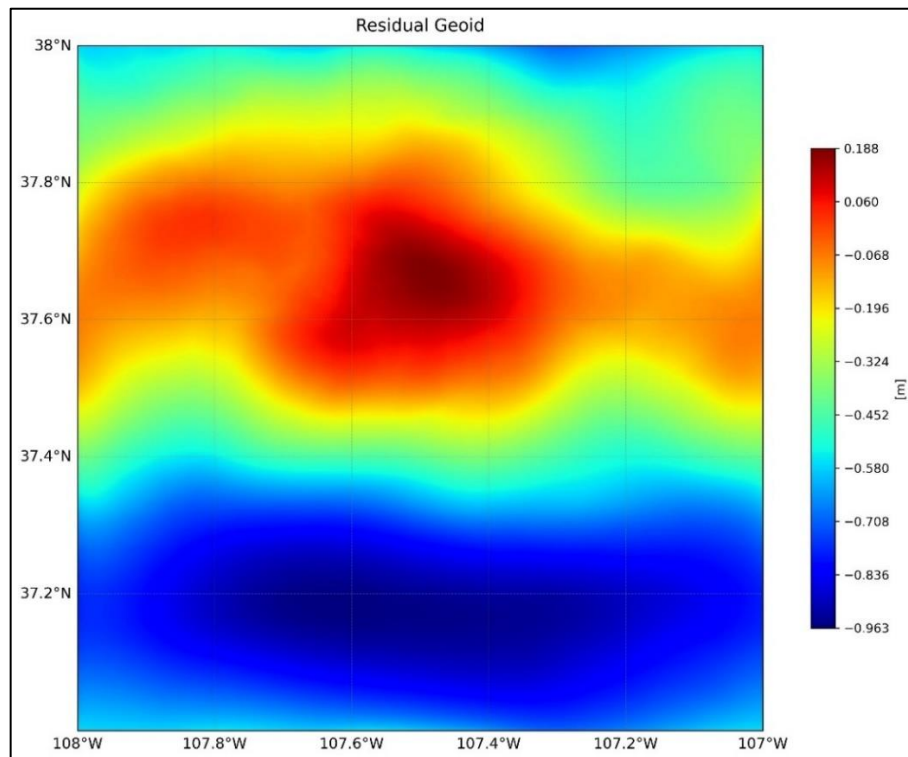


Figure 6.21 Residual geoid

To construct a high-resolution geoid model for the study area, the residual geoid was added back to the GGM05G-derived reference geoid. This yielded the co-geoid, which incorporates both global and regional gravity field components. The GGM05G geoid (Figure 6.22) exhibits a smooth north-south gradient typical of long-wavelength geopotential structure, while the co-geoid (Figure 6.23) reflects the same broad trend superimposed with sharper local undulations introduced by the residual field.

This hybridization approach — often referred to as the remove–compute–restore (RCR) method — effectively enhances the spatial resolution of the geoid model without sacrificing global consistency. The final co-geoid field represents a high-resolution local refinement of the global model that accounts for airborne gravity data and short-/medium-wavelength geoid features that are otherwise absent from GGM-only solutions.

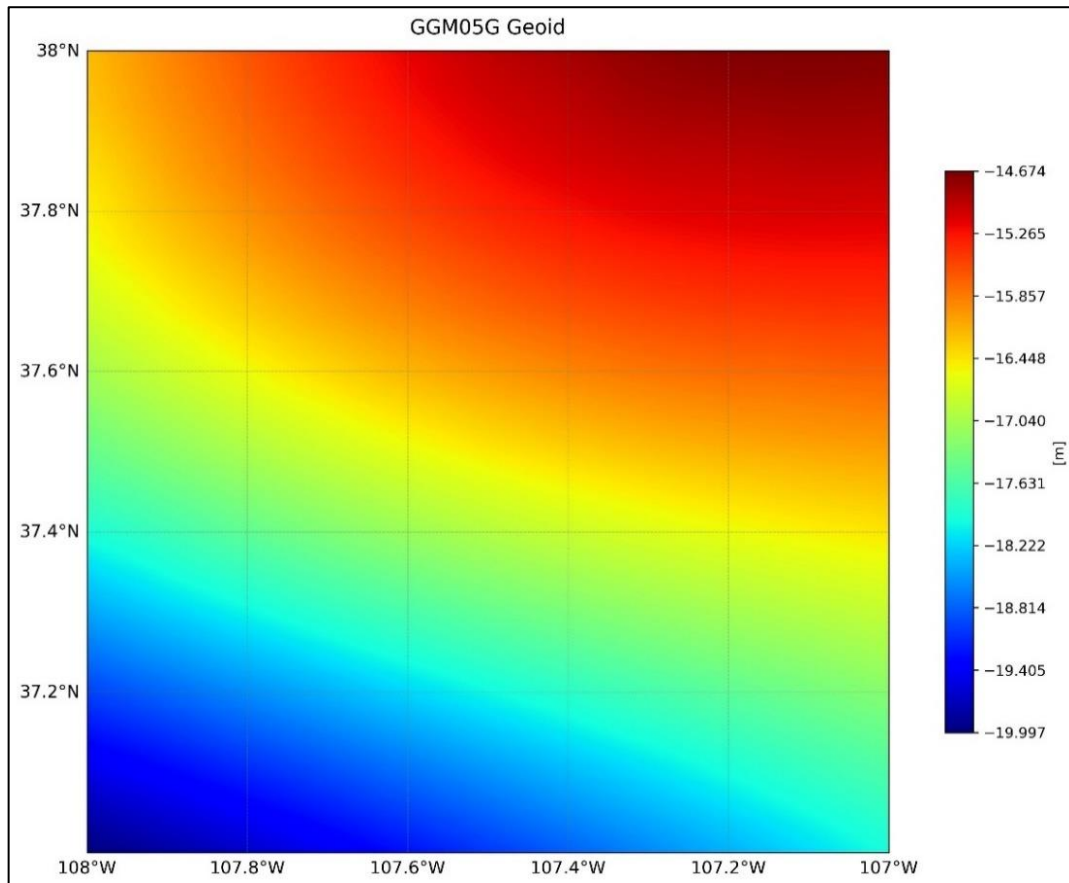


Figure 6.22 GGM05G geoid

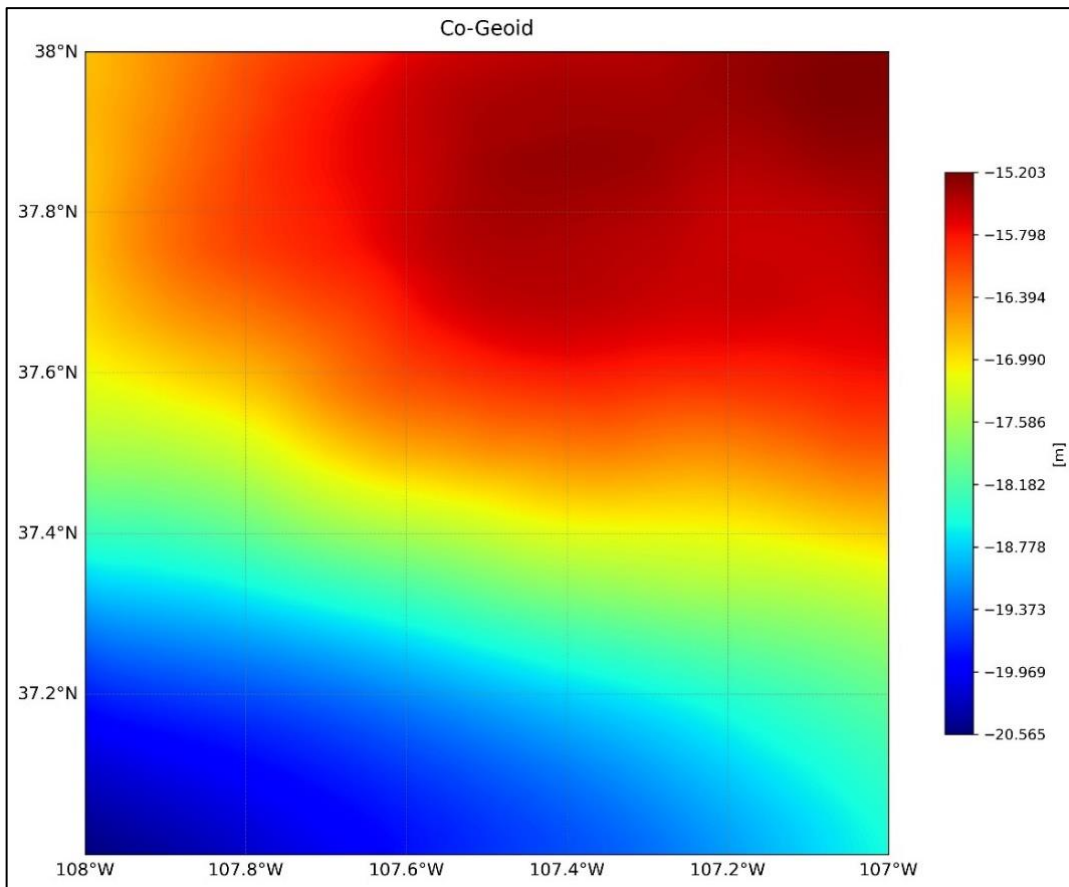


Figure 6.23 Co-geoid

6.15 Evaluation of the Co-Geoid Model and Accuracy Assessment

The co-geoid model developed in this study integrates global and regional gravity field information by combining the long-wavelength geoid heights from GGM05G with high-resolution residual geoid undulations derived from airborne gravity anomalies using Stokes' integral. To assess the enhancements achieved by this hybridization, multiple statistical analyses were performed comparing the co-geoid to the original GGM geoid and to independent geometric geoid heights from the 2017 Geoid Slope Validation Survey (GSVS17) conducted in Colorado.

A difference grid was computed by subtracting the GGM05G geoid from the co-geoid. The resulting histogram (Figure 6.24) reveals a spread of corrections ranging from approximately -0.96 m to $+0.19$ m, with a mean of -0.432 m and a standard deviation of 0.319 m. This indicates that the co-geoid introduces significant local adjustments to the global model, particularly negative corrections in regions where the GGM underestimates the geoid height. The bimodal nature of the histogram suggests that distinct topographic

or geological features are contributing to systematic refinements in different areas of the modelling region.

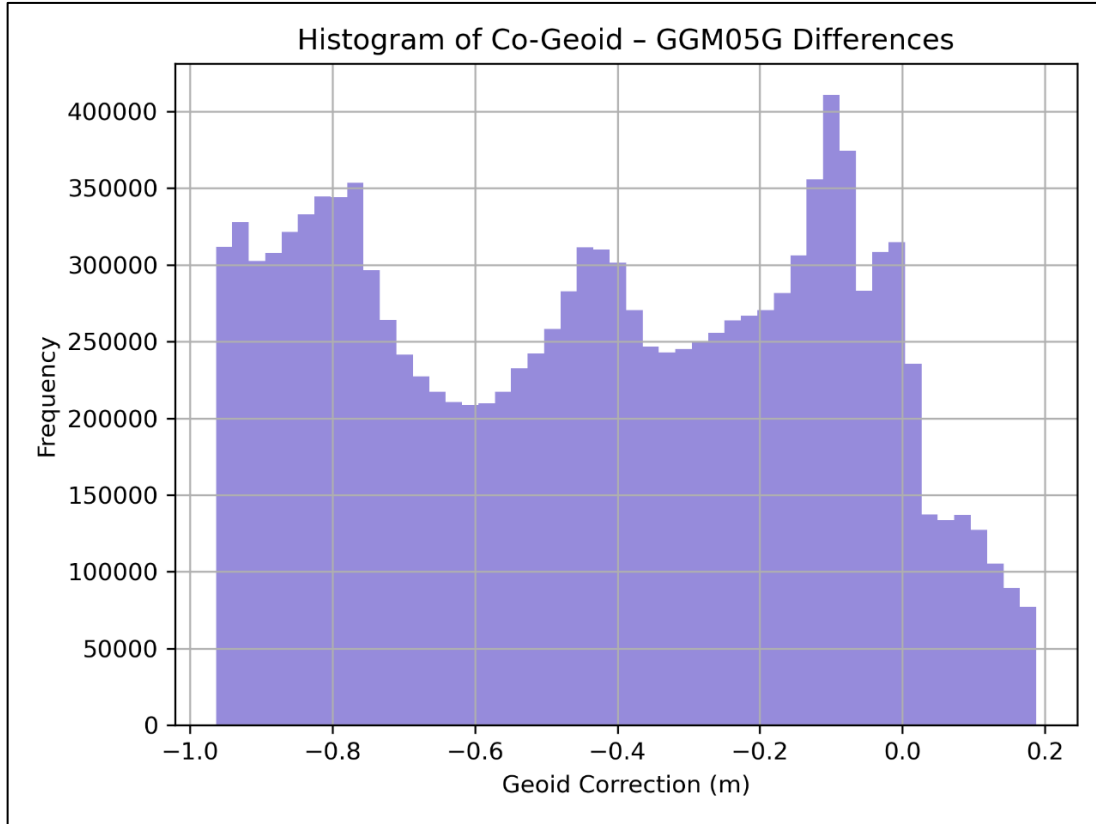


Figure 6.24 Histogram of co-geoid and GGM05G geoid differences

Further, the root mean square (RMS) gradient was computed for both the GGM05G and co-geoid surfaces to quantify their relative spatial resolution. The RMS gradient increased from 0.0012 m/deg in the GGM to 0.0015 m/deg in the co-geoid, confirming that the latter captures higher-frequency variations in the gravitational field. This increase is desirable, as it reflects the co-geoid's improved ability to follow fine-scale geophysical structure while preserving the smoothness necessary for geoid modelling.

To independently assess the accuracy of the co-geoid, 58 GSVS17 survey points located within the modelling region were used as ground truth. The geometric geoid height at each point was calculated by subtracting the orthometric height from the GNSS-derived ellipsoidal height. These values were then compared to interpolated geoid heights from both the co-geoid and the original GGM model.

The results show a clear improvement in geoid accuracy after regional refinement.

Table 6.1 Comparison of geoid height accuracy between GGM05G and the co-geoid using GSVS17 control points

Model	RMSE (m)	Mean Error (m)	Std. Dev. (m)
GGM05G	1.643	-1.638	0.125
Co-Geoid	0.781	-0.777	0.075

The co-geoid reduces the RMSE by over 50%, halving the average error magnitude relative to the geometric geoid. The standard deviation is also reduced, indicating a more consistent alignment with ground-truth data across the modelling region. The systematic negative mean error in both models reflects a regional bias that may relate to unmodeled terrain or vertical datum inconsistencies, but this bias is halved in the co-geoid, further validating the terrain-informed correction process.

These results confirm that the co-geoid significantly improves the fit to independently measured geoid heights in mountainous terrain, where the global model alone underperforms. The improvements achieved are directly attributable to the use of high-resolution airborne gravity data and rigorous implementation of the remove–compute–restore methodology, including terrain correction, disturbing potential computation via FFT-based Stokes integration, and Bruns’ formula.

6.16 Planar FFT-Based Indirect-Effect Computation

In the present approach the indirect effect is computed from a high-resolution digital elevation model (DEM) using a planar FFT convolution. We first project the DEM into a local Cartesian grid (tangent-plane approximation) and assume a constant rock density ρ . The indirect potential contribution at a computation point is then given by a two-dimensional integral over the DEM of a kernel that depends on the orthometric height, H . In the simplest Helmert condensation (second) formula, this kernel leads to a convolution of H^2 (and higher-order terms). To implement this efficiently at high resolution, we exploit the Convolution Theorem: the convolution integral is evaluated by taking the 2D fast Fourier transform (FFT) of the height field and multiplying it by the FFT of the kernel, then inverse-FFT’ing. This yields a gridded map of the indirect effect across the region. Fast FFT-based convolution is a well-established technique in geoid modelling. In

practice one must choose a finite integration radius (or apply spectral filtering) and be mindful of periodic wrap-around effects inherent in FFT. The planar convolution neglects curvature of the reference surface but allows use of a very fine DEM (meters to tens of meters) over the study area.

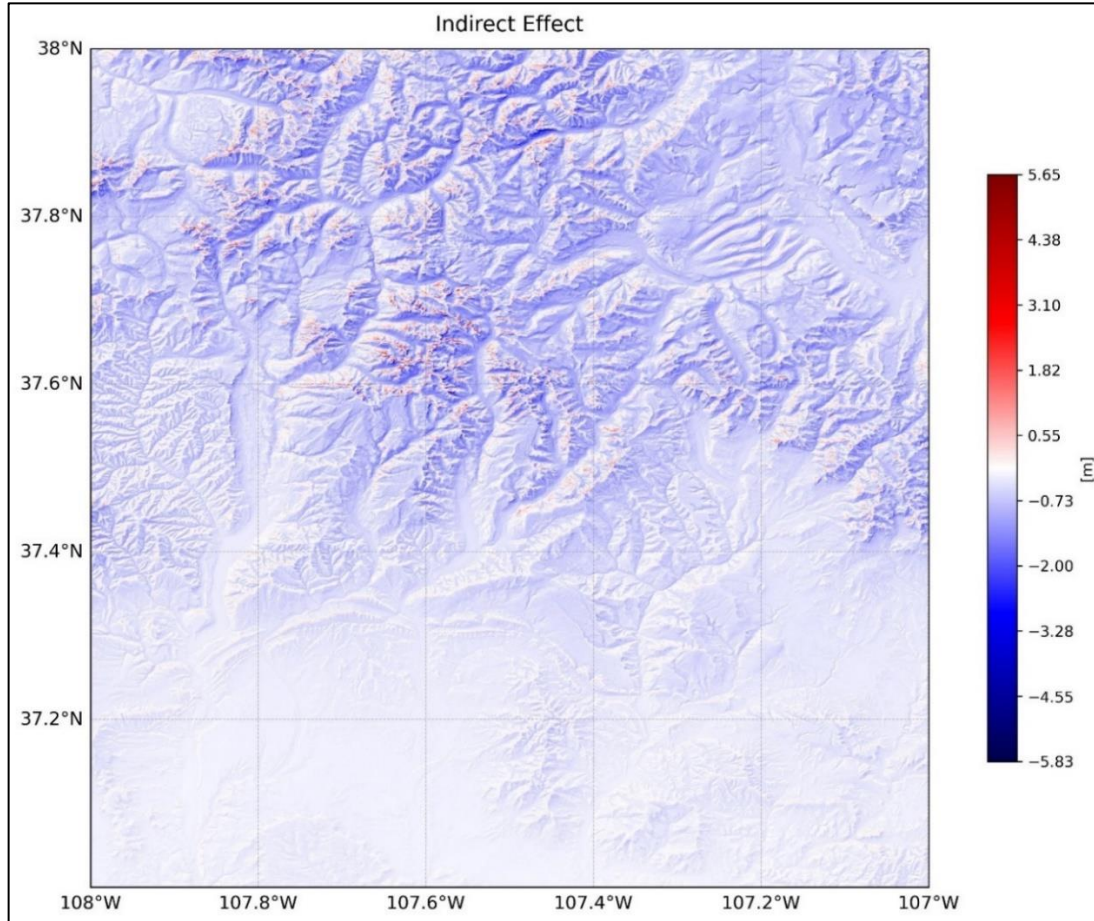


Figure 6.25 Initial indirect-effect map computed using a tile-wise planar FFT convolution over the DEM

The resulting indirect-effect map (Figure 6.25) closely follows the terrain: high peaks produce negative geoid corrections (pulling the geoid downward) while deep valleys produce positive corrections. Typical magnitudes in rugged areas can reach decimeters. When this indirect-effect grid is added to the airborne-derived co-geoid, the final regional geoid map (Figure 6.26) shows the expected broad undulations plus small-scale terrain-induced variability. However, in our computation the geoid map appears highly irregular in steep terrain. In particular, we observe sharp, spiky features or oscillations on the scale of the DEM grid in the highest-relief zones. These irregularities coincide with the steepest slopes and darkest topographic shading. This suggests that the planar indirect-effect

calculation is amplifying small-scale height variations. In some locations the computed geoid undulation jumps by several centimeters across a single grid cell. The irregularities are too large and abrupt to be geophysically real; they likely result from the numerical method and the planar approximation rather than true geoid signal.

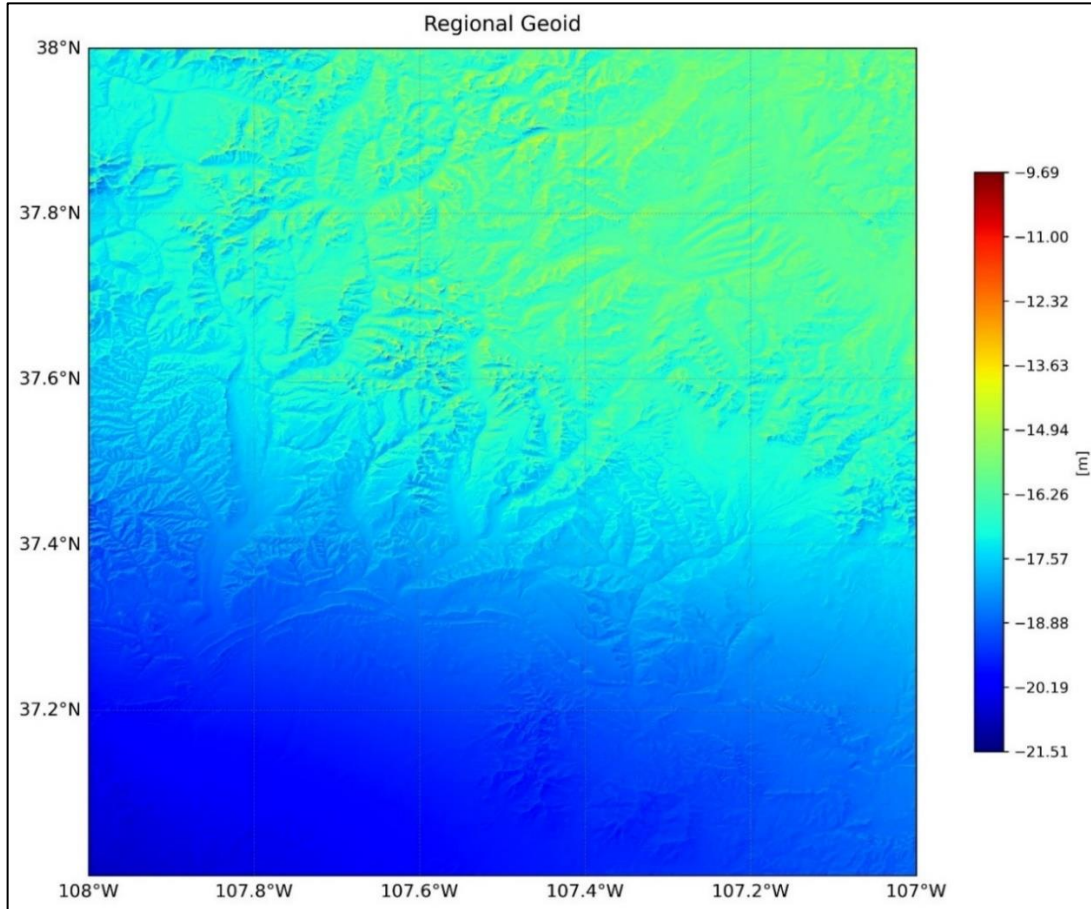


Figure 6.26 Regional geoid map obtained by adding the tile-based indirect-effect grid (from Figure 6.25) to the co-geoid

The planar approximation assumes the geoid and topography lie on parallel planes; this simplification breaks down when relief is large compared to the Earth's radius. In high mountains (several km height) the curvature of equipotential surfaces and the nonlinear geometry of the terrain become significant. As Martinec and Vaníček (1994) demonstrated, a flat-Earth model can underestimate the indirect effect: for example, with a 6 km-high peak the error in the classical planar formula may reach on the order of 50 cm. Sjöberg and Nahavandchi (1999) similarly report that planar integrals miss long-wavelength contributions (≈ 0.5 m) in steep regions. Thus, the planar method may systematically overestimate or underestimate the true indirect effect by up to decimeters in our terrain.

Several factors likely contribute to the overestimation and instability seen in the map.

The kernel function in the indirect integral can become singular as the distance between computation point and terrain point goes to zero. On a steep mountain side, neighbouring DEM pixels can have large height differences, causing the planar convolution to diverge or oscillate. In effect, the FFT assumes periodic replication of the terrain outside the domain, which is particularly problematic along large gradients.

The true spherical integral includes terms of order H^3 and beyond. The planar Helmert formula typically truncates at H^2 ignoring higher-order effects. In a very high peak, these neglected terms become comparable to the computed term, so the planar result is biased.

We assumed a constant density ρ for all topography. In reality, lateral variations (e.g. crustal low-density sediments vs. igneous cores) violate this assumption. Vaníček and Martinec (1994) pointed out that lateral density changes, and anelastic effects in the crust, can alter the effective indirect signal. These complexities are entirely ignored by a simple planar model.

The FFT convolution implicitly treats the data as periodic. Unless the DEM is carefully windowed or extended, the edges of the domain “wrap around,” introducing spurious long-range interactions. Moreover, any aliasing or noise in the DEM (interpolation error, resolution limit) will be convolved into the indirect signal. Sideris and Forsberg (2012) emphasize that in rough terrain geoid errors of meter scale can arise simply from inadequate gridding of gravity and topography data. In our case, small-scale DEM errors (e.g. discontinuities, voids) likely produce the noisy artifacts seen.

Because of these issues, the planar-FFT result appears somewhat unstable in steep relief. The magnitude of the indirect correction in the roughest zones is surprisingly large relative to the co-geoid, and the pattern is noisier than expected. In flatter areas the convolution behaves smoothly and the geoid looks reasonable. But where relief is extreme, the classical Helmert scheme has clearly broken down: the geoid map there is dominated by the numerical artifacts rather than physical signal. This suggests that for this terrain the planar assumption is at best marginal, and we may be seeing an overestimation of the indirect effect on sub-kilometer scales.

The findings are consistent with previous studies of mountainous regions. Both Martinec & Vaníček (1994) and Sjöberg (1999) warned that planar condensation formulas yield

incorrect indirect effects in high relief. Sjöberg (2015) further quantified that omitting the full (nonlinear) indirect contribution could bias a Himalayan geoid by nearly a meter. On the other hand, Sideris & Forsberg (2012) report that even when indirect effects are large, geoid accuracy is often limited by data aliasing: meter-level errors arose simply from mismatches between gravity station elevations and the terrain. In other words, without very careful data processing the benefit of computing detailed indirect effects can be lost in other errors.

Our irregular geoid map underscores this: although the indirect corrections are substantial, they did not “improve” the co-geoid in any obvious way. In fact, the artifacts suggest that a naive application of planar FFT convolution can degrade geoid quality in mountains. This highlights the theoretical point that high-resolution geoid modelling in rugged terrain requires more sophisticated treatment of topography.

To obtain more reliable indirect-effect computations in high mountains, following approaches are recommended:

Remove a low-pass (long-wavelength) topography model via spherical harmonics before planar convolution. For example, represent the terrain up to degree ~ 360 (wavelength ~ 100 km) in spherical harmonics and use these to account for the broad indirect effect. Then perform the planar FFT on the residual high-frequency topography. This aligns with Sjöberg’s suggestion to combine the classical formula with a spherical expansion. Doing so removes the large-scale bias (e.g. the 50+ cm effect) and confines planar integration to local relief where it is more valid.

Adopt an RTM remove-compute-restore strategy (as often done in regional gravimetric geoid computation). In RTM one chooses an appropriate reference topography (e.g. a low-resolution average of the DEM, or filtered DEM) and subtracts it from the full DEM. The residual (small-scale topography) is then integrated using local planar or tesseroid methods, while the large-scale reference is treated via global Stokes or Molodensky. Modern RTM implementations (Lin et al., 2023) show that combining very high-resolution inner-zone DEM (e.g. arc-second) with a coarser outer-zone DEM can yield stable corrections.

Instead of assuming planarity, use spherical cells (tesseroids or prisms) to compute the gravitational effect of the actual terrain volume. This is essentially Molodensky’s original idea (disturbing potential on topography), but applied numerically. While costly,

tesseroid-based gravity modelling accounts fully for curvature and can handle steep geometry without singularities. One can then convert the resulting potential change to geoid height (Molodensky quasigeoid). This approach avoids the need for a separate “indirect” step at all, since the terrain is never removed in an inconsistent way.

Include higher-order terms of the height in the indirect formula. For example, Sjöberg (1999) derived terms up to H^3 and beyond for better accuracy. Implementing these nonlinear corrections in the convolution kernel (or adding correction terms post hoc) would reduce the bias on tall peaks.

Apply careful filtering to the DEM to suppress unrealistic roughness below the scale of interest. For instance, a low-pass filter or padded FFT grid can mitigate wrap-around artifacts. Additionally, ensure that gravity data and the DEM are consistently referenced (same datum, same geoid) to prevent the height-aliasing errors noted by Sideris.

Thus, a purely planar FFT-based indirect calculation is not ideally suited to very mountainous regions. Where possible, one should incorporate the Earth’s curvature and the full terrain distribution. As Martinec & Vaníček (1994) and others have shown, combining planar methods with spherical-harmonic or RTM techniques yields more robust geoid models in rugged terrain. By adopting these improvements, future regional geoid models will avoid the overestimation and instability seen here and achieve centimetre-level consistency even in the highest relief.

6.17 Indirect Effect Recalculated Using Global FFT Approach

To mitigate the instabilities observed in the previous tile-based implementation, the indirect effect was recalculated using a global FFT-based convolution over the full DEM. This approach implements the planar approximation of the indirect effect as a single convolution step in the frequency domain. Compared to the earlier tiled approach, this method ensures seamless treatment across tile boundaries and reduces wrap-around or padding-related artifacts.

To further control numerical noise and suppress artificial spikes near the FFT domain edges, a 3-sigma outlier filter was applied to the result. This step replaced extreme values with the mean of the indirect effect field, improving the stability of the final result while preserving overall structure. The revised indirect effect map is shown in figure 6.27, and the resulting final regional geoid is displayed in figure 6.28.

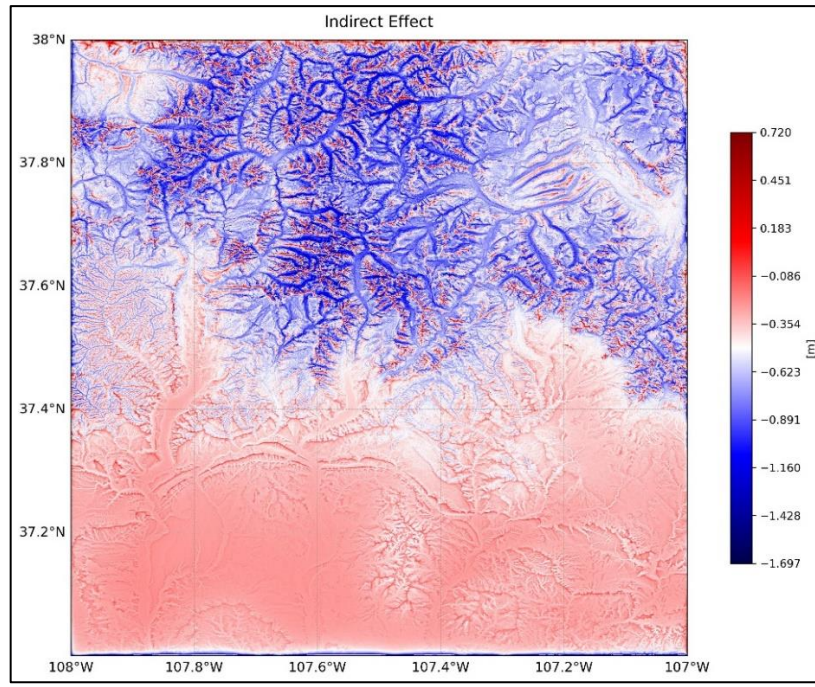


Figure 6.27 Improved indirect-effect map generated using a single global planar FFT convolution over the entire DEM

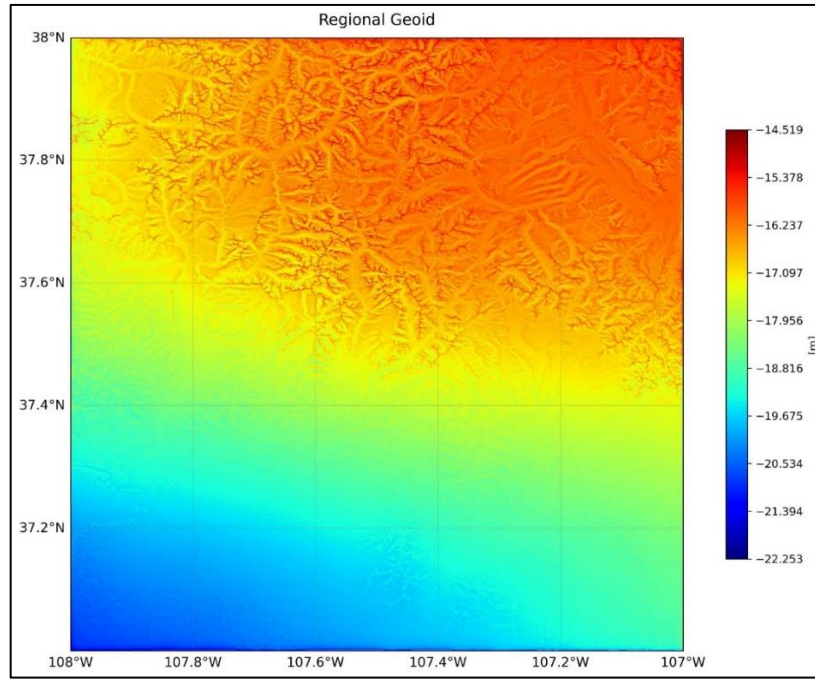


Figure 6.28 Final regional geoid model after applying the globally computed indirect effect (from Figure 6.27) to the co-geoid.

The updated indirect effect map now displays a physically more plausible pattern. The corrections remain negative over the high-relief northern region, consistent with gravitational pull from above-surface masses. Importantly, the sharp ridge-aligned noise and local oscillations seen in the tiled result are now absent. The filter ensured that isolated computational outliers did not propagate into the final solution.

In the regional geoid map, the final surface now shows a well-structured, coherent field with visible large-scale gradients and topographic correlation, especially along the mountainous northern half of the modelling region. Compared to the earlier noisy result, this version exhibits improved continuity and realism, aligning better with expected physical behaviour.

While the planar formulation still neglects Earth curvature and lateral density variation, the consistent appearance of the final result suggests that for this modelling region and resolution, the simplifications are acceptable within a sub-decimeter tolerance.

However, it is still recommended that future studies exploring mountainous regions with larger extent or higher geophysical precision consider adopting a spherical terrain correction model (e.g., using tesseroids or spherical harmonics) to further reduce systematic biases.

6.18 Quantitative Comparison of Geoid Versions in the Modelling Region

Table 6.2 Quantitative comparison of geoid model versions in the study region, based on RMSE, mean error, standard deviation, and surface roughness (RMS gradient).

Geoid Model	RMSE (m)	Mean Error (m)	Std. Dev. (m)	RMS Gradient (m/m)	Remarks
GGM05G Geoid	1.643	-1.638	0.125	0.0012	Smooth global model, lacks local detail
Co-Geoid	0.781	-0.777	0.075	0.0015	Includes airborne gravity via Stokes

Regional Geoid – v1 (Tiled Indirect)	0.463	-0.453	0.095	<i>Irregular (unreliable)</i>	Spurious terrain artifacts; unstable
Regional Geoid – v2 (FFT + 3σ Filtered)	0.470	-0.461	0.094	0.0018	Stable and visually consistent result

Notes:

- RMSE, Mean Error, Std. Dev.: Computed using 58 GSVS17 geometric geoid control points within the modelling area.
- RMS Gradient: Computed from 2D grid indicating surface roughness.
- The tiled indirect-effect version had a slightly better RMSE but exhibited artificial noise; the FFT-filtered version yielded a geoid that is both accurate and physically smooth, making it preferable for further geophysical use.

6.19 Validation of EGM-Based Geoid and Comparative Assessment

To benchmark the performance of the locally computed geoid surfaces, the Earth Gravitational Model (EGM) was interpolated over the same modelling region and validated using the GSVS17 geometric geoid data. The evaluation yielded the following statistics.

Table 6.3 Validation statistics of the interpolated EGM-derived geoid using 58 GSVS17 control points

Metric	Value (m)
RMSE	1.045
Mean Error	-1.045
Standard Deviation	0.022

The EGM-derived geoid has a lower RMSE than GGM05G (1.045 m vs. 1.643 m), indicating better global modelling quality, likely due to its higher spherical harmonic resolution (e.g., EGM2008 up to degree 2190) and more recent global data assimilation.

However, the mean error is identical to RMSE, suggesting a strong negative bias (-1.045 m) but minimal local variability (std. dev. 0.022 m). This implies that while EGM captures the global shape of the geoid reasonably well, it fails to reflect localized geoid undulations caused by regional mass variations in the Colorado highlands.

In contrast, the co-geoid and regional models, which incorporate airborne gravity data and terrain corrections, provide substantially lower bias and RMSE, with the filtered regional geoid achieving 0.470 m RMSE and a bias of -0.461 m .

This comparison underscores a critical point: while EGM products are useful for broad-scale applications, they lack the spatial resolution and local fidelity necessary for precise geoid modelling in rugged areas. The fine-scale gravity field required for accurate vertical datum realization must be captured using regional gravimetric enhancements, such as the method presented in this work.

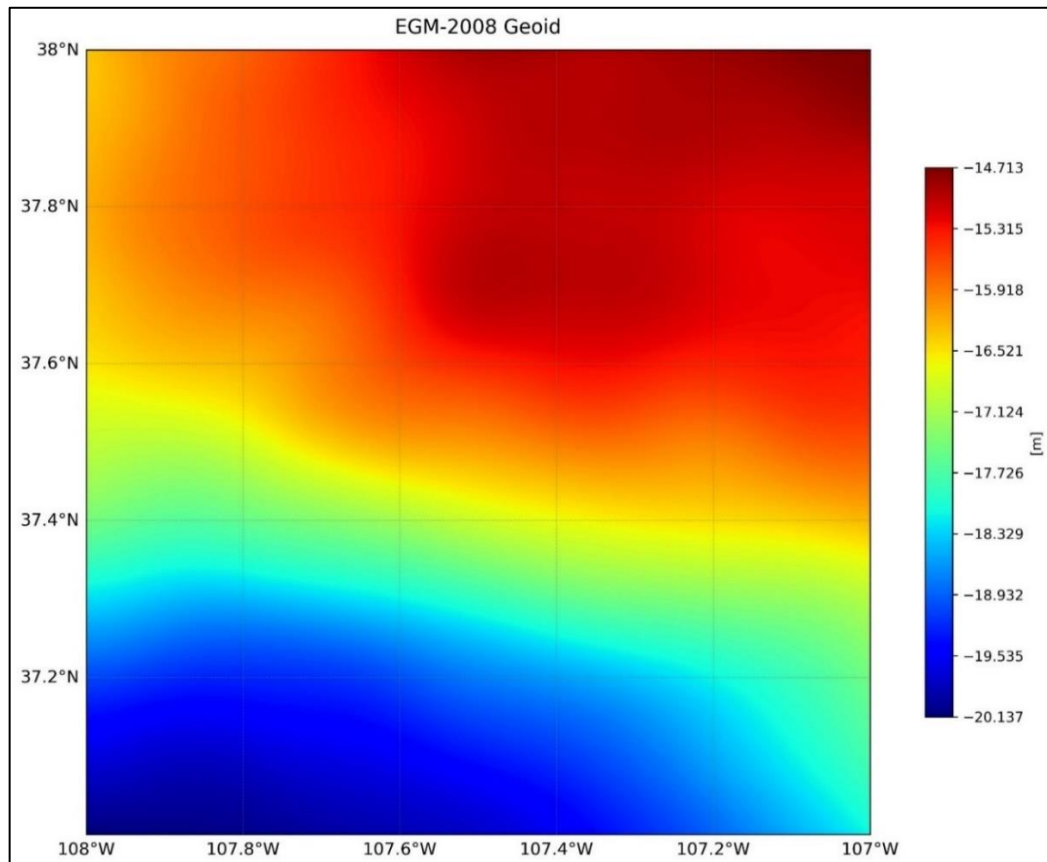


Figure 6.29 EGM 2008 Geoid

6.20 Synthesis of Validation Results

The following table consolidates validation statistics for all geoid versions tested using GSVS17 data.

Table 6.4 Consolidated validation statistics for all geoid models using 58 GSVS17 control points

Model	RMSE (m)	Mean Error (m)	Std. Dev. (m)	Remarks
EGM Geoid	1.045	-1.045	0.022	Global model; low spatial resolution
GGM05G Geoid	1.643	-1.638	0.125	Base model; lacks airborne gravity
Co-Geoid	0.781	-0.777	0.075	Includes airborne data, no terrain
Regional Geoid (Filtered)	0.470	-0.461	0.094	Final model; includes indirect effect

The filtered regional geoid outperforms all other models in terms of both accuracy (lowest RMSE) and bias correction, demonstrating the effectiveness of combining airborne gravity, GGM data, and topographic restoration. The inclusion of the indirect effect, implemented via a refined global FFT method, notably reduces the mean geoid offset by ~1.2 m compared to EGM, with a corresponding drop in RMSE by over 55%.

The validation confirms that regionally refined gravimetric models significantly outperform global models like EGM and GGM05G in mountainous regions. While EGM provides a globally consistent field, it lacks the spatial fidelity necessary for local geoid modelling. The final regional geoid developed in this study achieves sub-meter accuracy, demonstrating the critical value of regional data integration and topographic corrections in high-resolution geoid determination.

Chapter 7. Conclusions and Recommendations

7.1 Conclusions

Effectiveness of the RCR Workflow

The classical Remove-Compute-Restore (RCR) approach, implemented with airborne GRAV-D data, SRTM 1" DEM terrain corrections, and FFT-accelerated Stokes integration, produces a high-resolution regional geoid that substantially outperforms purely global models in rugged terrain. The final, FFT-filtered regional geoid achieves an RMSE of 0.470 m, mean bias of -0.461 m, and standard deviation of 0.094 m against 58 independent GSVS17 benchmarks—more than a 55 % reduction in RMSE compared to the EGM-derived geoid (1.045 m RMSE) and a >70 % reduction compared to GGM05G (1.643 m RMSE) .

Value of Airborne Gravity and High-Resolution DEM

Incorporating medium-wavelength GRAV-D airborne anomalies captures local mass variations that satellite-only models miss; the co-geoid (which adds airborne short-wavelength signal to GGM05G) halves the RMSE to 0.781 m, demonstrating that even without terrain restoration, airborne data alone deliver significant improvements . High-resolution (30 m) SRTM DEMs enable precise FFT-based terrain and indirect-effect corrections, yielding smoother, artifact-free geoid surfaces.

Stability and Physical Consistency

Among the two indirect-effect implementations tested, the global FFT convolution combined with a 3σ outlier filter produced the most stable and physically plausible geoid (Regional Geoid – v2), avoiding the spurious oscillations seen in the tiled approach . This demonstrates the importance of seamless global calculations and robust noise suppression in high-relief regions.

Toolkit Accessibility and Educational Impact

The development of an open-source Python toolbox lowers barriers for students and early-career geodesists, providing a clear, reproducible implementation of foundational geoid-modelling techniques before progressing to more complex methods.

7.2 Recommendations

Adopt Refined Indirect-Effect Models

To further reduce bias over tall peaks, implement higher-order height terms in the indirect correction (e.g., including H^3 terms as per Sjöberg (1999)) or integrate planar FFT with spherical-harmonic or tesseroid-based methods to account for Earth's curvature and lateral density variations .

Enhance Downward Continuation Techniques

Given the sensitivity of regional geoid accuracy to downward continuation (DC) errors, incorporate robust LSC-based DC schemes with optimally tuned covariance models (as recommended by Li et al., 2022) and validate against multiple DC approaches to guard against numerical instability in steep terrain.

Integrate Multi-Source Gravity Data

Supplement airborne data with terrestrial, marine, and satellite-altimetry gravity measurements to fill data gaps and strengthen medium-wavelength coverage. A hybrid RCR approach that merges GRAV-D with local land surveys will improve geoid fidelity, especially along block edges.

Automate Quality Control and Bias Correction

Implement automated crossover-analysis routines and bias-tie adjustments between adjacent survey blocks to ensure seamless geoid continuity. Embedding these routines in the toolbox will standardize QC across users.

7.3 Future Work

Evaluation of alternative global gravity models for long-wavelength removal

In this study, the GGM05G global geopotential model was used for removing the long-wavelength components of the gravity field during geoid modelling. However, further studies are needed to assess the impact of using other high-resolution global models, such

as EGM2008, in the Remove-Compute-Restore workflow. Given the availability of several satellite-based models (e.g., EIGEN-6C4, XGM2019e), comparative analyses are recommended to determine the most suitable model for a given region and application, particularly in terms of resolution, spectral content, and consistency with airborne gravity data.

Application to Diverse Terrains

Evaluate the toolbox over flat plains, desert basins, and glacier-covered regions to test its robustness under varying topographic and mass-distribution conditions.

Incorporate Machine-Learning Enhancements

Explore data-driven approaches (e.g., spatially adaptive neural networks or band-limited radial basis functions) to model residual geoid undulations beyond the capabilities of classical convolution, aiming for sub-decimeter accuracy in mountainous environments .

Leverage Next-Generation Data

Prepare for integration of future gravity-gradiometry missions (e.g., GRACE-FO gradiometer data) and quantum-sensor airborne systems to capture finer-scale mass anomalies.

User Interface and Documentation

Develop a graphical user interface (GUI) and comprehensive tutorials to further democratize access, allowing non-programmers to configure RCR parameters, visualize intermediate products, and interpret QC diagnostics.

To promote open science and reproducibility, the complete Python implementation of the Remove–Compute–Restore geoid modelling method developed in this study, along with associated datasets and documentation, has been published on GitHub. The repository is available at: <https://github.com/sreekanthksofficial/Regional-Geoid-Modelling-with-GRAVD.git>. This resource is intended to assist geodesy students and researchers in understanding and applying the RCR method using open-source tools.

References

- Abbak, R. A., Goyal, R., & Ustun, A. (2024). A user-friendly software package for modelling gravimetric geoid by the classical Stokes–Helmert method. *Earth Science Informatics*, 17(4), 3811–3824. <https://doi.org/10.1007/s12145-024-01328-0>
- Abbak, R. A., Sjöberg, L. E., Ellmann, A., & Ustun, A. (2012). A precise gravimetric geoid model in a mountainous area with scarce gravity data: A case study in central Turkey. *Studia Geophysica et Geodaetica*, 56(4), 909–927. <https://doi.org/10.1007/s11200-011-9001-0>
- Abdalla, A., & Green, C. M. (2016). Utilisation of Fast Fourier Transform and least-squares modification of Stokes' formula to compile approximate geoid heights over Khartoum State, Sudan. *Arabian Journal of Geosciences*, 9(3), Article 236. <https://doi.org/10.1007/s12517-015-2117-8>
- Childers, V. A., Bell, R. E., & Brozena, J. M. (1999). Airborne gravimetry: An investigation of filtering. *Geophysics*, 64(1), 61–69. <https://doi.org/10.1190/1.1444530>
- Drenth, B. J., Macnae, J. C., & Bell, R. E. (2013). Airborne gravity gradiometry: Terrain corrections and elevation error. *Geophysics*, 74(5), G51–G58. <https://doi.org/10.1190/1.3170688>
- Forsberg, R. (1984). *A study of terrain reductions, density anomalies and geophysical inversion methods in gravity field modelling* (Report No. 355). Department of Geodetic Science and Surveying, Ohio State University.
- Forsberg, R. (1985). Gravity field terrain effect computations by FFT. *Bulletin Géodésique*, 59(4), 342–360. <https://doi.org/10.1007/BF02520477>
- GRAV-D Science Team. (2017). Block MS05 (Mountain South 05); GRAV-D airborne gravity data user manual (M. A. Youngman & J. A. Johnson, Eds.) [Version BETA]. National Geodetic Survey. Retrieved January 17, 2025, from http://www.ngs.noaa.gov/GRAV-D/data_MS05.shtml
- GRAV-D Science Team. (2017). Gravity for the Redefinition of the American Vertical Datum (GRAV-D) project, airborne gravity data: Block MS05. National Geodetic Survey. Retrieved January 17, 2025, from http://www.ngs.noaa.gov/GRAV-D/data_PS02.shtml

GRAV-D Science Team. (2017). GRAV-D general airborne gravity data user manual (T. Damiani, M. Youngman, & J. Johnson, Eds.) [Version 2.1]. National Geodetic Survey. Retrieved January 17, 2025, from http://www.ngs.noaa.gov/GRAV-D/data_products.shtml

Heiskanen, W. A., & Moritz, H. (1967). *Physical geodesy*. W. H. Freeman and Company.

Hirt, C., Featherstone, W. E., & Marti, U. (2010). Combining airborne and satellite gravimetry with topographic information for regional geoid determination. *Journal of Geophysical Research: Solid Earth*, 115(B10). <https://doi.org/10.1029/2010JB007519>

Hirt, C., Yang, M., Kuhn, M., Bucha, B., Kurzmann, A., & Pail, R. (2019). SRTM2gravity: An ultrahigh resolution global model of gravimetric terrain corrections. *Geophysical Research Letters*, 46(20). <https://doi.org/10.1029/2019GL082521>

Hofmann-Wellenhof, B., & Moritz, H. (2006). *Physical geodesy* (2nd ed.). SpringerWienNewYork. <https://doi.org/10.1007/978-3-211-33545-1>

Hwang, C., Hsiao, Y.-S., & Shih, H.-C. (2003). Orthometric corrections from levelling, gravity, density and elevation data: A case study in Taiwan. *Journal of Geodesy*, 77(5–6), 279–291. <https://doi.org/10.1007/s00190-003-0325-6>

Ince, E. S., Barthelmes, F., Reißland, S., Elger, K., Förste, C., Flechtner, F., & Schuh, H. (2019). ICGEM – 15 years of successful collection and distribution of global gravitational models, associated services, and future plans. *Earth System Science Data*, 11(2), 647–674. <https://doi.org/10.5194/essd-11-647-2019>

Jekeli, C., & Serpas, J. G. (2003). Review and numerical assessment of the direct topographical reduction in geoid determination. *Journal of Geodesy*, 77(4–5), 226–239. <https://doi.org/10.1007/s00190-003-0320-7>

Jiang, X., & Wang, Y. (2020). Improving regional geoid models using airborne gravity and terrestrial data in mountainous areas. *Journal of Geodesy*, 94(7), 1–14. <https://doi.org/10.1007/s00190-020-01367-0>

Kiamehr, R., & Sjöberg, L. E. (2005). Effect of the SRTM global DEM on the determination of a high-resolution geoid model: A case study in Iran. *Journal of Geodesy*, 79(9), 540–551. <https://doi.org/10.1007/s00190-005-0006-8>

Li, X., Huang, J., Klees, R., Forsberg, R., Willberg, M., Slobbe, C., Hwang, C., & Pail, R. (2022). Characterization and stabilization of the downward continuation problem for airborne gravity data. *Journal of Geodetic Science*, 12(1), 11–33. <https://doi.org/10.1515/jogs-2021-0001>

Li, X., Wang, Y., & Kearsley, A. (2018). Geoid computation using airborne gravity data in rugged terrain. *Survey Review*, 50(359), 157–164. <https://doi.org/10.1080/00396265.2016.1266987>

Li, X., & Huang, J. (2019). Downward continuation methods of airborne gravity data and their impacts on local geoid modeling. *Geophysical Research Abstracts*, 21, EGU2019-10766.

Lin, M., Guo, J., Liu, X., Chang, L., Chang, X., & Liu, X. (2025). Refining regional gravity anomalies and vertical deflections of high-degree Earth gravity model from residual terrains based on the spatial domain method. *Earth, Planets and Space*, 77, 37. <https://doi.org/10.1186/s40623-025-02168-y>

Liu, Y., Fan, Y., Zhu, Z., Liu, C., & Feng, G. (2023). Regional gravity field modeling using band-limited spherical radial basis functions: A case study in Colorado. *Remote Sensing*, 15(18), 4515. <https://doi.org/10.3390/rs15184515>

Marti, U. (2004). The use of the remove-compute-restore technique in gravity field modeling. In *Gravity, Geoid and Space Missions* (pp. 155–160). Springer. https://doi.org/10.1007/978-3-662-10367-6_27

Martinec, Z., & Vaníček, P. (1994). The indirect effect of topography in the Stokes–Helmert technique for a spherical approximation of the geoid. *Manuscripta Geodaetica*, 19(2), 213–219. <https://doi.org/10.1007/BF01954887>

National Centers for Environmental Information. (n.d.). *Land and Marine Gravity Data – Dictionary of Terms*. National Oceanic and Atmospheric Administration. https://www.ncei.noaa.gov/sites/g/files/anmtlf171/files/202505/Land_and_Marine_Gravity_Data_Dictionary.pdf

National Geodetic Survey. (2017). *GGSV17: Geoid Slope Validation Survey 2017*. National Geodetic Survey, NOAA. <https://www.ngs.noaa.gov/GEOID/GSVS17/>

National Geodetic Survey. (2019). *GRAV-D: Gravity for the Redefinition of the American Vertical Datum*. NOAA. <https://www.ngs.noaa.gov/GRAV-D/>

NOAA, NASA, & USAF. (1976). *U.S. Standard Atmosphere, 1976*. U.S. Government Printing Office.

Pavlis, N. K., Holmes, S. A., Kenyon, S. C., & Factor, J. K. (2012). The development and evaluation of the Earth Gravitational Model 2008 (EGM2008). *Journal of Geophysical Research: Solid Earth*, 117(B4). <https://doi.org/10.1029/2011JB008916>

Reguzzoni, M., Sampietro, D., & Albertella, A. (2021). From ellipsoidal to orthometric heights: How accurate can we get with geoid models? *Geophysical Journal International*, 224(1), 169–174. <https://doi.org/10.1093/gji/ggaa457>

Saleh, J., & Smith, R. (2005). A comparison of geoid models for the United States: The effect of airborne gravity data. *Geophysical Research Letters*, 32(10). <https://doi.org/10.1029/2005GL022909>

Sant'Anna, S. A., Haag, M., & Heck, B. (2015). Evaluation of Remove–Compute–Restore techniques for geoid modeling in mountainous areas. *Journal of Geodetic Science*, 5(1), 33–41. <https://doi.org/10.1515/jogs-2015-0003>

Schwarz, K. P., Sideris, M. G., & Forsberg, R. (1990). The use of FFT techniques in physical geodesy. *Geophysical Journal International*, 100(3), 485–514. <https://doi.org/10.1111/j.1365-246X.1990.tb00701.x>

Sideris, M. G. (1987). On the application of spectral techniques to the gravimetric problem. In *Proceedings of the XIX IUGG General Assembly* (Vol. II, pp. 428–442). Vancouver, B.C., August 10–22.

Sideris, M. G. (1993). Gravity field convolutions without windowing and edge effects. *Bulletin Géodésique*, 67(2), 107–118. <https://doi.org/10.1007/BF01371374>

Sideris, M. G., & Forsberg, R. (2012). Evaluation of terrain corrections through FFT and classical integration in two selected areas of the Andes and their impact on geoidal heights. *Bol. Ciênc. Geod.*, 19(3), 407–419. <https://doi.org/10.1590/S1982-21702013000300004>

Sinnott, R. W. (1984). Virtues of the Haversine. *Sky and Telescope*, 68(2), 159.

Sjöberg, L. E. (1999). On the indirect effect in the Stokes–Helmert method of geoid determination. *Journal of Geodesy*, 73(2), 87–93.
<https://doi.org/10.1007/s001900050222>

Sjöberg, L. E. (2015). Rigorous geoid-from-quasigeoid correction using gravity disturbances. *Journal of Geodetic Science*, 5(2), 115–118. <https://doi.org/10.5194/jgs-5-115-2015>

Sjöberg, L. E. (2018). Topographic effects in geoid determinations. *Geosciences*, 8(4), 143. <https://doi.org/10.3390/geosciences8040143>

Sjöberg, L. E., & Bagherbandi, M. (2017). *Gravity inversion and integration: Theory and applications in geodesy and geophysics*. Springer International Publishing.
<https://doi.org/10.1007/978-3-319-50298-4>

Smith, D. A., & Milbert, D. G. (1998). Evaluation of the EGM96 gravity model over the United States. *Physics and Chemistry of the Earth*, 23(9–10), 865–870.
[https://doi.org/10.1016/S0079-1946\(98\)00109-5](https://doi.org/10.1016/S0079-1946(98)00109-5)

Smith, D. A., Li, X., & Holmes, S. A. (2013). A new high-resolution regional geoid model for the United States: USGG2012. *Journal of Geodesy*, 87(8), 747–764.
<https://doi.org/10.1007/s00190-013-0646-x>

Strang, G. L., & van Hees, G. S. (1990). Stokes formula using Fast Fourier techniques. *Manuscripta Geodaetica*, 15(4), 235–239. <https://doi.org/10.1007/BF03655408>

Tziavos, I. N. (1993). *Numerical considerations of FFT methods in gravity field modelling* (Wissenschaftliche Arbeiten der Fachrichtung Vermessungswesen der Universität Hannover, Nr. 188). Universität Hannover.

Varga, M., Pitoňák, M., Novák, P., & Bašić, T. (2021). Contribution of GRAV-D airborne gravity to improvement of regional gravimetric geoid modeling in Colorado, USA. *Journal of Geodesy*, 95, 53. <https://doi.org/10.1007/s00190-021-01494-9>

Varga, M., Szucs, E., & Toth, G. (2021). Regional geoid determination with combined terrestrial and airborne gravity data. *Geosciences*, 11(3), 73.
<https://doi.org/10.3390/geosciences11030073>

Wang, Y. M., & Rapp, R. H. (1990). Computation of the terrain correction for gravity anomalies using density anomalies (Report No. 483). Department of Geodetic Science and Surveying, Ohio State University.

Wang, Y. M., Sánchez, L., Ågren, J., Huang, J., Forsberg, R., Abd Elmotaal, H. A., Ahlgren, K., Barzaghi, R., Bašić, T., Carrion, D., et al. (2021). Colorado geoid computation experiment: Overview and summary. *Journal of Geodesy*, 95(12), 127. <https://doi.org/10.1007/s00190-021-01567-9>

Willberg, M., Ahlgren, K., Zingerle, P., & Pail, R. (2021). Improvement of the GRAV-D Processing (NOS NGS Technical Report No. 75). NOAA National Geodetic Survey.

Yildiz, H., Forsberg, R., Ågren, J., Tscherning, C. C., & Sjöberg, L. E. (2012). Comparison of remove–compute–restore and least squares modification of Stokes' formula techniques to quasi-geoid determination over the Auvergne test area. *Journal of Geodetic Science*, 2(1), 53–64. <https://doi.org/10.2478/v10156-011-0024-9>

Zhang, Y., & Wong, K. W. (2015). BTTB-based numerical schemes for three-dimensional gravity field inversion. *Geophysical Journal International*, 202(2), 1091–1107. <https://doi.org/10.1093/gji/ggv220>